SCUOLA DI DOTTORATO
UNIVERSITÀ DEGLI STUDI DI MILANO-BICOCCA

Dipartimento di / Department of

Physics “Giuseppe Occhialini

Dottorato di Ricerca in / PhD program Physics Ciclo / Cycle XXXV

Curriculum in Subnuclear Physics

Measurement of charm mixing and CP violation parameter y_{CP} with $D^0 \to K_S^0 K^+ K^-$ decays at the LHCb detector

Cognome / Surname: Shields Nome / Name: Edward

Matricola / Registration number: 854372

Tutore / Tutor: Prof. Marta Calvi

Supervisor: Prof. Maurizio Martinelli

Coordinatore / Coordinator: Prof. Stefano Ragazzi

ANNO ACCADEMICO / ACADEMIC YEAR 2021/2022

Abstract

This thesis presents a measurement of the mixing and CP violation parameter y_{CP} using a sample of D^0 mesons decaying to the final state $D^0 \to K^0_S K^+ K^-$. The measurement is performed with a sample of D^0 mesons originating both from the primary vertex and from the secondary decays of B mesons collected in the Run II (2015-2018) of the LHC by the LHCb experiment at CERN, using proton-proton collisions, with a center-of-mass energy of 13 TeV and an integrated luminosity of 5.7 fb^{-1}.

The measurement of y_{CP} is performed using a novel technique for hadron colliders that involves measuring the difference in the number of candidates produced in different regions of the three body decay phase-space. We study the ratio of the number of candidates produced on the $D^0 \to K^0_S\phi(1020)$ resonance (ON-resonance) to number of candidates produced off this resonance (OFF-resonance), and extract y_{CP} through a fit to the decay time distribution of this ratio,

$$\frac{dN_{\mathrm{ON}}}{dN_{\mathrm{OFF}}} = 1 - 2\left(f_{\mathrm{ON}} - f_{\mathrm{OFF}}\right)\frac{t}{\tau_{D^0}} y_{CP}.$$

At the time of submitting the thesis, the measurement of the value of y_{CP} is still blinded as per LHCb procedure and to avoid any biases while the analysis is finalised. A preliminary estimation of the statistical and systematic uncertainties is calculated and we measure,

$$y_{CP} = (X.XX \pm 0.099\,(\mathrm{stat}) \pm 0.083\,(\mathrm{syst}))\,\%.$$

Sommario

L'argomento principale di questa tesi è la misura del parametro di mixing e violazione di *CP* y_{CP} nei decadimenti dei mesoni con Charm. Per effettuare questa misura si è studiato un campione di decadimenti $D^0 \to K^0_S K^+ K^-$ raccolto a LHC durante il RunII (2015-2018) dall'esperimento LHCb, corrispondente ad una energia nel centro di massa di 13 TeV e ad una luminosità integrata di $5.7\,\mathrm{fb}^{-1}$. I decadimenti del D^0 sono ricostruiti sia se prodotti nel punto di collisione dei due protoni che se originati da decadimenti di adroni con Beauty.

La misura di y_{CP} è ottenuta utilizzando una tecnica nuova per i collisori adronici misurando il rapporto tra il numero di candidati ricostruiti in regioni distinte dello spazio delle fasi del decadimento a tre corpi. Le regioni prese in considerazione sono quella dominata dal decadimento $D^0 \to K^0_S \phi(1020)$ (ON) e quelle intorno a questa risonanza (OFF). La distribuzione del rapporto tra il numero di eventi nelle due regioni permette di misurare y_{CP}:

$$\frac{dN_{\mathrm{ON}}}{dN_{\mathrm{OFF}}} = 1 - 2\,(f_{\mathrm{ON}} - f_{\mathrm{OFF}})\,\frac{t}{\tau_{D^0}} y_{CP}.$$

Al momento di sottomettere questa tesi il valore y_{CP} è ancora nascosto al fine di permettere una revisione imparziale da parte della collaborazione LHCb. Viene perciò riportata una stima preliminare delle incertezze statistiche e sistematiche di questa misura:

$$y_{CP} = (X.XX \pm 0.099\,(\mathrm{stat}) \pm 0.083\,(\mathrm{syst}))\,\%.$$

Acknowledgements

The thesis presented here would not have been possible without the help and support of a large number of people. First and foremost, to Prof. Maurizio Martinelli, my PhD supervisor, he has taught me so much about charm physics and high energy physics more broadly. He had unending patience with me and I was particularly appreciative of his constant encouragement for me to learn and try new things, it made the entire PhD experience an incredibly enjoyable one. I cannot describe it any other way than an absolute pleasure to work with Maurizio.

I must also thank Prof. Marta Calvi for her support and guidance throughout my PhD. It was an honour to be a part of the Bicocca LHCb group for three years.

To all my colleagues and friends who at one point or another have worked in the Bicocca office. In particular to: Simone Meloni, Simone Capelli, Davide Fazzini, and Julian Garcias, it was a pleasure to work with you all.

I was fortunate enough to have a fantastic group of friends both here in Milan and back in England who have been incredibly supportive and tolerant throughout my PhD

All of my ‘seconda famiglia’ in Milan: Chiara, Luigi, Andrea, Gemma, Alba, Sylvi, Ljuba, and Giorgio, have been so welcoming and kind to me. They welcomed me with open arms into their family and I will be forever grateful for that.

To Elizabeth, of whom I could not have asked for more and will be forever grateful. A constant source of love, support, and encouragment, who helped me through every moment.

Finally I am under no doubt that I was only able to get to this position due to the incredible love and support of my wonderful family. Daniel, Rachel, and Marta have been so supportive and encouraging throughout my PhD, and I am very proud of them. To my mum and dad who not only inspired me but gave me the confidence to set out on this incredible journey, thank you.

Milano, 27th January 2023 E.B.B.S.

Contents

Part I

Introduction

For thousands of years humankind has thought about what constitutes the fundamental matter that makes up our universe. Over two thousand years ago, the Greek philosopher Democritus proposed the theory that everything is composed of '*atoms*', which are physically, but not geometrically, indivisible; that between atoms, there lies empty space; that atoms are indestructible, and have always been and always will be in motion; that there is an infinite number of atoms and of kinds of atoms, which differ in shape and size [1]. Over time the theory of the fundamental matter has evolved, from Newton, who introduced the idea of infinitely hard smooth balls as the constituents of matter, and gravity as the first force that acts between them [2]. Chemists then discovered the atoms of a large number of elements, which were found to be divisible, consisting of a nucleus surrounded by an electron cloud, and then this nucleus was found to be made of protons and neutrons. This was the picture of the atom and fundamental matter that was prevalent until around 1930

Further discoveries in the 20th century led to a far richer understanding of the sub-atomic world. The '*particle zoo*' with lots of newly discovered mesons, pions and 'strange' particles was leading to confusion. New elementary particles such as quarks, leptons and gauge bosons were discovered and a more complete picture evolved. Today almost all of fundamental particle physics can be explained through the Standard Model, it is able to provide precise predictions about the existence of particles and their interactions. In the last few decades, the discovery of the top quark [3, 4] and the tau neutrino [5] gave further validation of the theory. Then in 2012 the last missing piece of the Standard Model, the Higgs Boson, was discovered by the ATLAS and CMS collaborations at CERN [6, 7].

Despite the remarkable success of the Standard Model in its predictions, it cannot be the final theory for our understanding of fundamental matter in the universe. There are too many arbitrary parameters (e.g. masses of particles, values of couplings) which have to be determined experimentally; an underlying theory based on first principles is still missing. There are further problems posed by mainly astrophysical data that also cannot be explained by the Standard Model: it does not fully explain the baryon asymmetry [8–10]; there is no inclusion of gravity and general relativity in the theory; the theory contains no viable dark matter or dark energy candidates; and it cannot account for neutrino oscillations [11, 12] or their non-zero masses [13].

To date all attempts to find experimental deviations from the Standard Model of particle-level observables have failed. The are two main approaches to searches for New Physics, that is physics beyond the Standard Model: *direct* searches and *indirect* searches. Direct searches look directly for new on-mass shell particles or interactions predicted by a theoretical model, an example of this include searches for SUSY particles. The other approach, which is the approach taken in this thesis, is to test the Standard Model to ever increasing levels of precision. If there is found to be a statistically significant deviation between an experimental observation and its theoretical prediction, then this would be a strong indication that there is New Physics and would perhaps provide a hint as to where to look for this. In this thesis we are focussing on the latter approach, indirect searches for New Physics, in particular in the area of *flavour* physics.

Flavour physics is the study of particles and their interactions between other particles of different flavours. The Standard Model gives six flavour of leptons and six flavour of quarks, and the interactions between them is predicted by the Standard Model. By studying these interactions we can perform indirect searches for New Physics. Two particular phenomena are interesting in flavour physics, neutral meson mixing and *CP* violation.

Neutral meson mixing is the phenomenon in which a particle can oscillate back and forth with its antiparticle counterpart. The property was predicted, initially for neutral kaons (K^0), by Murray Gell-Mann and Abraham Pais in 1955 [14] and was necessary to explain the regeneration patterns of the K^0 meson in 1960 [15]. Neutral meson mixing has subsequently been observed in the neutral beauty meson (B^0) system by the ARGUS collaboration in 1987 [16]; in the neutral strange-beauty meason (B_s^0) system by the CDF collaboration in 2006 [17]; and in the neutral charm meson (D^0) system initially by the BaBar and Belle collaborations in 2007 [18, 19], then in a single experiment by the LHCb collaboration in 2012 [20]. The study of mixing between D^0 and $\overline{D}^0$ is extremely challenging due to the oscillation rate being highly suppressed relative to the mixing rates of the kaon or beauty systems.

The second phenomenon of interest is *CP* violation, which can be seen in differences between the behaviour of matter and antimatter. A surprising absence in our universe is that of 'primordial' antimatter from the Big Bang. In the early stages of the expanding universe, a hot (10^{32}K) and dense plasma of quarks, antiquarks, leptons, antileptons, and photons existed in equilibrium. As the universe cooled down, all the matter and antimatter could combine and annihilate into photons. If all interactions were symmetric between matter and antimatter and baryon and lepton numbers are conserved, all the particles would eventually convert to photons and the expansion of the Universe would shift the wavelength of these photons to the far infrared region [21]. This cosmic background radiation was observed by Penzias and Wilson in 1965 [22] and its wavelength distribution corresponds exactly to the expected Planck black-body radiation temperature. However there is also a small amount of baryonic matter left over, and this phenomenon can only be explained if the three conditions of Sakharov are fulfilled [23]: there must be an interaction violating *CP* invariance, where C is the particle-antiparticle transformation and P the space inversion operator; there must be an interaction violating the conservation of baryon number; and there must be phases of the expansion without thermodynamic equilibrium.

The first condition was shown to be fulfilled by the discovery of *CP* violation in decays of neutral K mesons by James Cronin and Val Fitch in 1964 [24]. Later it was observed in the B sector by the BaBar and Belle collaborations in 2001 [25, 26] and in the D sector by the LHCb collaboration in 2019 [27].

CP violation occurs in the Standard Model in the quark sector due to the presence of a single complex phase in the Cabibbo- Kobayashi-Maskawa (CKM) matrix [28]. Aditional sources of *CP* violation arise in BSM theories. The phase was originally introduced when only three of the six quarks were known and was a consequence of the extension to the GIM mechanism [29] required to account for *CP* violation. The CKM mechanism successfully predicted the existence of the heaviest two quarks, the beauty and top quarks, which were discovered at Fermilab in 1977 [30] and 1995 [3, 4] respectively. All measurements of *CP* violation so far have been consistent with the Standard Model predictions. However our current understanding of *CP* violation is not sufficient to explain the baryon asymmetry in the universe and thus New Physics beyond the Standard Model is still needed to explain this asymmetry.

In this thesis a measurement of the mixing and *CP* violation parameter y_{CP} is presented by studying $D^0 \to K^0_S K^+ K^-$ decays at the LHCb experiment. The parameter y_{CP} is measured using a novel technique first developed by the BaBar collaboration [31, 32]. By studying different regions of the three body decay phase-space, we can avoid flavour tagging the D^0 sample and extract y_{CP} by directly measuring the ratio of events produced in different regions of phase-space. The analysis presented makes use of proton-proton (pp) collision data collected by the LHCb experiment during the Run II (2016-2018) data taking period of the LHC at a centre-of-mass energy of 13 TeV. The data sample corresponds to an integrated luminosity of 5.7 fb^{-1}. The parameter y_{CP} is measured using D^0 decays to the $K^0_S K^+ K^-$ final state.

The thesis has the following structure: Part I gives an introduction to the physics relevant to the thesis. Chapter 1 offers a description of the Standard Model and of flavour physics, while in Chapter 2 the LHCb detector is described. Part II describes the analysis performed to measure y_{CP}, with Chapter 3 describing the formalism of the technique, Chapter 4 gives details about the data used and how it was selected, Chapter 5 shows how the measurement was performed, and Chapter 6 outlines how the systematic uncertainties were treated and estimated.

1 Theory and Motivations

1.1 The Standard Model

The *Standard Model* (SM) of particle physics is a quantum field theory that describes three of the four fundamental forces of nature:

- The *electromagnetic force* is responsible for interactions between electrically charged particles.
- The *strong force* is responsible for the interaction of quarks inside the nuclei of atoms.
- The *weak force* facilitates the radioactive decays of atoms.

The fourth force, the *gravitational force*, is not described by the SM.

The SM gives rise to a rich set of interactions between particles, where these interactions are governed by a local relativistic quantum field theory. To each fundamental, or point-like particle, is associated a field with appropriate transformation properties under the *Poincare group* (the relativistic space-time coordinate transformations). The description of all the particle interactions is based on a common principle of *gauge invariance*. A gauge symmetry is invariant under transformations that rotate the basic internal degrees of freedom but with rotation angles that depend on the space-time point. Theories with gauge symmetry are completely determined by the given symmetry group and representations in the interacting fields. The whole set of electromagnetic, strong, and weak interactions is described by such a gauge theory, with twelve gauged non-commuting charges, referred to as the Standard Model.

However, only a subgroup of the SM symmetry is directly reflected in the spectrum of physical states. A part of the electroweak symmetry is hidden by the Higgs mechanism for the spontaneous symmetry breaking of a gauge symmetry [21].

The SM is a non-abelian, local gauge invariant theory, under the symmetry group [33],

$$G_{\mathrm{SM}} = SU(3)_C \otimes SU(2)_L \otimes U(1)_Y \,. \tag{1.1}$$

- $SU(3)_C$ is the *colour group* of the theory of strong interactions [34–38].

- The $SU(2)_L \otimes U(1)_Y$ group describes the electroweak interactions [39–41].

The SM symmetry group, shown in Equation (1.1), has $8 + 3 + 1 = 12$ generators. In a gauge theory, to every generator, T, is associated a vector boson (or gauge boson) with the same quantum numbers as T. If the gauge symmetry is unbroken, then this boson is of vanishing mass. These vector (i.e of spin 1) bosons act as mediators of the corresponding interaction. The $SU(3)$ group has 8 massless gluons associated to the color generators, while the $SU(2) \otimes U(1)$ group has 4 gauge bosons: W^+, W^-, Z, and γ. Of these only the photon, γ, is massless because the symmetry induced by the other three generators is spontaneously broken. The masses of the W^+, W^-, and Z are fairly large on the scale of elementary particles: $m_W \sim 80.4\,\text{GeV}$ [1], $m_Z \sim 91.2\,\text{GeV}$ [42].

In the electroweak theory, the breaking of the symmetry is spontaneous. In this mechanism the charges and currents are dictated by the symmetry of the group, but the fundamental state of minimum energy, the vacuum, is not unique. There is a continuum of degenerate vacuum states that respects the symmetry of the group, meaning the whole vacuum orbit can be spanned by applying the symmetry transformations. A simpler example of the potential of a $U(1)$ symmetry group with potential, $V(\phi^\star\phi) = \mu^2(\phi^\star\phi) + \lambda(\phi^\star\phi)^2$ is shown in Fig. 1.1.

The symmetry breaking is due to the system, which has infinite volume and infinite degrees of freedom, being found in one particular vacuum state. This choice of state is made in the beginning instants of the universe, and violates the symmetry in the spectrum of states. In the SM, this spontaneous symmetry breaking is realized by the Higgs mechanism [44–48][2]: There is a scalar (spin 0) boson with a potential that produces an orbit of degenerate vacuum states.

The SM can be formulated in terms of its Lagrangian, which when written in the compact representation [49], is written as

[1] Here and generally elsewhere in this thesis (unless when it is clearly not the case), we use natural units by taking $c = h = 1$

[2] Although the mechanism and boson have become known by the name Higgs, the mechanism was discovered independently by a number of physicists all within a short space of time. However Peter Higgs was the only one to explicitly state that the Higgs mechanism necessitated the existence of a massive scalar boson, hence the mechanism and boson were subsequently named after him. The other physicist who wrote papers at the same time on the topic are: Englart, Brout, Guralnik, Hagen and Kibble.

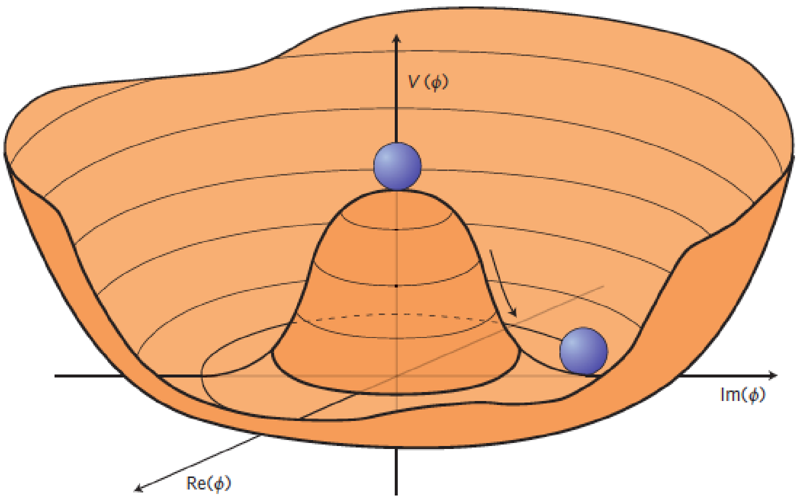

Figure 1.1: *An illustration of the Higgs potential in the case that $\mu^2 < 0$, in which case the minimum is at $|\phi|^2 = -\mu^2/(2\lambda)$. Choosing any of the points at the bottom of the potential breaks spontaneously the rotational $U(1)$ symmetry [43].*

$$
\begin{aligned}
\mathcal{L}_{\mathrm{SM}} = & -\frac{1}{4}F_{\mu\nu}F^{\mu\nu} \\
& + i\bar{\psi}\not{D}\psi + h.c. \\
& + \bar{\psi}_i y_{ij}\psi_j\phi + h.c. \\
& + |D_\mu\phi|^2 - V(\phi).
\end{aligned}
\tag{1.2}
$$

The fundamental particles of the SM can be split into two categories, gauge bosons and *fermions*. The gauge bosons, as described above are the mediators of their respective theories, and obey Bose-Einstein statistics. Fermions are spin-$\frac{1}{2}$, and each fermion has an anti-particle with the same mass but opposite charge. Fermions are separated into three generations, whose main difference is the mass. Further, fermions can be split into two types: leptons and quarks.

Leptons are split into two groups: charged leptons and neutrinos. The charged leptons have a charge of -1 and the three generations are the *electron*, *muon*, and *tau lepton*. Each charged lepton has a corresponding neutral neutrino. The SM predicts the neutrinos to be massless; however, recent observations of neutrino oscillations mean that at least two of the three generations must have a non-zero mass [13]. Leptons are not sensitive to the strong force as they don't posses colour charge.

There are six types of quarks that are sensitive to all three forces of the SM. They each possess a *flavour*. There are three quarks that have a positive, $+\frac{2}{3}$ charge: *up*, *charm*, and *top*. Similarly there are three quarks with a negative

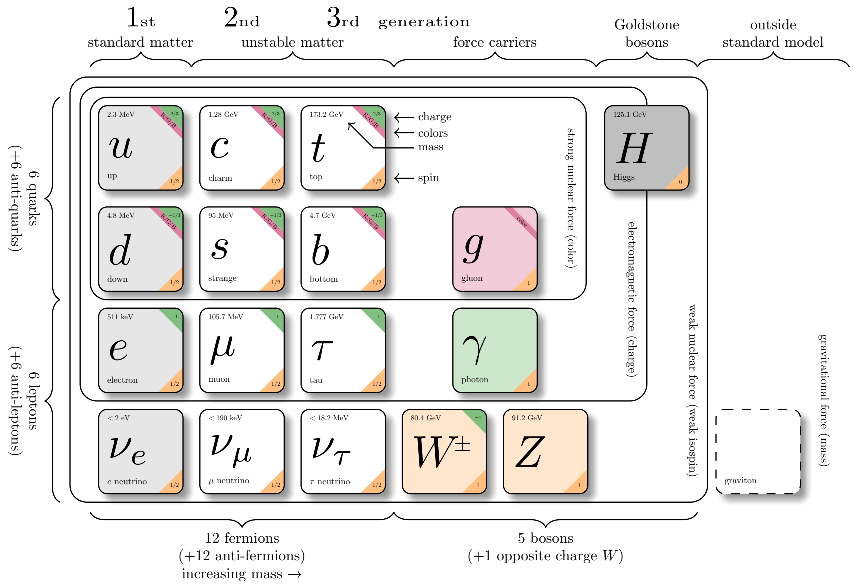

Figure 1.2: *Overview of the Standard Model and its fundamental particles [50].*

$-\frac{1}{3}$ charge: *down*, *strange*, and *beauty* (or *bottom*). All quarks have a color, red, green, or blue, that dictates how the gluons interact with them.

To summarize, also shown in Fig. 1.2:

<u>Gauge bosons</u>

- 8 massless gluons, g, the strong-force carriers that bind quarks together. Any hadron constructed from quarks must be color neutral.
- 3 massive weak bosons, W^+, W^-, and Z. They are the weak-force carriers and mediate flavour changing processes and particle decays.
- 1 massless photon, γ, the electromagnetic-force carrier.

<u>Fermions</u>

- 6 quarks and anti-quarks. They have a flavour, color charge, and interact with all the forces of the SM.
- 6 leptons and anti-leptons. Come in two types, charged leptons and neutrinos. They do no interact via the strong force.

1.2 Discrete symmetries

A discrete symmetry is a symmetry that describes non-continuous changes in a system. In the SM there are three discrete symmetries, meaning there are three non-continuous transformations that can be applied to the theory:

- The *charge-conjugation* transformation, C, transforms a particle into its anti-particle, and vice-versa.
- The *parity* transformation, P, inverts the spatial coordinates of a particle: $\mathbf{x} \to -\mathbf{x}$.
- The *time reversal* transformation, T, inverts the time coordinate: $t \to -t$.

The electromagnetic and strong forces conserve all three of these symmetries, and their combinations, so their interactions are unchanged after any of the symmetry transformations. The weak interaction, however, violates all three of these symmetries.

An interesting property of the weak theory is that it is a *chiral* theory. Chirality is a fundamental property of the particle which breaks left-right symmetry. For a massless particle it is identical to helicity which is a property that defines the direction of spin of a particle with respect to the direction of its momentum. For a massless left-handed particle, the direction of its spin is opposite to the direction of its momentum, while the opposite is true for right-handed particles, as shown in Fig. 1.3[3]. Robert Marshak, George Sudarshan, Richard Feynman and Murray Gell-Mann developed the **V-A** theory [51,52] in 1957, that states the weak interaction only acts on left-handed particles and right handed anti-particles. Thus it maximally violates P symmetry.

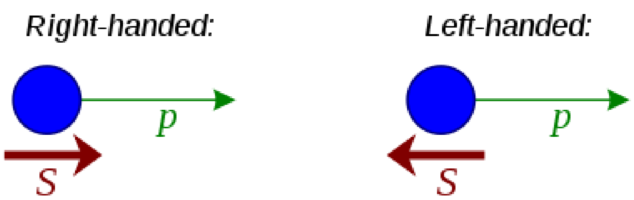

Figure 1.3: *Diagram of helicity of particles [53].*

The violation of P symmetry was discovered before the formulation of the electroweak theory. In 1956 theorists Chen-Ning Yang and Tsung-Dao Lee

[3] For massive particles, chirality is slightly more abstract. It is determined by whether the particle transforms in a right- or left-handed representation of the Poincaré group. It is possible to boost to a reference frame to reverse the direction of momentum and thus switch the helicity of the particle.

questioned why the τ^+ and θ^{+4} particles had identical properties but decayed weakly to two different final states with opposite parities. They proposed that parity conservation had never been tested experimentally in weak decays, and suggested an experiment to test the idea [54]. Chinese physicist Wu Chien-Shiung later tested the theory through an analysis of the *beta* decay of Cobalt-60. She found that the weak interaction violates parity symmetry as some processes did not occur with the same probability as they did for their mirror images [55].

In 1964, two American physicists, James Cronin and Val Fitch, studied the decay of neutral kaons and found that the combination of C and P symmetry, CP symmetry, was not conserved. This gave rise to the study of CP violation which has been discovered in the B meson system by the BaBar and Belle collaborations [25, 26], and recently in the D^0 meson by the LHCb collaboration [56].

CP violation has been suggested as a explanation for the observed asymmetry between matter and antimatter. In 1967, Andrei Sakharov set out three conditions that need to be fulfilled to explain the remaining baryonic matter we observe in our universe after the big bang [57]:

- There must be an interaction violating CP invariance.
- There must be an interaction violating the conservation of baryon number.
- There must be phases of the expansion without thermodynamic equilibrium.

However it has since been established that the amount of CP violation predicted by the SM is insufficient to explain the matter antimatter asymmetry observed in the universe [58]. Thus new physics beyond the SM is needed and expected, in order to explain the matter-antimatter asymmetry phenomenon.

1.3 Quark flavour changing transitions

As was mentioned in Section 1.1, there are six types of quarks each with a distinct flavour. In the weak interaction a quark can change its flavour through the exchange of a $W^\pm$ boson. This results in a flavour change from an up-type quark to a down-type quark. In 1963, only three of the six quarks had been observed, Italian physicist Nicola Cabibbo proposed a cabibbo angle θ_c

[4] Now known to be the same particle, K^+, and the τ here is not the same as the *tau* lepton described before.

to describe how the flavour of quarks can change in the weak interaction [59],

$$d' = d\cos\theta_c + s\sin\theta_c. \tag{1.3}$$

It can be seen that d' is the superposition of the down, d, and strange, s, quarks. Cabibbo then introduced the Cabibbo matrix, V_c to describe the weak transitions of the first two generations of quarks,

$$\begin{bmatrix} d' \\ s' \end{bmatrix} = V_c \begin{bmatrix} d \\ s \end{bmatrix} = \begin{bmatrix} \cos\theta_c & \sin\theta_c \\ -\sin\theta_c & \cos\theta_c \end{bmatrix} \begin{bmatrix} d \\ s \end{bmatrix}. \tag{1.4}$$

The quark transitions described by the matrix V_c progress via the exchange of a $W^{\pm}$ boson. In this process the $W^{\pm}$ boson mediates transitions from up to down type quarks (and vice-versa), and due to the maxing between the generations transitions are possible not only within a single generation, but also between generations. The relative amplitudes of these transitions are given by the relevent matrix element of the Cabibbo matrix.

In the late sixties came more measurements relating to strangeness changing neutral current processes such as $K^0_{\mathrm{L}} \to \mu^+\mu^-$ decays and $K^0 - \overline{K}^0$ mixing, which revealed discrepancies of several orders between experimental values and theoretical predictions of the current models. Experiments showed strong suppression of these processes with respect to existing theoretical predictions. The solution to this came from Sheldon Glashow, John Iliopoulos, and Luciano Maiani, who in 1970 introduced an additional quark, the *charm* quark, to describe the new amplitudes needed to explain experimental measurements. This came to be known as the GIM mechanism [29]. Its application to $K^0 - \overline{K}^0$ mixing is shown in Fig. 1.4. It can be shown that in the case of $m_u = m_c$, amplitudes for the $d \to s$ transition would perfectly cancel out [60]. This model thus suggests why the processes are found to be suppressed in experimental data. The GIM mechanism predicted the mass of the charm quark to be much heavier than the rest of the quarks discovered at the time ($m_c \simeq 1.5\,\mathrm{GeV}$), in order to account for the level of neutral current suppression observed.

The predictions of the GIM mechanism were successfully confirmed in 1974 with the discovery of the J/ψ meson (a $c\bar{c}$ pair) at the Brookhaven National Laboratory (BNL) and the Stanford Linear Accelerator Center (SLAC) [61,62].

Despite the success of the GIM mechanism in explaining $K^0_{\mathrm{L}} \to \mu^+\mu^-$ decays and $K^0 - \overline{K}^0$ mixing, it was unable to account for *CP* violation. In 1973, Japanese physicists, Makoto Kobayashi and Toshihide Maskawa, noticed that *CP* violation could not be explained mathematically by only the first two generations of quarks. They then introduced two additional quarks, the b and t [5], in a third generation, to build a 3×3 unitary matrix, V_{CKM} [28],

[5]Subsequently discovered by the E288 experiment at Fermilab in 1977 [30] and by the CDF and D0 collaborations in 1995 [3,4] respectively.

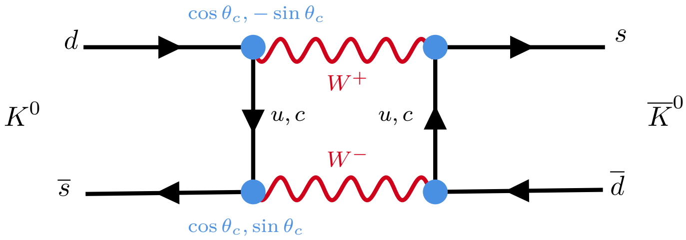

Figure 1.4: *Feynman diagram of $K^0 - \overline{K}^0$ mixing. In the case of $m_u = m_c$ the magnitude of the $d \to s$ amplitude would perfectly cancel out, $\cos\theta_c \sin\theta_c + (-\sin\theta_c)\cos\theta_c = 0$.*

$$\begin{bmatrix} d' \\ s' \\ b' \end{bmatrix} = V_{\text{CKM}} \begin{bmatrix} d \\ s \\ b \end{bmatrix} = \begin{bmatrix} V_{ud} & V_{us} & V_{ub} \\ V_{cd} & V_{cs} & V_{cb} \\ V_{td} & V_{ts} & V_{tb} \end{bmatrix} \begin{bmatrix} d \\ s \\ b \end{bmatrix}. \tag{1.5}$$

A $N \times N$ complex matrix, such as V_{CKM}, has $2N^2$ degrees of freedom. However since the matrix is unitary [6], the number of degrees of freedom is reduced to N^2. $2N - 1$ of the degrees of freedom have no physicality. Thus the number of parameters independent of the chosen set of phases is $N^2 - (2N-1) = (N-1)^2$. Of these, $\frac{1}{2}N(N-1)$ are the quark mixing angles, and the remaining $\frac{1}{2}(N-1)(N-2)$ are the *CP*-violating complex phases.

For the CKM matrix, V_{CKM}, which is a 3×3 unitary matrix, this leads to three mixing angles, θ_{12}, θ_{23}, and θ_{13}, and one complex phase, δ. This single complex phase is responsible for all of the *CP* violation in the Standard Model.

By writing $c_{ij} = \cos\theta_{ij}$ and $s_{ij} = \sin\theta_{ij}$, the CKM matrix can be written as,

$$V_{\text{CKM}} = \begin{bmatrix} c_{12}c_{13} & s_{12}c_{13} & s_{13}e^{i\delta} \\ -s_{12}c_{23} - c_{12}s_{23}s_{13}e^{i\delta} & c_{12}c_{23} - s_{12}s_{23}s_{13}e^{i\delta} & s_{23}c_{13} \\ s_{12}s_{23} - c_{12}c_{23}s_{13}e^{i\delta} & -c_{12}s_{23} - s_{12}c_{23}s_{13}e^{i\delta} & c_{23}c_{13} \end{bmatrix}. \tag{1.6}$$

This is referred to as the *standard* parametrization, however it is not very useful when trying to derive physical parameters that can be tested experimentally. In 1983, American physicist Lincoln Wolfenstein, introduced a new parametrization of the CKM matrix, which is more useful for experimental analysis, the *Wolfenstein* parametrization [63]. It is a precise approximation of the CKM matrix and highlights the hierarchy of the CKM elements. The Wolfenstein parametrization expresses the CKM matrix elements in terms of four parameters, λ, ρ, η, and A, which are related to the standard parametriz-

[6]A unitary matrix is a square matrix whose inverse is equal to its conjugate transpose, and thus satisfies $V^{-1} = V^{\dagger} \Leftrightarrow VV^{-1} = \mathbb{I}$

ation by,

$$
\begin{aligned}
\lambda &\equiv s_{12}, \\
A\lambda^2 &\equiv s_{23}, \\
A\lambda^3 \left(\rho - i\eta\right) &\equiv s_{13} e^{-i\delta}.
\end{aligned} \tag{1.7}
$$

With these four parameters, ρ, η, and A are of order unity and thus the CKM matrix can be expressed as a power series of $\lambda = \left|V_{us}\right|^2 \approx 0.23$, truncated at an order of $\mathcal{O}\left(\lambda^5\right)$,

$$
V_{\text{CKM}} = \begin{bmatrix} 1 - \frac{\lambda^2}{2} - \frac{\lambda^4}{8} & \lambda & A\lambda^3 \left(\rho - i\eta\right) \\ \lambda + \frac{\lambda^5}{2} A^2 \left(1 - 2\left(\rho + i\eta\right)\right) & 1 - \frac{\lambda^2}{2} - \frac{\lambda^4}{8}\left(1 + 4A^2\right) & A\lambda^2 \\ A\lambda^3 \left(1 - \left(\rho + i\eta\right)\right) + \frac{\lambda^5}{2} A \left(\rho + i\eta\right) & -A\lambda^2 + \frac{\lambda^4}{2} A \left(1 - 2\left(\rho + i\eta\right)\right) & 1 - \frac{\lambda^4}{2} A^2 \end{bmatrix}. \tag{1.8}
$$

From the order on λ for the CKM matrix elements it can be seen what transitions are suppressed and what are favoured. The most suppressed ones are the ones between the most separated generations of quarks such as $b \to u$ and $t \to d$ transitions.

From the unitarity of the CKM matrix, we can write,

$$
\begin{aligned}
&\sum_{k=u,c,t} V_{ki}^{\star} V_{kj} = \delta_{ij} \quad \text{with } i, j \in \{d, s, b\} \\
&\sum_{k=d,s,b} V_{ik}^{\star} V_{jk} = \delta_{ij} \quad \text{with } i, j \in \{u, c, t\}.
\end{aligned} \tag{1.9}
$$

Where δ_{ij} is the Kronecker delta. This leads to the following relations between the CKM matrix elements,

$$
V_{ud}^{\star} V_{ub} + V_{cd}^{\star} V_{cb} + V_{td}^{\star} V_{tb} = 0. \tag{1.10}
$$

The relation in Equation (1.10) can be visualised as a triangle in the complex plane, as shown in Fig. 1.5, and is referred to as the *unitary triangle*[7]. The unitary triangle is a useful tool for visualising the CKM matrix and the relations between the CKM matrix elements.

After rescaling for convenince, the vertices of the unitary triangle are $(0, 0)$, $(1, 0)$, and $(\overline{\rho}, \overline{\eta})$, where $\overline{\rho}$ and $\overline{\eta}$ follow,

$$
\overline{\rho} + i\overline{\eta} = -\frac{V_{ud} V_{ub}^{\star}}{V_{cd} V_{cb}^{\star}}. \tag{1.11}
$$

[7] There are six such triangles, one for each of the unitary relations with a zero on the right-hand-side. One of these triangles is especially interesting in the contect of flavour physics and *CP* violation which we refer to as the unitary traingle.

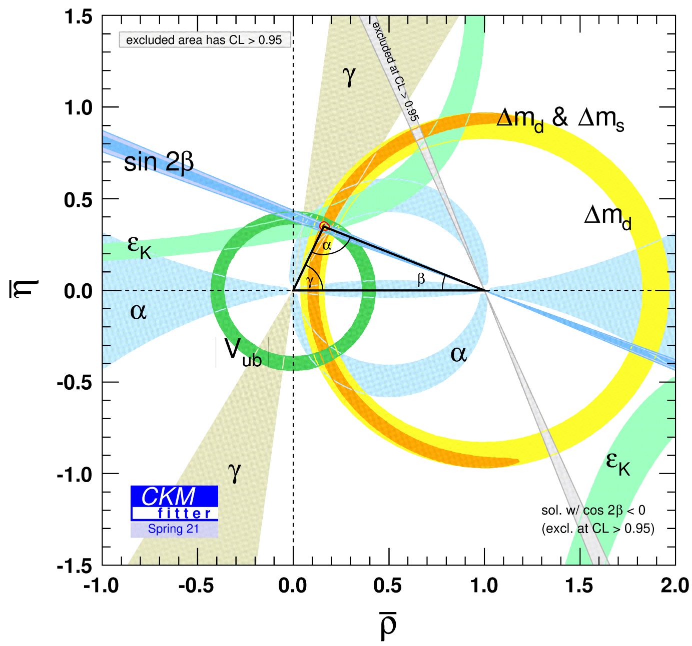

Figure 1.5: *The unitary triangle with constraints as of Summer 2021. The circles are experimental constraints on the lengths of the two non-fixed sides, while each angle is also constrained independently. Finally there s a band from the measurements of kaon CP violation, marked as ε_K. [64].*

The unitary triangle has angles α, β, and γ, which are defined as,

$$\begin{aligned} \alpha &= \arg\left(-\frac{V_{td}V_{tb}^{\star}}{V_{ud}V_{ub}^{\star}}\right), \\ \beta &= \arg\left(-\frac{V_{cd}V_{cb}^{\star}}{V_{td}V_{tb}^{\star}}\right), \\ \gamma &= \arg\left(-\frac{V_{ud}V_{ub}^{\star}}{V_{cd}V_{cb}^{\star}}\right). \end{aligned} \tag{1.12}$$

A key objective of the flavour physics community consists of constraining the unitary triangle by measuring the phases and various CKM matrix elements magnitudes, through the study of weak decays.

1.4 Neutral meson mixing

Neutral meson mixing refers to the quantum mechanical phenomenon in which neutral mesons can oscillate between particle and anti-particle states. This has been observed in K^0, B^0, B_s^0, and D^0 mesons, which are the only mesons which can exhibit mixing (the neutral mesons which can be distinguished from their antiparticles).

The propagation of a neutral meson and its anti-particle, N^0 and $\overline{N}^0$ respectively, is given by the Schrödinger equation [65],

$$i\frac{\partial}{\partial t}\begin{pmatrix}|N^0\rangle \\ |\overline{N}^0\rangle\end{pmatrix} = \mathscr{H}\begin{pmatrix}|N^0\rangle \\ |\overline{N}^0\rangle\end{pmatrix} \tag{1.13}$$

The mixing between the states causes the Hamiltonian to be non-diagonal. Thus, the flavour states are not eigenstates of the Hamiltonian, and as such do not have well defined masses or lifetimes. As with any quantum mechanical system, we can change to a different orthonormal, complete basis. In this bases we can write the quantum state of a neutral meson, $|\psi\rangle$, produced at $t = 0$, as the superposition of two *flavour eigenstates*, N^0 and $\overline{N}^0$,

$$|\psi\rangle = a(0)\,|N^0\rangle + b(0)\,|\overline{N}^0\rangle. \tag{1.14}$$

If we allow the state, $|\psi\rangle$ to evolve in time, it will evolve into a superposition of all its possible states including its final states, f_n,

$$|\psi(t)\rangle = a(t)\,|N^0(t)\rangle + b(t)\,|\overline{N}^0(t)\rangle + \sum_n c_n(t)\,|f_n\rangle. \tag{1.15}$$

Here only $a(t)$ and $b(t)$ are of interest to study neutral meson mixing. Now consider a window of time $[t, t + \Delta t]$, where t is orders of magnitude larger than the time scale considered when dealing with strong interaction processes. The time-dependent evolution of the system is then described by a 2×2 non hermitian effective Hamiltonian, $\mathscr{H}$, written explicitly as,

$$\mathscr{H} = \mathbf{M} - i\frac{\mathbf{\Gamma}}{2} = \begin{bmatrix} M_{11} - i\frac{\Gamma_{11}}{2} & M_{12} - i\frac{\Gamma_{12}}{2} \\ M_{21} - i\frac{\Gamma_{21}}{2} & M_{22} - i\frac{\Gamma_{22}}{2}\end{bmatrix}. \tag{1.16}$$

The Hamiltonian can be separated as a complex sum of two hermitian matrices, $\mathbf{M}$ and $\mathbf{\Gamma}$. Here $\mathbf{M}$ is the dispersive mixing amplitude. In the SM it is dominated by short distance contributions of off-shell, or virtual, intermediate states. Additional undiscovered particles beyond the SM can appear in the virtual loops and hence influence these short distance amplitudes. $\mathbf{\Gamma}$ is the absorptive mixing amplitude, due to long distance contributions of on-shell intermediate states, *i.e.* decays [66].

Calculating the eigenvectors of the Hamiltonian, $\mathscr{H}$, gives access to the eigenstates $|N_1\rangle$ and $|N_2\rangle$. These are also referred to as the *mass eigenstates*. From this we can now relate the mass eigenstates to the flavour eigenstates as,

$$\begin{bmatrix}|N_1\rangle \\ |N_2\rangle\end{bmatrix} = \mathbf{Q}\begin{bmatrix}|N^0\rangle \\ |\overline{N}^0\rangle\end{bmatrix} \quad \text{with } \mathbf{Q} = \begin{bmatrix}p & q \\ p & -q\end{bmatrix}. \tag{1.17}$$

Which gives,

$$|N_1\rangle = p|N^0\rangle + q|\overline{N}^0\rangle \tag{1.18}$$

$$|N_2\rangle = p|N^0\rangle - q|\overline{N}^0\rangle \tag{1.19}$$

where p and q are complex numbers that satisfy the relationships [67]

$$|p|^2 + |q|^2 = 1, \tag{1.20}$$

and

$$\left(\frac{p}{q}\right)^2 = \frac{M_{21} - \frac{i}{2}\Gamma_{21}}{M_{12} - \frac{i}{2}\Gamma_{12}} = \frac{M_{12}^\star - \frac{i}{2}\Gamma_{12}^\star}{M_{12} - \frac{i}{2}\Gamma_{12}}. \tag{1.21}$$

As previously stated, $|N_1\rangle$ and $|N_2\rangle$ are the mass eigenstates, with masses $M_{1,2}$ and decay widths $\Gamma_{1,2}$. In the limit of *CP* symmetry, $|N_1\rangle$ is the *CP*-even eigenstate, while $|N_2\rangle$ is the *CP*-odd eigenstate. As $|N_{1,2}\rangle$ are the eigenstates of the Hamiltonian, $\mathscr{H}$, we can express the eigenvalues, $\lambda_{1,2}$ of the eigenvectors $|N_{1,2}\rangle$ in terms of their masses and decay widths,

$$\lambda_1 \equiv M_1 - i\frac{\Gamma_1}{2} = M_{11} - i\frac{\Gamma_{11}}{2} + \frac{q}{p}\left(M_{12} - i\frac{\Gamma_{12}}{2}\right), \tag{1.22}$$

$$\lambda_2 \equiv M_2 - i\frac{\Gamma_2}{2} = M_{22} - i\frac{\Gamma_{22}}{2} - \frac{q}{p}\left(M_{12} - i\frac{\Gamma_{12}}{2}\right). \tag{1.23}$$

The differences between the masses and the widths of the mass eigenstates,

$$\Delta M = M_1 - M_2, \tag{1.24}$$

$$\Delta\Gamma = \Gamma_1 - \Gamma_2. \tag{1.25}$$

Here we take M_1 to be the greater of the two masses, thus ΔM is semi positive-definite. These parameters can be expressed in terms of dimensionless observable *mixing parameters* of neutral meson mixing,

$$x = \frac{\Delta M}{\Gamma}, \tag{1.26}$$

$$y = \frac{\Delta\Gamma}{2\Gamma}, \tag{1.27}$$

where $\Gamma = \frac{\Gamma_1+\Gamma_2}{\Gamma}$.

Returning to the Schrödinger equation for a quantum state $|\psi(t)\rangle$ [65],

$$i\frac{\partial}{\partial t}|\psi(t)\rangle = \mathscr{H}|\psi(t)\rangle. \tag{1.28}$$

The solution to this equation gives,

$$|\psi(t)\rangle = e^{-i\mathscr{H}t}|\psi(0)\rangle. \tag{1.29}$$

As $|N_{1,2}\rangle$ are the eigenvectors of $\mathscr{H}$, this implies,

$$|N_{1,2}(t)\rangle = e^{-i\lambda_{1,2}t}|N_{1,2}\rangle. \tag{1.30}$$

By using Equation (1.17) to change the basis we obtain,

$$\begin{bmatrix}|N^0(t)\rangle\\|\overline{N}^0(t)\rangle\end{bmatrix} = \mathbf{Q}^{-1}\begin{bmatrix}e^{-i\lambda_1 t} & 0\\ 0 & e^{-i\lambda_2 t}\end{bmatrix}\mathbf{Q}\begin{bmatrix}|N^0\rangle\\|\overline{N}^0\rangle\end{bmatrix} = \begin{bmatrix}g_+(t) & \frac{q}{p}g_-(t)\\ \frac{p}{q}g_-(t) & g_+(t)\end{bmatrix}\begin{bmatrix}|N^0\rangle\\|\overline{N}^0\rangle\end{bmatrix}. \tag{1.31}$$

Writing out the terms gives,

$$|N^0(t)\rangle = g_+(t)\,|N^0\rangle + \frac{q}{p}g_-(t)\,|\overline{N}^0\rangle, \tag{1.32}$$

$$|\overline{N}^0(t)\rangle = \frac{p}{q}g_-(t)\,|N^0\rangle + g_+(t)\,|\overline{N}^0\rangle, \tag{1.33}$$

where $N^0(t)$ means the state at time t of a meson which was N^0 at time 0, and similarly for $\overline{N}^0(t)$. The coefficients $g_\pm(t)$ are given by,

$$g_\pm(t) = \frac{e^{-i\lambda_1 t} \pm e^{-i\lambda_2 t}}{2}. \tag{1.34}$$

From Equations (1.32) and (1.33), we are able to calculate the probabilities of an initially produced N^0 evolving into a given state at time t,

$$\mathbb{P}\big(N^0 \to N^0, t\big) = \left|\langle N^0(t)\,|N^0\rangle\right|^2 = |g_+(t)|^2\,, \tag{1.35}$$

$$\mathbb{P}\Big(N^0 \to \overline{N}^0, t\Big) = \left|\langle N^0(t)\,|\overline{N}^0\rangle\right|^2 = \left|\frac{q}{p}\right|^2 |g_-(t)|^2\,. \tag{1.36}$$

Similarly for $\overline{N}^0$,

$$\mathbb{P}\Big(\overline{N}^0 \to \overline{N}^0, t\Big) = \left|\langle \overline{N}^0(t)\,|\overline{N}^0\rangle\right|^2 = |g_+(t)|^2\,, \tag{1.37}$$

$$\mathbb{P}\Big(\overline{N}^0 \to N^0, t\Big) = \left|\langle \overline{N}^0(t)\,|N^0\rangle\right|^2 = \left|\frac{q}{p}\right|^2 |g_-(t)|^2\,. \tag{1.38}$$

The $|g_\pm(t)|^2$ terms can also be expressed in terms of the mixing parameters, x and y,

$$|g_\pm(t)|^2 = \frac{e^{-\Gamma t}}{2}\left(\cosh\left(y\Gamma t\right) \pm \cos\left(x\Gamma t\right)\right). \tag{1.39}$$

System	x	y
$K^0 - \overline{K}^0$	-0.946 ± 0.004	0.99650 ± 0.00001
$D^0 - \overline{D}^0$	$\left(4.09^{+0.48}_{-0.49}\right) \times 10^{-3}$	$\left(6.15^{+0.56}_{-0.55}\right) \times 10^{-3}$
$B^0 - \overline{B}^0$	0.769 ± 0.004	$(0.1 \pm 1.0) \times 10^{-2}$
$B_s^0 - \overline{B}_s^0$	26.89 ± 0.07	$(12.9 \pm 0.6) \times 10^{-2}$

Table 1.1: *The experimental status of the measurements of the mixing parameters x and y [69].*

From Equations (1.35) and (1.37) it is clear that the probability of a $N^0 \to N^0$ process is equal to that of a $\overline{N}^0 \to \overline{N}^0$ process, the probability being $|g_+(t)|^2$. However if $|q/p|^2 \neq 1$, then the $N^0 \to \overline{N}^0$ and $\overline{N}^0 \to N^0$ process do not have the same probability. This is *CP* violation in mixing which will be expanded upon in this thesis.

Neutral meson mixing is described by the observables, x and y, and differences in these values among mesons results in vastly different behaviors. The differences between the K^0, D^0, B^0, and B_s^0 meson systems can be seen in Fig. 1.6. The B_s^0 system has the highest frequency oscillations and differs significantly from the D^0 system which has, by a long way, the lowest frequency of oscillations. This is due to the D^0 system having a very small mass difference between the mass eigenstates D_1 and D_2, so small that it was only recently observable as non-zero at the current levels of experimental precision [68].

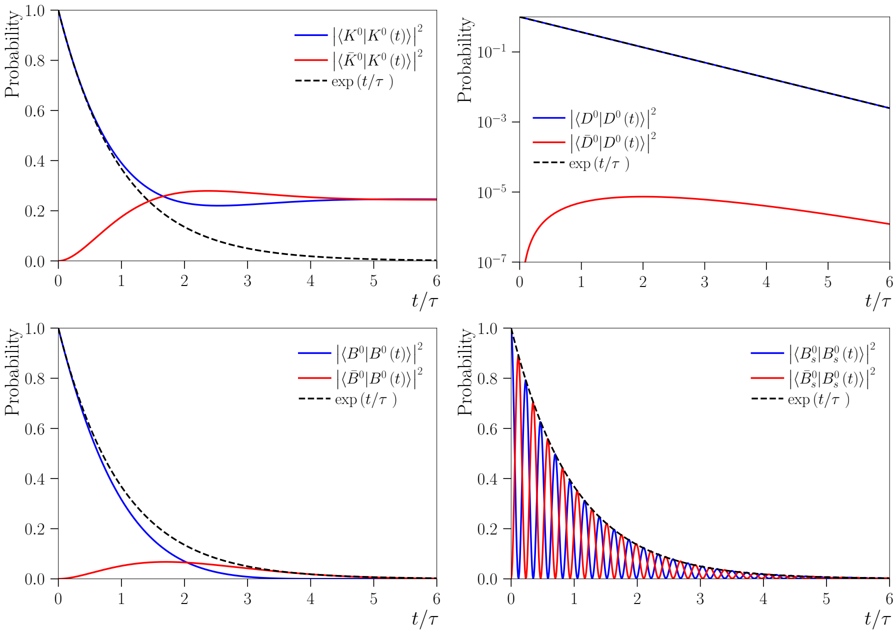

Figure 1.6: *Neutral meson oscillations for the K^0 (top left), D^0 (top right), B^0 (bottom left) and B_s^0 (bottom right) decays. The evolution of the probability is depicted as the function of dimensionless variable t/τ, the decay time unit of the meson. An exponential decay curve not subject to any oscillations is also drawn in a dotted line for comparison. Note for the D^0 meson oscillations, it is a semilog plot due in order to show the very slow oscillations.*

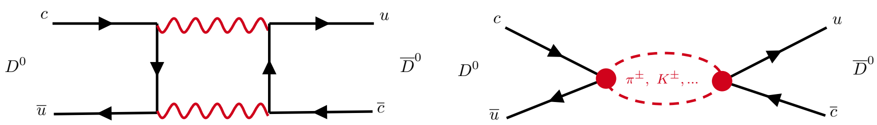

Figure 1.7: $D^0 - \overline{D}^0$ *mixing corresponding to short distance contributions (left) and long distance contributions (right).*

1.5 *CP* violation

The decay amplitude of a D^0 or $\overline{D}^0$ meson to a final state f or $\overline{f}$ is defined as,

$$\begin{aligned} A_f &= \langle f|\mathscr{H}|D^0\rangle, \quad A_{\overline{f}} = \langle \overline{f}|\mathscr{H}|D^0\rangle, \\ \overline{A}_f &= \langle f|\mathscr{H}|\overline{D}^0\rangle, \quad \overline{A}_{\overline{f}} = \langle \overline{f}|\mathscr{H}|\overline{D}^0\rangle. \end{aligned} \tag{1.40}$$

There are multiple Feynman diagrams to reach the same final state. These all need to be added coherently together to produce the total amplitude. Thus the decay amplitudes A_f and $\overline{A}_f$ can be expanded as a series of decay amplitudes,

$$\begin{aligned} A_f &= \sum_k \left|A_f^k\right| e^{i\delta_f^k} e^{i\phi_f^k}, \\ \overline{A}_f &= \sum_k \left|A_f^k\right| e^{i\delta_f^k} e^{-i\phi_f,^k}. \end{aligned} \tag{1.41}$$

Where $\left|A_f^k\right|$ are the magnitudes of the decay amplitudes for each order k. The ϕ_f^k elements are the *weak phases*, which arise from the CKM mechanism that describes electroweak physics. Weak phases change sign under a *CP* transformation. The δ_f^k elements are the *strong phases*, originating from strong interaction processes happening through contributions of intermediate on-shell states in the decay process. These phases do not undergo a sign change under a *CP* transformation.

There are three different and distinct mechanisms through which *CP* violation can occur: *CP* violation in the decay, through mixing, and in the interference between mixing and decay.

CP violation in the decay

By taking Equation (1.41) and restricting it to the first two amplitude terms ($k \in [1, 2]$), the difference between the squared amplitudes $|A_f|^2$ and $\left|\overline{A}_{\overline{f}}\right|^2$ can be written as,

$$|A_f|^2 - \left|\overline{A}_{\overline{f}}\right|^2 = -4\left|A_f^1\right|\left|A_f^2\right| \sin\left(\delta_f^1 - \delta_f^2\right) \sin\left(\phi_f^1 - \phi_f^2\right). \tag{1.42}$$

If $|A_f| \neq \left|\overline{A}_{\overline{f}}\right|$, and both the strong and weak phase difference is non-zero, then *CP* violation can proceed through the decay. This is the only mechanism of *CP* violation that occurs in both charged and neutral hadrons.

Experimentally, *CP* violation in the decay is measured by estimating the asymmetry of the decay time integrated decay widths, Γ, of D^0 decays to a final state f and $\overline{D}^0$ decays to a final state $\overline{f}$. As $\Gamma\left(D^0 \to f\right) \propto |A_f|^2$ and a similar relation holds for $\overline{D}^0 \to \overline{f}$, the asymmetry is given by,

$$A_{CP}(f) = \frac{\Gamma\left(D^0 \to f\right) - \Gamma\left(\overline{D}^0 \to \overline{f}\right)}{\Gamma\left(D^0 \to f\right) + \Gamma\left(\overline{D}^0 \to \overline{f}\right)} = \frac{|A_f|^2 - \left|\overline{A}_{\overline{f}}\right|^2}{|A_f|^2 + \left|\overline{A}_{\overline{f}}\right|^2} \tag{1.43}$$

Thus when $A_{CP}(f) \neq 0$, then $|A_f|^2 - \left|\overline{A}_{\overline{f}}\right|^2 \neq 0$, and *CP* violation has occurred in the decay.

For charm decays, *CP* violation in the decay was observed by the LHCb collaboration in 2019 through the measurement of $\Delta A_{CP} = A_{CP}(KK) - A_{CP}(\pi\pi)$. [27, 70, 71]. The measurement was performed by studying the difference in $A_{CP}(f)$ between two D^0 decays: $D^0 \to K^+K^-$ and $D^0 \to \pi^+\pi^-$. The resulting measurement in the difference of the asymmetries was, $\Delta A_{CP} = (-15.4 \pm 2.9) \times 10^{-4}$, corresponding to a tension between ΔA_{CP} and zero of 5.3σ. Another measurement of $A_{CP}(K^-K^+)$ and ΔA_{CP} in 2022 by the LHCb collaboration, indicates that the *CP* violation is coming from the $D^0 \to \pi^-\pi^+$ decay, at a significance of 3.8σ [72]. So far *CP* violation in the decay remains the only observed *CP* violation in the charm sector.

CP violation through mixing

CP violation through mixing occurs when the probability of a $D^0 \to \overline{D}^0$ process is not equal to the probability of a $\overline{D}^0 \to D^0$ process. This occurs when,

$$\left|\frac{q}{p}\right| - 1 \neq 0. \tag{1.44}$$

CP violation in the interference between mixing and decay

The final mechanism for *CP* violation to occur is through interference between the mixing amplitude and the decay amplitude. For this, the D^0 and the $\overline{D}^0$ meson must share the final state ($f = \overline{f}$). This occurs when the decay amplitude for the $D^0 \to f$ process interferes with the decay amplitude for the $D^0 \to \overline{D}^0 \to f$ process and induces *CP* violation. Mathematically it is expressed as,

$$\phi_{\lambda_f} = \arg(\lambda_f) = \arg\left(\frac{q}{p}\frac{\overline{A}_f}{A_f}\right) \neq 0, \quad \text{where } \lambda_f = \frac{q}{p}\frac{\overline{A}_f}{A_f}. \tag{1.45}$$

Using this we can now look to y_{CP}, the parameter that is measured in this thesis. Start by defining the *effective decay width* [66] [8],

$$\begin{aligned}
\hat{\Gamma}\left(D^0 \to f\right) &= \Gamma \cdot \left[1 + \left|\frac{q}{p}\right| \left|\frac{\overline{A}_f}{A_f}\right| \left(y \cos\phi_{\lambda_f} - x \sin\phi_{\lambda_f}\right)\right], \\
\hat{\Gamma}\left(\overline{D}^0 \to f\right) &= \Gamma \cdot \left[1 + \left|\frac{q}{p}\right| \left|\frac{A_f}{\overline{A}_f}\right| \left(y \cos\phi_{\lambda_f} + x \sin\phi_{\lambda_f}\right)\right].
\end{aligned} \tag{1.46}$$

Now define two variables,

$$c_f^{\pm} = \left|\frac{q}{p}\right| \left|\frac{\overline{A}_f}{A_f}\right|^{\pm 1} \left(-y \cos\phi_{\lambda_f} \pm x \sin\phi_{\lambda_f}\right) \approx -y \pm x\phi_{\lambda_f} \pm y \left[a_f^d - \left(\left|\frac{q}{p}\right| - 1\right)\right], \tag{1.47}$$

where

$$a_f^d = \frac{\left|A_f\right|^2 - \left|\overline{A}_f\right|^2}{\left|A_f\right|^2 + \left|\overline{A}_f\right|^2} \approx 1 - \left|\frac{\overline{A}_f}{A_f}\right|^2. \tag{1.48}$$

Using the expression for $c_f^{\pm}$ the effective decay widths can be written as,

$$\begin{aligned}
\hat{\Gamma}\left(D^0 \to f\right) &= \Gamma \cdot \left[1 + c_f^{+}\right], \\
\hat{\Gamma}\left(\overline{D}^0 \to f\right) &= \Gamma \cdot \left[1 - c_f^{-}\right].
\end{aligned} \tag{1.49}$$

It is useful to define an experimentally measurable *CP*-violating obersvable y_{CP}^f as,

Now we can define the *CP*-violating observable y_{CP}^f as,

$$\begin{aligned}
y_{CP}^f &= \frac{\hat{\Gamma}\left(D^0 \to f\right) + \hat{\Gamma}\left(\overline{D}^0 \to f\right)}{2\Gamma} \\
&= \frac{c_f^{+} + c_f^{-}}{2} \\
&= \left(\left|\frac{q}{p}\right| \left|\frac{\overline{A}_f}{A_f}\right| + \left|\frac{p}{q}\right| \left|\frac{A_f}{\overline{A}_f}\right|\right) \frac{y}{2} \cos\phi_{\lambda_f} - \left(\left|\frac{q}{p}\right| \left|\frac{\overline{A}_f}{A_f}\right| - \left|\frac{p}{q}\right| \left|\frac{A_f}{\overline{A}_f}\right|\right) \frac{x}{2} \sin\phi_{\lambda_f}.
\end{aligned} \tag{1.50}$$

In the limit of no *CP* violation then it can be seen that $y_{CP} = y$. Thus any significant departure in the measurement of y_{CP} from y would be in indication of *CP* violation through mixing and in the interference between mixing and decay.

[8] *Effective decay times* are defined as $\hat{\tau} = 1/\hat{\Gamma}$

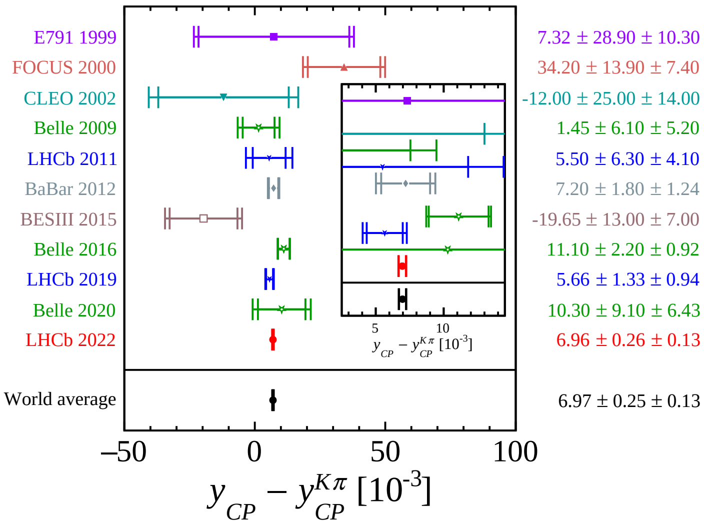

Figure 1.8: *The world average value for y_{CP}, including the most recent LHCb measurement [74].*

1.6 Status of y_{CP}

The current experimental world average measured value of y_{CP} is [73] [9],

$$y_{CP} - y_{CP}^{K\pi} = (0.697 \pm 0.028)\,\%. \tag{1.51}$$

This includes a recent measurement by the LHCb collaboration in which the result for y_{CP} is given in the above form [74]. Before the inclusion of this analysis, which substantially improved the precision on the world average value for y_{CP}, the world average value was [75], $y_{CP} = (7.19 \pm 1.13) \times 10^{-3}$, and the experimental knowledge of y_{CP} is shown in Figs. 1.8 and 1.9.

y_{CP} has been measured experimentally multiple times by multiple collaborations. Each measurement is performed with a different data sample and using different techniques. The first measurements were performed at Fermilab by the E791 and FOCUS collaborations. The E791 collaboration was based on the interaction of a π^- beam on a platinum-diamond fixed target. In 1999, it measured the y_{CP} through the measurement of lifetimes of $D^0 \to K^+K^-$ and $D^0 \to K^-\pi^+$ decays [76]. This was followed by a measurement by the FOCUS collaboration, a charm photoproduction experiment at Fermilab. In 2000 it performed a measurement of y_{CP} in a similar fashion to the E791 collaboration [77].

CLEO was a particle physics experiment based at the Cornell Electron Storage Ring (CESR), collecting data from e^+e^- collisions that produced B meson

[9] $y_{CP}^{K\pi} \sim -\sqrt{R_D}\, y_{12} \approx -3.5 \times 10^{-4}$

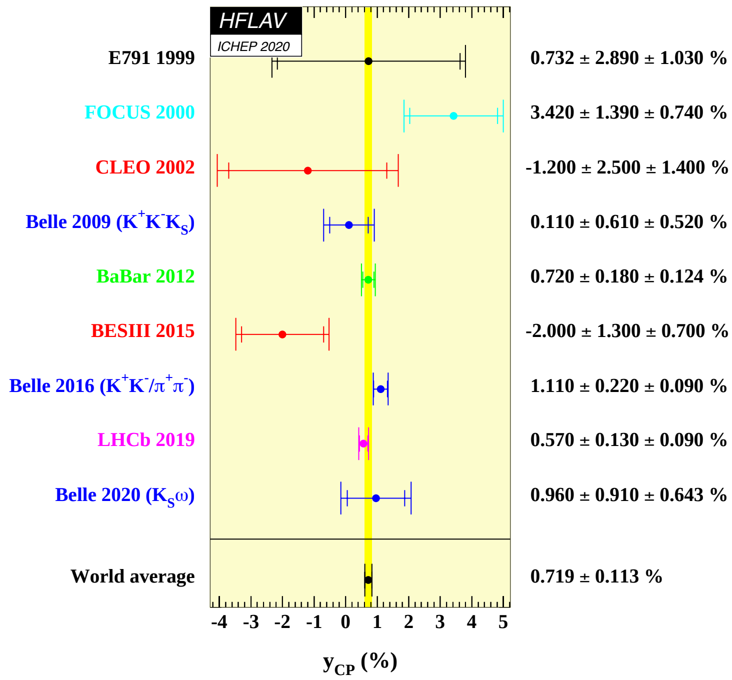

Figure 1.9: *The world average value for y_{CP} up to Summer 2020 [75].*

decays. In 2001, CLEO measured y_{CP} by estimating the lifetime difference between the $D^0 \to K^+K^-$ (or $D^0 \to \pi^+\pi^-$) and $D^0 \to K^-\pi^+$ final states [78].

The Belle experiment was a B meson factory at the High Energy Accelerator Research Organisation (KEK) in Tsukuba (Japan). It took data between 1999 and 2010 from asymmetric e^+e^- collisions at the centre-of-momentum energy equal to the mass of the $\Upsilon(4S)$ resonance. The Belle experiment has measured y_{CP} three times, in 2009, 2016, and 2020. The first measurement was based on comparing mean decay times for different regions of the three-body phase-space distribution using an untagged $D^0 \to K^0_S K^+K^-$ sample. This measurement used $673\,\mathrm{fb}^{-1}$ of data and yielded $y_{CP} = (+0.11 \pm 0.61\,(\mathrm{stat}) \pm 0.52\,(\mathrm{syst}))\,\%$ [31]. This technique is the basis of the analysis method employed and described in this thesis. The subsequent measurements by the Belle experiment published in 2016 used $D^0 \to K^+K^-$ and $D^0 \to \pi^+\pi^-$ decays and the full Belle dataset, giving the most precise estimate of y_{CP} by the Belle experiment with an uncertainty of about 2×10^{-3} [79]. Finally in 2020 y_{CP} was again measured by the Belle experiment using the CP-odd $D^0 \to K^0_S\omega$ decay [80].

One measurement of y_{CP} has been performed by the BaBar experiment in 2012. The BaBar experiment was a B meson factory based at the SLAC National Accelerator Laboratory on the Stanford campus in the US. Similarly

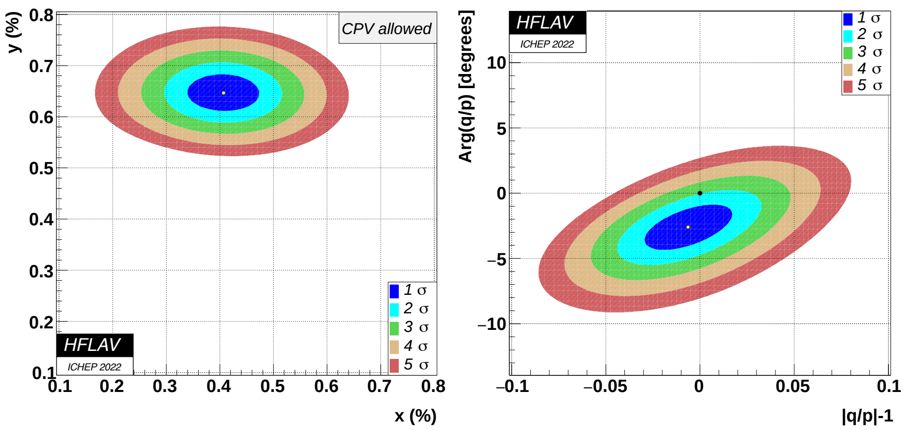

Figure 1.10: *Experimental status of x, y, q, and p as of Summer 2022 [73].*

to the Belle experiment, it analysed data from e^+e^- collisions at the $\Upsilon(4S)$ resonance energy. The BaBar experiment measured y_{CP} by measuring the lifetimes of the $D^0 \to K^+K^-$, $D^0 \to \pi^+\pi^-$, and $D^0 \to K^-\pi^+$ decays [81].

The Beijing Spectrometer III (BESIII) experiment performed a measurement of y_{CP} in 2015. The BESIII experiment collects data from e^+e^- collisions at the Beijing Electron- Positron Collider II (BEPCII) collider with a collision energy between 2 and 4.63 GeV. In the measurement of y_{CP}, D^0 candidates are obtained from the pair production, $e^+e^- \to \gamma \to D^0\overline{D}^0$. One D decay is tagged to a *CP*-eigenstate while the other is tagged to a semi-leptonic decay. The parameter y_{CP} is then estimated by comparing the branching fractions of semi-leptonic D decays to the branching fractions of D decays to *CP*-even eigenstates [82].

The final experiment to have performed a measurement of y_{CP} is the LHCb collaboration. In both measurements, $D^0 \to K^+K^-$, $D^0 \to \pi^+\pi^-$, and $D^0 \to K^-\pi^+$ decays are studied. At LHCb it is very difficult to measure y_{CP} through direct measurements of decay lifetimes, due to a selection to remove background being dependent on the D^0 flight distance which heavily biases the D^0 decay time. However y_{CP} is only sensitive to the difference of decays times between $D^0 \to K^+\pi^+$ and Cabibbo surpressed decays. This is measured in both 2019 [83] and recently in 2022 [74], with the latter measurement significantly improving the precision of the world average value of y_{CP}.

2 Experimental setup

2.1 The Large Hadron Collider at CERN

The European Organization for Nuclear Research (*Conseil europeen pour la recherche nucleaire*, CERN) is a research laboratory hosting the current largest particle physics collider in the world, the Large Hadron Collider, LHC. The LHC is the last in a chain of accelerators, as shown in Fig. 2.1, which successively increase the energy of the protons in the machine. The other accelerators are:

- The Linear accelerator (LINAC) 2 accelerates protons, extracted from hydrogen gas, up to an energy of 50 MeV.
- The Proton Synchrotron Booster (Booster) accelerates protons up to 1.4 GeV.
- The Proton Synchrotron (PS) accelerates the protons further, to an energy of 25 GeV.
- The final non-LHC component, the Super Proton Synchrotron (SPS), accelerates the protons up to an energy of 450 GeV.
- Protons are injected, in two counter-rotating beams, into the LHC, where they are accelerated to their final energy.

The LHC operates with a nominal number of proton bunches of about 2800 per beam, where each bunch consists of about 10^{11} protons. Once the beams have been accelerated to their required final energy, the two counter-rotating beams are focused to collide at four pp interaction points, each one corresponding to a dedicated physics experiment:

- The ATLAS and CMS are 4π experiments that are particularly interested in the direct production and detection of New Physics candidates [85,86].
- ALICE is a 4π detector, which exploits heavy ion collisions to study quark gluon plasma [87].

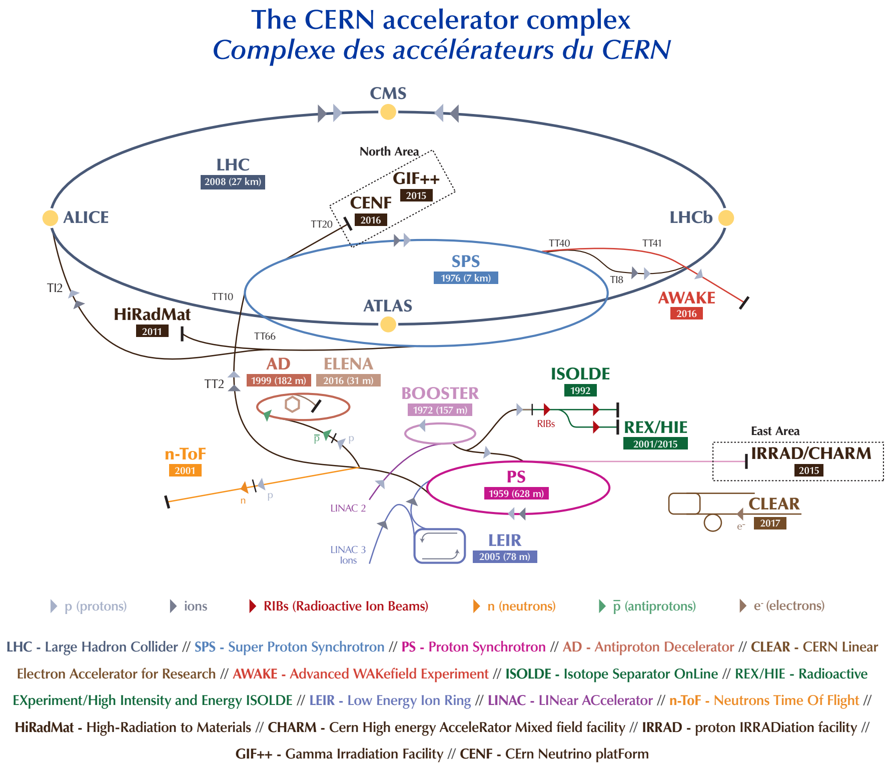

Figure 2.1: *The CERN accelerator complex [84].*

- LHCb is forward spectrometer and a specialist b and c hadron factory, searching for indirect signs of New Physics by performing high precision comparisons of experimental observables with SM predictions [88].

2.2 LHCb Detector

The LHCb detector [88, 89] is a single-arm forward spectrometer covering the pseudorapidity range $2 < \eta < 5$, designed for the study of particles containing b or c quarks. The pseudorapidity is defined as,

$$\eta = -\ln\left(\tan\frac{\theta}{2}\right) = \text{atanh}\left(\frac{p_z}{|\vec{p}|}\right), \tag{2.1}$$

where θ is the angle between momentum of the produced particle and the beam axis (z-axis). The LHCb detector covers the range $2 < \eta < 5$, which is optimised for b-hadron production at the LHC. Tracks with $\eta > 5$ are generally too close to the beam pipe to be reconstructed, and on the other hand tracks with $\eta < 2$ are outside the external boundaries of the detector. The narrow pseudorapidity range is motivated by the fact that $b\bar{b}$ and $c\bar{c}$ pairs are predominantly produced in these forward and backward regions, as shown in Figs. 2.2 and 2.3.

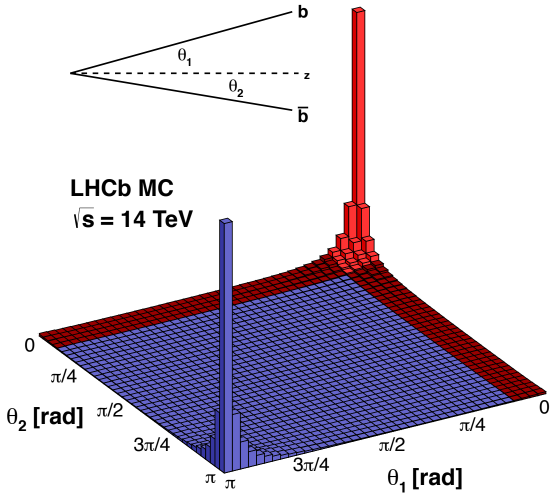

Figure 2.2: *$b\bar{b}$ production angles at the LHC centre-of-mass energy of 14 TeV. The red region shows the 2D region covered by the LHCb acceptance [90].*

The LHCb experiment operates at a lower instantaneous luminosity with respect to the one offered by the LHC. A beam focusing lens is employed to reduce the instantaneous luminosity from $\mathscr{L} = 1 \times 10^{34}\,\mathrm{cm}^{-2}\,\mathrm{s}^{-1}$ to $\mathscr{L} = 4 \times 10^{32}\,\mathrm{cm}^{-2}\,\mathrm{s}^{-1}$ at the pp interaction point. This reduces the number of pp interactions per event, called *pile-up*. For the LHCb detector the average pile-up is around 1, depending on year and running conditions. It is a carefully considered design choice to reduce the pile-up in events. In order to make highly precise measurements of hadrons containing b or c quarks, excellent vertex reconstruction is needed. Increased pile-up in the interaction point would make these measurements difficult and computationally less efficient. The LHCb detector collected data for physics analysis during *Run I* (2010-2012) at a center of mass energy of $\sqrt{s} = 7 - 8\,\mathrm{TeV}$ and *Run II* at $\sqrt{s} = 13\,\mathrm{TeV}$. The corresponding integrated luminosity is shown in Fig. 2.4.

The LHCb detector is shown in Fig. 2.5. It is constructed from a series of subdetectors, each of which has a specific function, and the information from each subdetector is combined to construct the event.

- The *Vertex Locator* (VELO) is placed at the pp interaction point, and consists of 42 silicon detector elements with the aim of reconstructing the

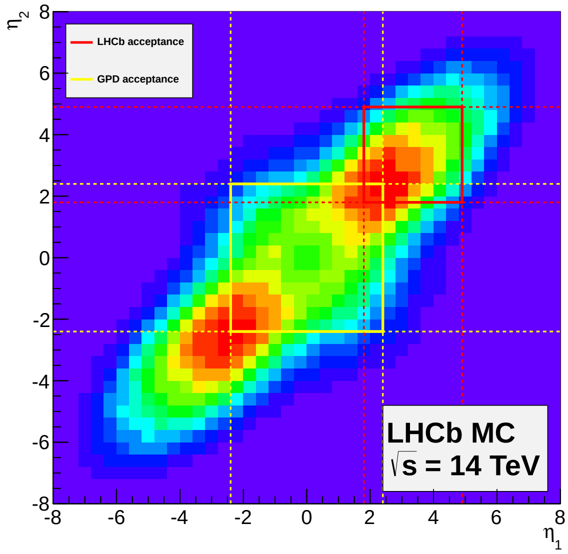

Figure 2.3: *Pseudorapidity acceptance of the LHCb detector and a General Purpose Detector (GPD), such as ATLAS or CMS, at the LHC centre-of-mass energy of 14 TeV [90].*

decay vertices of particles.

- The *Ring Imaging Cherenkov* (RICH-1) detector provides information relating to the identity of the particles leaving the VELO.
- The *Tracking Turicensis* (TT) is the first of the tracking stations, placed before the dipole magnet.
- The *Dipole Magnet* creates a 4 Tm magnetic field, whose main component is directed across the y-axis with regular polarity changes. This causes a charged particle traveling in the z-direction to be deflected in the x-direction.
- The three *Tracking Stations*, (T1, T2, and T3) and the *Inner Tracker* (IT) are placed after the dipole magnet. Their purpose is to precisely reconstruct the tracks of charged particles and determine their momenta.
- The second RICH detector (RICH-2) covers a higher momenta range with respect to RICH-1.
- The *Electromagnetic Calorimeter* (ECAL) measures the energies of electrons and photons.
- The *Hadronic Calorimeter* (HCAL) measures the energies of hadrons.

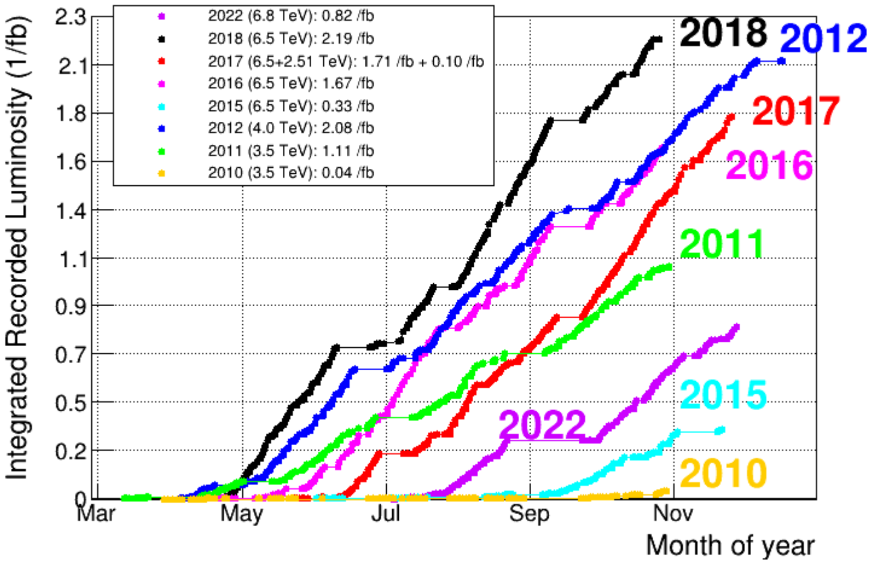

Figure 2.4: *Cumulative integrated luminosity for each separate data-taking year as recorded by the LHCb detector [91].*

- The five *Muon Stations* (M1-M5) are used to detect and identify muons.

The subdetectors can broadly be divided into two subgroups, the *tracking system* and the *particle identification system.* These are described in more detail in Section 2.2.

The tracking system

The LHCb tracking system consists of the VELO, the dipole magnet and all the trackers (TT, T1, T2, T3, and IT). Charged particles leave a *hit* when they pass through the VELO and trackers. The dipole magnet bends the trajectory of the particles, allowing their charge and momentum to be reconstructed.

The Vertex Locator

The VErtex LOcator (VELO) [92] is a silicon micro-strip detector placed around the pp interaction point. It covers $\sim$ 1 metre along the beam line. The main purpose of the VELO detector is to locate and reconstruct, with a high precision, the position of the *primary vertex* (PV) and the position of the decays of hadrons produced at the PV, called *secondary vertices* (SV). The precise identification of the PV and SV are crucial to the LHCb physics program as the b- and c-hadrons are formed at the PV and decay at the SV.

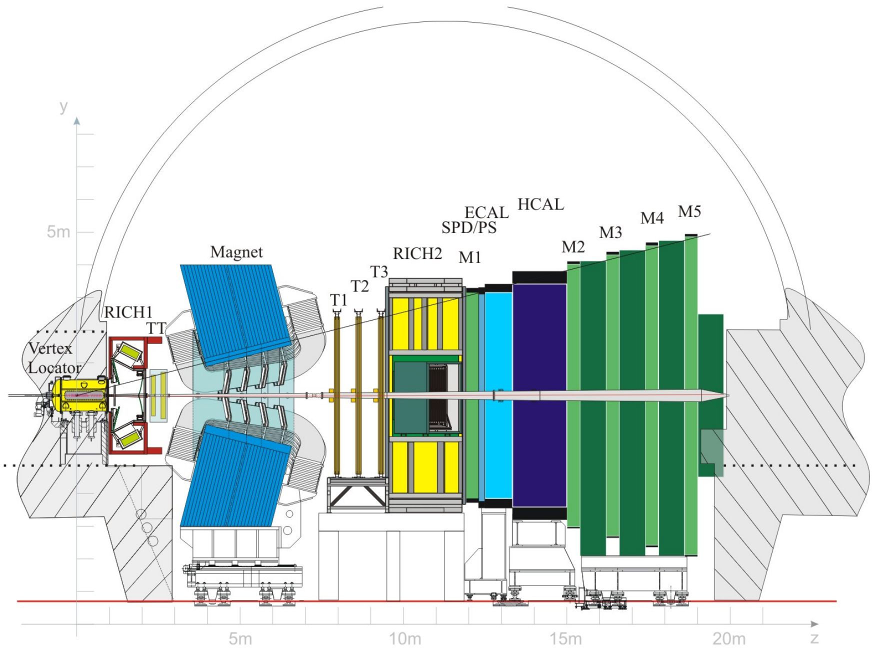

Figure 2.5: *Schematic side view of the LHCb detector [88].*

The VELO is contructed in two halves, each comprising an array of semicircular sesnors perpendicular to the beam. It is built from 21 modules that measure the azimuthal angle, Φ, and radial distance, r, of the particle hits, while z is given by the position of the module, giving a 3D localization of the hits.

The detector is operated in two configurations depending on conditions. While the beam is injected into the beam pipe, the two semicircular pieces of the VELO modules are kept as a safe distance of 29 mm with respect to the beam line in order to protect the detector from radiation damage. This is referred to as the *open* position. During data acquisition the detector is then placed in the *closed* position, at about 8mm from the beamline, as shown in Fig. 2.6. In the closed position there is a slight overlap between the two semicircular modules to ensure full angular coverage [93].

The dipole magnet

The LHCb dipole magnet [94] is a non-superconducting dipole magnet that is placed between the TT and T1. Its purpose is to bend the trajectory of charged particles in the xz plane by generating an integrated magnetic field of 4 Tm for tracks in the region $z \in [0, 10]$ m

The LHCb detector is not perfectly symmetrical along the x-axis. Therefore in order to avoid any unwanted detection asymmetries, the polarity of

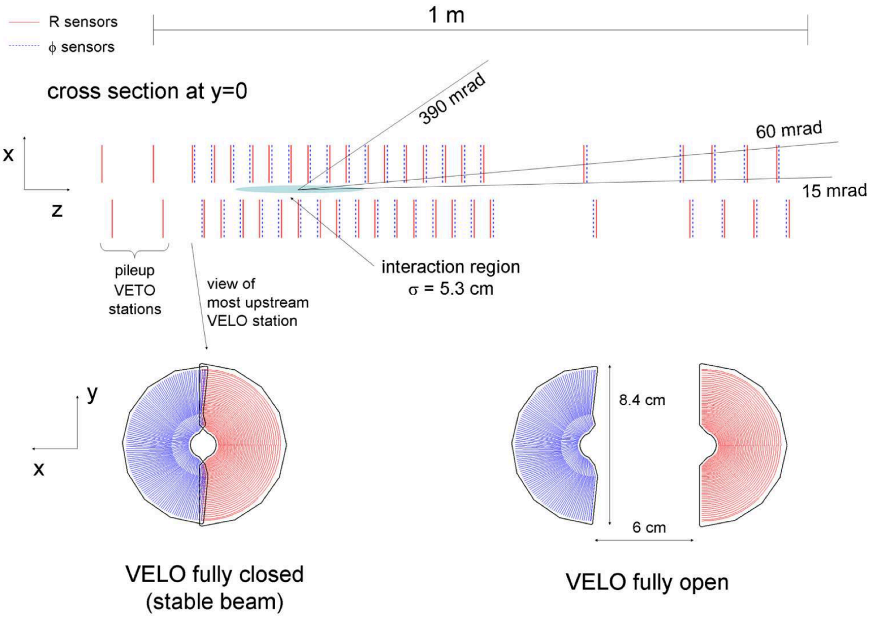

Figure 2.6: *Layout of the VELO circular modules [88].*

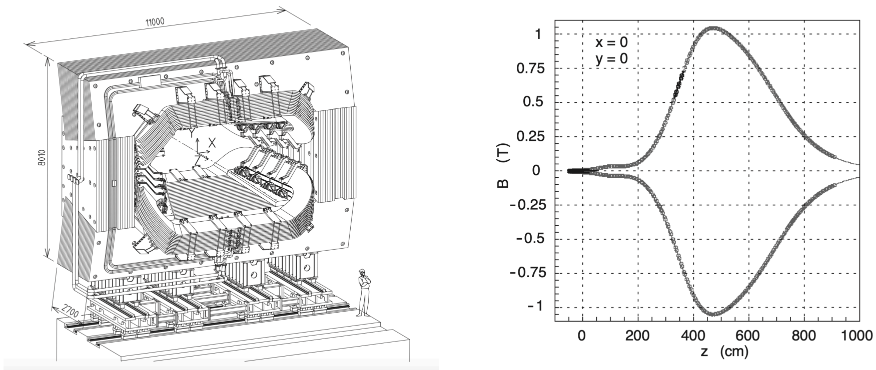

Figure 2.7: *Left: Drawing of the LHCb dipole magnet. Right: Magnitude of the B-field along the z-axis. Figures taken from Ref. [88].*

the magnet is regularly inverted during data taking. The $\vec{B}$ field projection along the y-axis can be positive, referred to as *MagUp*, or negative along the y direction, *MagDown*. Typically the polarity is inverted biannually during data taking, resulting in two distinct data samples, corresponding to the MagUp and MagDown polarity orientations.

The tracking stations

The tracking stations are modules designed to track the passage of a charged particle traversing the detector.

The **Tracking Turicensis (TT)** [94] is located upstream of the dipole magnet and built from four silicon micro-strip layers with an active area of $8.4\,\mathrm{m}^2$, covering a pseudorapidity of $2.0 < \eta < 4.9$. The four layers are rotated by 0°C, +5°C, −5°C, and 0°C in the xy plane as shown in Fig. 2.8. It is optimised to detect low momentum tracks deflected outside the LHCb acceptance by the dipole magnet and tracks of long lived particles that decay outside of the VELO. The system provides a measurement of the momentum of a charged particle through its curvature.

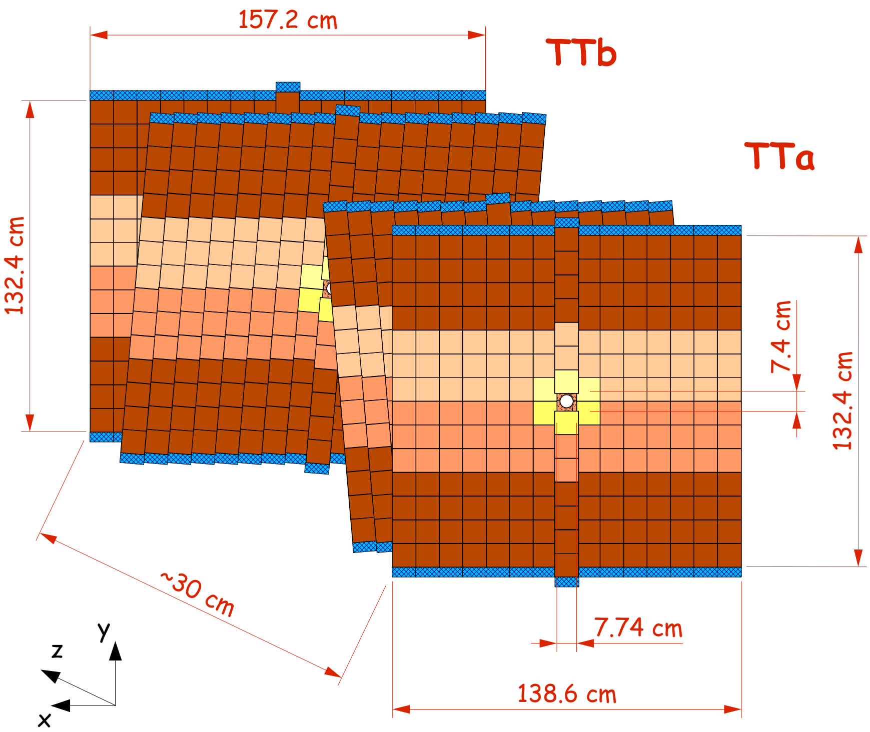

Figure 2.8: *Layout of the racking Turicensis stations [95].*

The **Inner Tracker IT** [96] and **Outer Tracker OT** [97, 98] stations are the three downstream tracking modules (T1-T3), located after the magnet, as shown in Fig. 2.5. The IT is designed similarly to the TT, it is constructed from four silicon micro-strip layers, with two of the layers titled at an angle of ±5°C, to allow for 3D reconstruction of tracks. The IT is specifically designed to detect charged particles in the high track density region around the beam pipe, downstream of the magnet. It covers an acceptance of $3.4 < \eta < 5.0$, and although it only covers 1.3% of the surface of the OT, it processes around 20% of the tracks due to the high track density in the region it covers. The OT is constructed to envelop the IT subdetector and is a gaseous straw tube detector. Each tube is filled with a mixture of Argon (70%), CO_2 (28.5%), and O_2 (1.5%). 64 straw tubes are glued together to form modules which are arranged in forms of two layers. Groups of four layers are called stations, and similarly to the IT and TT, two of the layers are tilted at $\pm 5°$C. Collectively the IT and OT are arranged into three stations (T1-T3), with each station consisting of four layers of IT and OT modules, having orientations as described.

Track reconstruction

Reconstructed tracks from the LHCb tracking system are split into various *track types* depending on what subdetectors of the tracking system they interact with:

- A *VELO track* is reconstructed from the VELO hits only.
- A *long track* is reconstructed from the whole tracking system.
- A *upstream track* is bent out of the detector acceptance by the magnet before the downstream tracking stations and is only reconstructed by the VELO and TT.
- A *downstream track* is not reconstructed by the VELO, but with every other part of the tracking system.
- A *T track* is only reconstructed from the downstream T stations.

The particle identification system

A precise tracking system is very important to physics analyses but it is not sufficient by itself. It gives important information on vertex locations, charges, and momenta of particles passing through the detector, but we also need to be able to identify, accurately, the types of particles. The particle identification (PID) system consists of two Ring Imaging Cherenkov (RICH) detectors, an electromagnetic calorimeter (ECAL), a hadronic calorimeter (HCAL), and muon stations.

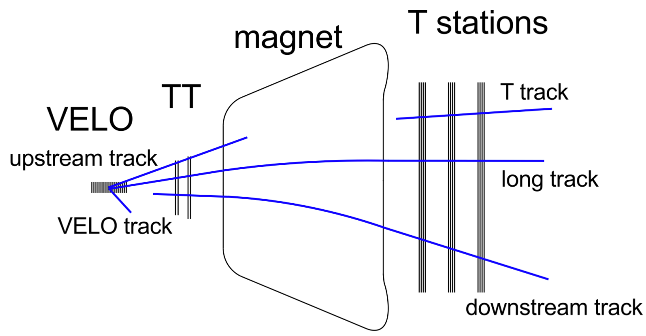

Figure 2.9: *Schematic of track types [99].*

The Ring Imaging Cherenkov detectors

The Ring Imaging Cherenkov (RICH) [100, 101] detectors are based on the *Cherenkov effect*. When a charged particle travels through a medium with a velocity, v, higher than the speed of light in that medium, it emits a cone of light, which is characterized by an angle θ measured with respect to its incident radiation,

$$\cos\theta = \frac{c}{nv}, \tag{2.2}$$

where n is the refractive index of the medium and c is the speed of light in a vacuum. Thus θ is only dependent on the velocity of the particle as c and n are constant. When combined with information from the tracking system, namely the momentum of the particle, the RICH detector can determine the velocity of the particle by measuring θ, giving access to the mass of the particle and its identity.

There are two RICH detectors placed in two parts of the LHCb detector, each covering a different momentum range in order to ensure there is good particle identification across the momentum spectrum. RICH-1 is upstream of the dipole magnet and uses a C_4F_{10} radiator, covering a momentum range of $p \in [0, 60]$ GeV/c. The RICH-2 detector is placed downstream of the dipole magnet, uses a CF_4 radiator, and covers a momentum range of $p \in [50, 100]$ GeV/c.

The calorimeters

The LHCb calorimeters [102,103] provide information of the position and energies of final state particles. They also provides information on neutral particles, such as neutrons, neutral kaons, and photons, which do not interact with the tracking system or the RICH detectors.

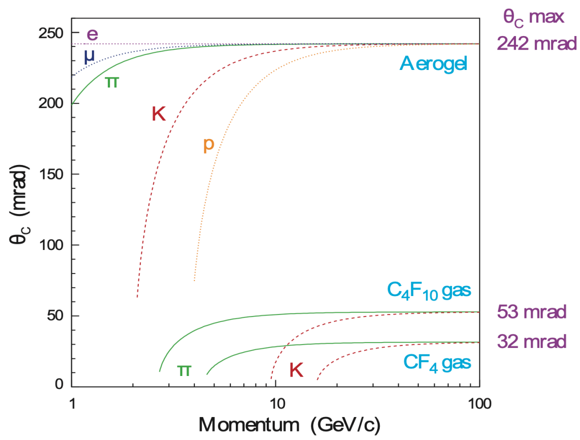

Figure 2.10: *Cherenkov angle versus particle momentum for various gas radiators [88].*

The calorimeter is composed of four main components, which following the z direction are:

- The *Scintillating Pad Detector* (SPD), discriminates between charged and neutral particles, and provides an estimate on the number of tracks.
- A 14mm *lead converter*.
- The *Preshower* detector (PS), allows for adequate separation between electromagnetic and hadronic showers.
- The *Electromagnetic Calorimeter* (ECAL), measures the energy and position of hits of light particles which interact via the electromagnetic interaction, such as electrons or photons.
- The *Hadronic Calorimeter* (HCAL), measures the energy and position of hits of hadronic particles.

The ECAL and HCAL are both constructed from alternating layers of scintillators and layers of dense material (lead for the ECAL, iron for the HCAL). This method induces showers within the calorimeters with different types of particles leaving different signatures in the different subsystems as shown in Fig. 2.11.

The muon system

The muon system [105, 106] consists of five rectangular shaped stations (M1-M5). The main process for electrons to produce energy in the calorimeters is

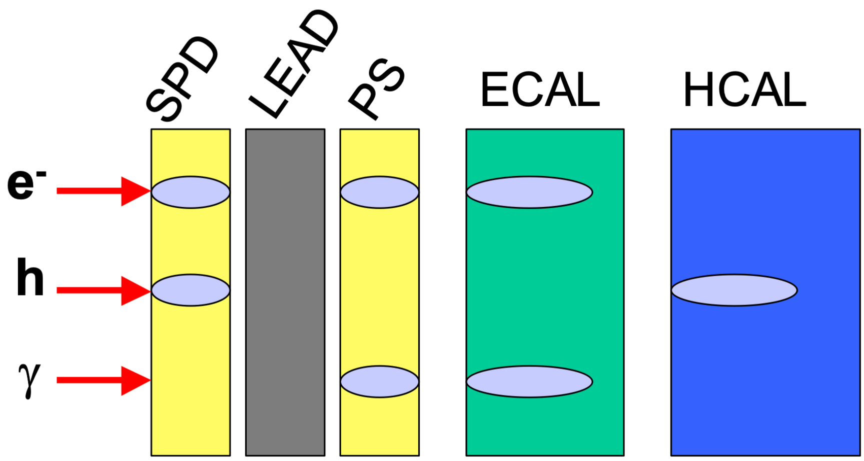

Figure 2.11: *Signatures of an electron, e; a hadron, h; and a photon, γ in the calorimeter system [104].*

Bremsstrahlung, where energy as electromagnetic radiation is emitted when a charged particle is accelerated. The emission power is inversely proportional to the square of the mass of the particle. As the muon is 200 times more massive than the electron, it deposits significantly less energy in the calorimeters. It is also a lepton and therefore does not interact via the strong force.

Muon chambers are thus placed behind the calorimeters to detect the muons. The first chamber (M1) is placed upstream of the calorimeters (but is mainly used for triggering purposes). The rest of the chambers (M2-M5) are placed downstream of the calorimeters, the furthest point away from the interaction point. This is suitable due to the large lifetime of the muon ($c\tau_\mu \approx 700m$) and its low interaction cross section with matter.

The muon chambers are gaseous detectors, composed of alternating layers of iron and multiwire proportional chambers to detect ionization of the gas inside the chamber. The gas is a mixture of Argon (40%), CO_2 (55%), and CF_4 (5%). The inner chamber, M1, is made of Gas Electron Multiplier detectors using Argon (45%), CO_2 (15%), and CF_4 (40%), to withstand the harsh environment due to the high particle occupancy.

Particle indentification variables

The information collected by the particle identification system: the RICH, the calorimeters and the muon chambers can be used to build high level variables. These variables can then be used by the physics analyst to help determine the identity of the particle. Three main algorithms are used:

- The `DLL` algorithm, uses the *delta log-likelihood*. The tracks are by the null hypothesis assumed to be pions, and a log-likelihood difference is calculated between each particle hypothesis and the null hypothesis. Mathematically it is given by,

$$\mathrm{DLL}_X = \ln \mathscr{L}_X - \ln \mathscr{L}_\pi = \ln \left(\frac{\mathscr{L}_X}{\mathscr{L}_\pi} \right). \tag{2.3}$$

Each likelihood is given by the sum of three probability density functions (PDF), one for each of: the RICH system, the calorimeters, and the muon system.

- The `ProbNN` algorithm is a neural network trained to distinguish between the different types of particles. It outputs a score between 0 and 1 for each type of particle, X, giving the probability of the particle having the respective identity.

- The `isMuon` algorithm gives a boolean decision if a track matches hits recorded in the muon system. The exact requirements for hits in the muon system is momentum dependent and summarised in Table 2.1.

Momentum	Hit requirements
$p < 6\,\mathrm{GeV}/c$	M2 + M3
$6\,\mathrm{GeV}/c < p < 10\,\mathrm{GeV}/c$	M2 + M3 + (M4 or M5)
$p > 10\,\mathrm{GeV}/c$	M2 + M3 + M4 + M5

Table 2.1: *Summary of muon hits requirements [105].*

The trigger system

The LHC provides LHCb with *pp* collisions at a rate of 40 million per second (40 MHz). This volume of information is far too much to practically process or store, as it would require storing data to tape at a rate of 1 TB/s. Of the 40 MHz bunch crossing rate, a large majority of the events are of little interest to the physics analyst, whether that be due to common processes already well understood, poor track reconstruction or insufficiently energetic hits. In order to select the events that are of interest to the physics analyst, the LHCb *trigger system* [107] is designed to reduce the rate and select only the most interesting physics events. It broadly consists of two stages, a *hardware trigger*, also referred to as the Level 0, L0, and a *software trigger*, which is split into two High Level Triggers, HLT1 and HLT2. The trigger system is shown in Fig. 2.12.

The trigger system takes the rate from 40 MHz down to a rate of 12.5 kHz which can be stored to tape. Each stage of the trigger is organized into trigger lines that look for different signatures. Any event that does not pass any trigger line at each level is discarded and does not pass to the next level.

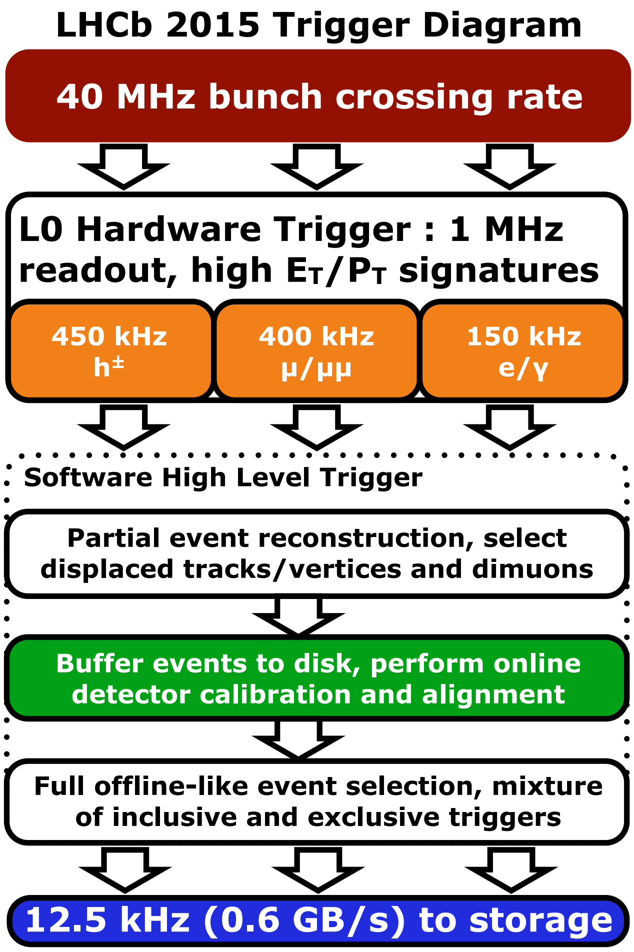

Figure 2.12: *The Run II trigger system for LHCb [108].*

- The **Level 0 (L0)** trigger takes the rate from 40 MHz down to 1 MHz. It is a hardware based trigger that selects events that contain muons or high transverse momentum particles using information read out from the VELO, calorimeters, and muon chambers.

- The **High Level Trigger 1 (HLT1)** trigger is the first of the software based triggers. It reduces the rate coming in from the L0 trigger of 1 MHz down to 50 kHz. It uses a C++ based algorithm to partially reconstruct events using information from all the subdetectors. If events pass a HLT1 line, they are stored in a computing farm before being transferred to the next level.

- The **High Level Trigger 2 (HLT2)** trigger is the second software based trigger and final stage of the full trigger process. It reduces the rate coming from the HLT1 trigger of 50 kHz to a rate of 12.5 kHz that can then be written to tape. The HLT2 trigger performs a full event reconstruction from the full information from every subdetector. The selection is split into different physics lines which are looking for specific decay channels of interest.

Events that pass the trigger system are written to tape and stored. They are then ready to be used and analysed by the physics analyst.

In the LHCb trigger system, it is important to know whether a given signal candidate fired a specific trigger line. This tells us whether the signal candidate is the source of the trigger decision or if some unrelated particle, perhaps produced in an unrelated decay, fired the line. For this a denomination is assigned to the candidate:

- *Trigger On Signal* (`TOS`) shows the signal candidate has fired the positive trigger decision.
- *Trigger Independent of Signal* (`TIS`) shows an unrelated candidate, not part of the signal, fired the trigger line.
- *Trigger On Both* (`TOB`) shows the candidate is neither `TIS` nor `TOS`. Both the signal and an unrelated candidate were required to fire the positive trigger decision.

The LHCb software stack

The LHCb software stack is used to process data from online and offline streams, as well as simulation. The data has to be processed from the raw collision data read out from the detector to the tabular data format, with high level variables, that is used by the physics analyst. Much of the data processing in centralized either on dedicated computing farms or distributed across the GRID.

The LHCb software stack is built on the Gaudi framework [109, 110], infrastructure of application that provides event reconstruction, selection, and detector simulation. A diagram of the data flow in LHCb is shown in Fig. 2.13 and the different applications are described below.

- Moore is used to perform the HLT1 and HLT2 trigger reconstruction and selection.
- Brunel performs full track reconstruction and particle identification to store large data files in the Data Summary Tapes (DSTs) format.

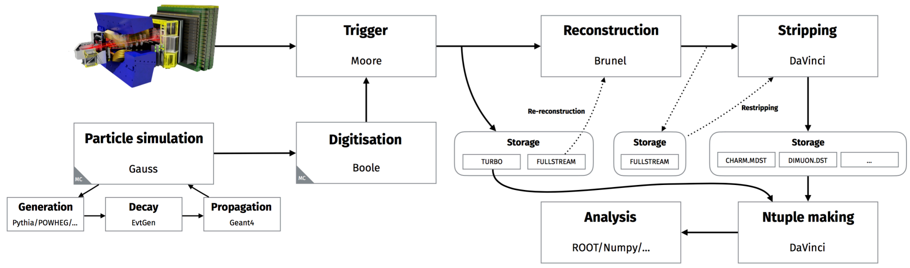

Figure 2.13: *The LHCb data flow through the software stack during Run II [111].*

- DaVinci performs full event reconstruction and provides many tools for calculating important high level variables. The output of DaVinci is Root files [112] which is the typical file format used by a physics analyst.
- Gauss provides the simulation. It simulates pp collision events and the detector response to the events.
- Boole digitizes the detector response as part of the simulation process, allowing for the simulation of the electric response and L0.

Part II

Measurement of y_{CP}

3 Formalism

3.1 Amplitude Structure

Multibody decays are described by an amplitude distribution which when squared gives the probability distribution of the decay. The decay of a particle into a final state is allowed to decay within phase-space of the decay, this is the space in which all allowed states are respresented. For a three body decay, such as the one considered in this thesis, the phase-space can be described using the Dalitz plot. In the Dalitz plot formalism the phase-space can be completely described using two variables, traditionally taken to be the squares of the invariant masses of two of the final state particles. Here we refer to these Dalitz variables as s_0, s_+, and s_-, which correspond to the squares of the invariant masses of the K^+K^-, $K^0_\mathrm{S}K^+$, and $K^0_\mathrm{S}K^-$ respectively.

The distribution of $D^0 \to K^0_\mathrm{S}K^+K^-$ decays in the phase-space of $K^0_\mathrm{S}K^+K^-$ at time $t = 0$ is given by,

$$\langle K^0_\mathrm{S}K^+K^-|D^0(t)\rangle = \mathcal{A}(s_0, s_+)\,, \quad \langle K^0_\mathrm{S}K^+K^-|\overline{D}^0(t)\rangle = \overline{\mathcal{A}}(s_0, s_+)\,. \tag{3.1}$$

Where $\mathcal{A}$ and $\overline{\mathcal{A}}$ are the amplitude distributions of the decay. As time proceeds, mixing introduces a superposition of the decay amplitudes of D^0 and $\overline{D}^0$,

$$\begin{aligned}\langle K^0_\mathrm{S}K^+K^-|D^0(t)\rangle &= \frac{1}{2}\left(\mathcal{A}(s_0, s_+) + \frac{q}{p}\overline{\mathcal{A}}(s_0, s_+)\right) e_1\left(t\right) \\ &+ \frac{1}{2}\left(\mathcal{A}(s_0, s_+) - \frac{q}{p}\overline{\mathcal{A}}(s_0, s_+)\right) e_2\left(t\right),\end{aligned} \tag{3.2}$$

$$\begin{aligned}\langle K^0_\mathrm{S}K^+K^-|\overline{D}^0(t)\rangle &= \frac{1}{2}\left(\overline{\mathcal{A}}(s_0, s_+) - \frac{p}{q}\mathcal{A}(s_0, s_+)\right) e_1\left(t\right) \\ &+ \frac{1}{2}\left(\overline{\mathcal{A}}(s_0, s_+) - \frac{p}{q}\overline{\mathcal{A}}(s_0, s_+)\right) e_2\left(t\right),\end{aligned} \tag{3.3}$$

where

$$e_k\left(t\right) = e^{-i(m_k - i\Gamma_k/2)t} \quad k = 1, 2. \tag{3.4}$$

First lets assume that *CP* is conserved, this implying that $\frac{q}{p} = \frac{p}{q} = 1$. With the current knowledge of *CP* violation in mixing this assumption is reasonable [113]. By writing,

$$\mathcal{A}_1(s_0, s_+) = \left(\mathcal{A}(s_0, s_+) + \overline{\mathcal{A}}(s_0, s_+)\right)/2 \tag{3.5}$$

$$\mathcal{A}_2(s_0, s_+) = \left(\mathcal{A}(s_0, s_+) - \overline{\mathcal{A}}(s_0, s_+)\right)/2 \tag{3.6}$$

then Equations (3.2) and (3.3) can be written as,

$$\langle K^0_S K^+ K^- | D^0(t)\rangle = \mathcal{A}_1(s_0, s_+)\, e_1\,(t) + \mathcal{A}_2(s_0, s_+)\, e_2\,(t)\,, \tag{3.7}$$

$$\langle K^0_S K^+ K^- | \overline{D}^0(t)\rangle = \mathcal{A}_1(s_0, s_+)\, e_1\,(t) - \mathcal{A}_2(s_0, s_+)\, e_2\,(t)\,. \tag{3.8}$$

Conveniently these are also the definition of the *CP* amplitudes,

$$CP\mathcal{A}_1(s_0, s_+) = \mathcal{A}_1(s_0, s_-)\,, \quad CP\mathcal{A}_2(s_0, s_+) = -\mathcal{A}_2(s_0, s_-)\,. \tag{3.9}$$

The isobar model is used to express the amplitude distributions in terms of the amplitudes of the individual intermediate resonances. The three-body decay can proceed via an intermediate resonance, r, resulting in non-constant $|\mathcal{A}|^2$ across the phase-space. In the isoabr model, the overall amplitude $\mathcal{A}$ ($\overline{\mathcal{A}}$) for a D^0 ($\overline{D}^0$) decay to a three-body final state is approximated as a sum of terms with individual couplings and propagators, each respresenting a resonance r in one pair of particles and a constant non-resonant term. Using the isobar model, the amplitude can be written as a sum of intermediate amplitudes,

$$\mathcal{A}(s_0, s_+) = \sum_r a_r e^{i\phi_r} \mathcal{A}_r(s_0, s_+), \tag{3.10}$$

$$\overline{\mathcal{A}}(s_0, s_+) = \sum_r \bar{a}_r e^{i\bar{\phi}_r} \overline{\mathcal{A}}_r(s_0, s_+) = \sum_r a_r e^{i\phi_r} \mathcal{A}_r(s_0, s_-). \tag{3.11}$$

Where in Equation (3.11) it has been assumed *CP* is conserved in strong interaction. The individual amplitudes are themselves *CP*-even or *CP*-odd, satisfying,

$$CP\text{-even}: \quad CP\left[\mathcal{A}_r(s_0, s_+)\right] = \mathcal{A}_r(s_0, s_-)\,, \tag{3.12}$$

$$CP\text{-odd}: \quad CP\left[\mathcal{A}_r(s_0, s_+)\right] = -\mathcal{A}_r(s_0, s_-)\,. \tag{3.13}$$

Thus $\mathcal{A}_1(s_0, s_+)$ is the sum of all the *CP*-even amplitudes and $\mathcal{A}_2(s_0, s_+)$ of the *CP*-odd amplitudes.

3.2 Time evolution

The distribution of events in the $K^0_S K^+ K^-$ phase-space at time t is obtained by squaring the amplitude,

$$\begin{aligned}\left|\langle K^0_S K^+ K^- | D^0(t)\rangle\right|^2 &= |\mathcal{A}_1 e_1(t) + \mathcal{A}_2 e_2(t)|^2 \\ &= \left(\mathcal{A}_1 e_1(t) + \mathcal{A}_2 e_2(t)\right)\left(\mathcal{A}_1^* e_1^*(t) + \mathcal{A}_2^* e_2^*(t)\right) \\ &= |\mathcal{A}_1|^2 |e_1(t)\,|^2 + |\mathcal{A}_2|^2 |e_2(t)\,|^2 + 2\mathcal{R}e\left(\mathcal{A}_1\mathcal{A}_2^* e_1(t)\, e_2^*(t)\right),\end{aligned} \tag{3.14}$$

where $\mathcal{A}_k = \mathcal{A}_k(s_0, s_+)$ for brevity. Following the development of the time dependent terms, we get,

$$\begin{aligned}\left|\langle K_S^0 K^+ K^- | D^0(t)\rangle\right|^2 =& |\mathcal{A}_1|^2 e^{-\frac{t}{\tau}(1+y)} + |\mathcal{A}_2|^2 e^{-\frac{t}{\tau}(1-y)} \\ &+2\mathcal{R}e\left(\mathcal{A}_1\mathcal{A}_2^*\right)\mathcal{R}e\left(e_1(t)\, e_2^*(t)\right) \\ &+2\mathcal{I}m\left(\mathcal{A}_1\mathcal{A}_2^*\right)\mathcal{I}m\left(e_1(t)\, e_2^*(t)\right) \\ =& |\mathcal{A}_1|^2 e^{-\frac{t}{\tau}(1+y)} + |\mathcal{A}_2|^2 e^{-\frac{t}{\tau}(1-y)} \\ &+2\mathcal{R}e\left(\mathcal{A}_1\mathcal{A}_2^*\right)\cos\left(x\frac{t}{\tau}\right) e^{-\frac{t}{\tau}} \\ &+2\mathcal{I}m\left(\mathcal{A}_1\mathcal{A}_2^*\right)\sin\left(x\frac{t}{\tau}\right) e^{-\frac{t}{\tau}}.\end{aligned} \tag{3.15}$$

From this, we can integrate over s_+ resulting in the interference terms to cancel, leaving,

$$\frac{dN(s_0, t)}{dt} \propto a_1(s_0)\, e^{-\frac{t}{\tau}(1+y)} + a_2(s_0)\, e^{-\frac{t}{\tau}(1-y)}, \tag{3.16}$$

where $a_k(s_0, t) = \int_{s_+} |\mathcal{A}_k(s_0, s_+)|^2\, ds_+$. Equation (3.16) holds true for both D^0 and $\overline{D}^0$ decays.

3.3 Phasespace distribution

A peculiarity of the $D^0 \to K_S^0 K^+ K^-$ decay is that there is a good separation between the *CP*-odd and *CP*-even components of the amplitude in the $K_S^0 K^+ K^-$ phase-space. Therefore it is possible to isolate specific regions of phase-space and measure the number of events corresponding to the *CP*-odd and *CP*-even amplitudes. This is particularly effective in the s_0 ($m_{K^+K^-}$) invariant mass distribution which is dominated by two amplitudes: a *CP*-odd ϕK_S^0 resonance, and a $K_S^0 K^+ K^-$ *CP*-even, *S*-wave contribution [114–116].

The distribution of events in a region, $\mathcal{R}$, of the s_0 invariant mass distribution with time is given by,

$$\begin{aligned}\frac{dN_{\mathcal{R}}}{dt} &= \int_{\mathcal{R}} \frac{dN(s_0, t)}{dt} ds_0 \\ &= \int_{\mathcal{R}} \left[a_1(s_0)\, e^{-\frac{t}{\tau}(1+y)} + a_2(s_0)\, e^{-\frac{t}{\tau}(1-y)}\right] ds_0 \\ &= \frac{\int_{\mathcal{R}} (a_1(t) + a_2(t))}{\int_{\mathcal{R}} (a_1(t) + a_2(t))}\left[e^{-\frac{t}{\tau}(1+y)} \int_{\mathcal{R}} a_1(t)\, ds_0 + e^{-\frac{t}{\tau}(1-y)} \int_{\mathcal{R}} a_2(t)\, ds_0\right]\end{aligned} \tag{3.17}$$

Now let us define the fraction of the *CP*-odd amplitude of the total amplitude in region $\mathcal{R}$.

$$f_{\mathcal{R}} = \frac{\int_{\mathcal{R}} a_2(t)\, ds_0}{\int_{\mathcal{R}} (a_1(t) + a_2(t))\, ds_0} \tag{3.18}$$

This is a model-dependent observable that has to be calculated from an amplitude model. With this definition of $f_{\mathcal{R}}$, we can now write,

$$\frac{dN_{\mathcal{R}}}{dt} = \int_{\mathcal{R}} (a_1(t) + a_2(t)) \left[f_{\mathcal{R}} e^{-\frac{t}{\tau}(1+y)} + (1 - f_{\mathcal{R}})\, e^{-\frac{t}{\tau}(1-y)} \right] \tag{3.19}$$

As was mentioned before, the s_0 invariant mass of the $D^0 \to K^0_S K^+ K^-$ decay is dominated by a *CP*-odd ϕK^0_S resonance, and a *CP*-even *S*-wave contribution. If we define two regions, one around the ϕ resonance, which we call ON-resonance, and the other off this resonance peak, which we call OFF-resonance. It clearly follows that the ON-resonance region will be dominated by the *CP*-odd amplitude and the OFF-resonance will be dominated by the *CP*-even amplitude. We use these definitions for the region $\mathcal{R}$ in Equations (3.17) to (3.19).

Therefore by taking the ratio of number of $D^0 \to K^0_S K^+ K^-$ decays in the ON- and OFF-resonance regions we obtain,

$$\frac{dN_{\text{ON}}}{dN_{\text{OFF}}} = \frac{f_{\text{ON}} e^{-\frac{t}{\tau}(1+y)} + (1 - f_{\text{ON}})\, e^{-\frac{t}{\tau}(1-y)}}{f_{\text{OFF}} e^{-\frac{t}{\tau}(1+y)} + (1 - f_{\text{OFF}})\, e^{-\frac{t}{\tau}(1-y)}} \tag{3.20}$$

By performing a Taylor expansion and truncating at order y (as we know y to be small), we then arrive at,

$$\frac{dN_{\text{ON}}}{dN_{\text{OFF}}} \simeq 1 - 2\,(f_{\text{ON}} - f_{\text{OFF}})\,\frac{t}{\tau} y + \mathcal{O}(y^2)\,. \tag{3.21}$$

What has been shown in Equation (3.21) is that by counting the number of decays in the ON- and OFF-resonance regions over decay time, taking the ratio of decays in the regions as a function of decay time, and not assuming *CP* invariance (in which $y = y_{CP}$) we can measure y_{CP}. The result is slightly model dependent as the $f_{\text{ON,OFF}}$ parameters have to be calculated from a model.

We define precisely the regions as:

$$\text{ON-resonance:} \quad m_{K^+K^-} \in [1015, 1025]\ \text{MeV}/c^2 \tag{3.22}$$

$$\text{OFF-resonance:} \quad m_{K^+K^-} \in [2m_K, 1010] \cup [1033, 1100]\ \text{MeV}/c^2. \tag{3.23}$$

3.4 Determination of f_{ON} and f_{OFF}

As shown in Section 3.3, the measurement of y_{CP} is slightly model dependent. It requires the determination of f_{ON} and f_{OFF} which is calculated from a amplitude model. Again, the definition of $f_{\mathcal{R}}$ is the ratio of the *CP*-odd amplitude to the total amplitude,

$$f_{\mathcal{R}} = \frac{\int_{\mathcal{R}} a_2(t)\, ds_0}{\int_{\mathcal{R}} (a_1(t) + a_2(t))}. \tag{3.24}$$

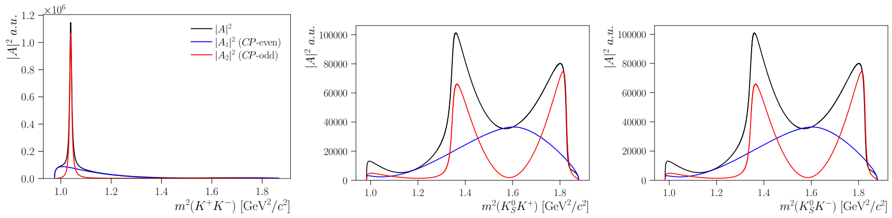

Figure 3.1: *The amplitude model for the $D^0 \to K^0_S K^+ K^-$ decay as reported by the BaBAr collaboration in 2010 [115]. Showing the full amplitude (black), as well as the CP-odd (red) and CP-even (blue) amplitudes.*

Resonance	Mass [MeV]	Width [MeV]	|Amplitude|	Phase (deg.)
$a_0(980)^0$	999	$g_{\eta\pi} = 324$ $g_{K\overline{K}} = 550 \pm 10$	1.0	0.0
$\phi(1020)$	1019.43 ± 0.02	4.59319 ± 0.00004	0.227 ± 0.005	-56.2 ± 1.0
$f_2(1270)$	1275.1	184.2	0.261 ± 0.020	-9 ± 6
$f_0(1370)$	1434	173	0.04 ± 0.06	-2 ± 80
$a_0(1450)$	1474	265	0.65 ± 0.09	-95 ± 10
$a_0(980)^+$	$m_{a^0(980)^0}$	$g_{\eta\pi}, g_{K\overline{K}}$	0.562 ± 0.015	179 ± 3
$a_0(1450)^+$	$m_{a^0(1450)^0}$	$\Gamma_{a^0(1450)^0}$	0.84 ± 0.04	97 ± 4
$a_0(980)^-$	$m_{a^0(980)^0}$	$g_{\eta\pi}, g_{K\overline{K}}$	0.118 ± 0.015	1138 ± 7

Table 3.1: *Amplitudes (a_r), phases ϕ_r, masses, and widths of the resonances in the BaBar 2010 amplitude model [115].*

We consider the model published by the BaBar collaboration in 2010 [115]. This model follows the isobar model and is constructed from 8 resonances: 1 *CP*-odd and 7 *CP*-even, with no non-resonant contribution.

This model is built using a custom written C++ package and then $f_{\mathrm{ON,OFF}}$ is calculated by numerically integrating the *CP*-odd amplitude (the ϕK^0_S resonance) and the *CP*-even amplitude (all the other resonances) over the respective phase-space regions. The resulting value for $f_{\mathrm{ON}} - f_{\mathrm{OFF}}$ is,

$$f_{\mathrm{ON}} - f_{\mathrm{OFF}} = -0.753 \pm 0.004. \tag{3.25}$$

The calculation of the systematic uncertainty on the value of $f_{\mathrm{ON}} - f_{\mathrm{OFF}}$ is discussed in Section 6.3. In the BaBar analysis the model accounts for detector effects and experimentally induced non-uniformaties and is meant to respresent the underyling amplitdue model. The model is published with associated undertainties to account for these effects. In this analysis we take the model as given and account for detector effects and other experimentally induced non-uniformaties in other uncertainties.

3.5 Analysis Strategy

The overall analysis strategy for the measurement of y_{CP} in $D^0 \to K^0_S K^+ K^-$ decays, presented in this thesis, is as follows. A sample of $D^0 \to K^0_S K^+ K^-$ decays is collected as presented in Chapter 4. The data is then split into 15 decay time bins constructed to be approximately evenly populated with candidates. Within each decay time bin a simultaneous maximum likelihood fit, to either the D^{*+} or D^0 mass, is performed between the ON- and OFF-resonance region and the ratio of the two yields is extracted. This then builds up a distribution of $dN_{\mathrm{ON}}/dN_{\mathrm{OFF}}$ over decay time. The distribution is then fitted with the function,

$$\frac{dN_{\mathrm{ON}}}{dN_{\mathrm{OFF}}} = \delta\epsilon \left(1 - 2\left(f_{\mathrm{ON}} - f_{\mathrm{OFF}}\right) \frac{t}{\tau_{D^0}} y_{CP}\right). \tag{3.26}$$

The term $\delta\epsilon$ accounts for any differences in acceptance efficiencies between the ON- and OFF-resonance regions (as long as these efficiencies are integrated over decay time). This analysis strategy has some powerful advantages, notably in the cancelling out of many systematic asymmetries between the ON- and OFF-resonance regions. Further this approach negates the need for flavour tagging of the D^0 meson at production, which in other analyses has been a significant source of systematic uncertainty.

4 Selection and Reconstruction

In this chapter we look at the how $D^0 \to K^0_S K^+ K^-$ candidates were selected. The measurement performed in this thesis uses data collected by LHCb during the years $2016-2018$, corresponding to an integrated luminosity of $5.7\,\mathrm{fb}^{-1}$. A second decay channel was also considered, $D_s^+ \to K^+ K^- \pi^+$, which is used as a control channel to validate the analysis technique and estimate systematic uncertainties. Data from the control channel was also collected during the years $2016-2018$, corresponding to an integrated luminosity of $5.7\,\mathrm{fb}^{-1}$.

4.1 Production

The pp collisions that occur within the LHCb detector produce $D^0 \to K^0_S K^+ K^-$ decays through a number of mechanisms. We broadly classify these production mechanisms into two distinct categories: prompt, and semi-leptonic production. Prompt production occurs when a D^{*+} is produced at the primary vertex, this in turn decays into a D^0 and a π^+. The D^0 produced then decays into the $K^0_S K^+ K^-$ channel of interest. The total decay chain is then, $D^{*+} \to \left[D^0 \to \left[K^0_S \to \pi^+\pi^-\right] K^+ K^-\right] \pi^+$. In a flavour tagged analysis we would determine the neutral D as a D^0 or a $\overline{D}^0$ from the charge of the pion (sometimes referred to as the soft pion) coming from the D^{*+} [1]. However a benefit of the analysis presented in this thesis is that is unnecessary to know the flavour of the D^0 at production, so this detail in unimportant in this analysis.

The second of the production mechanisms is semi-leptonic production, in this mechanism a B meson is produced at the primary vertex. Here we further distinguish between two different semi-leptonic production mechanisms: single, and double tagged. The tagging terminology again refers to using the charge of other particles in the decay chain to determine the flavour of the D^0 at production time. In the single tagged production mechanism a B^+ meson produced at the primary vertex decays directly into a $\overline{D}^0$ meson, a μ^+, and a μ neutrino. The charge of the μ can be used to determine the flavour of the D^0 at production, $B^+ \to \left[\overline{D}^0 \to \left[K^0_S \to \pi^+\pi^-\right] K^+ K^-\right] \mu^+ \nu$. In the double

[1] Unless explicitly stated, charge conjugation is implied throughout.

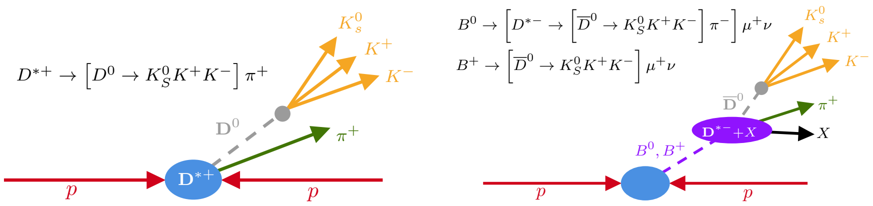

Figure 4.1: *Schematic diagrams of the production mechanisms for $D^0 \to K^0_S K^+ K^-$ decays. Prompt production (left) and semi-leptonic production (right).*

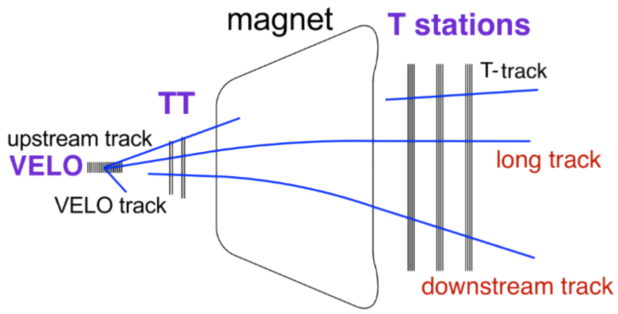

Figure 4.2: *Schematic diagram of the track types in the LHCb tracking system.*

tagged production mechanism, a B^0 is produced at the primary vertex, this then decays into a D^{*-}, μ^+, and ν. The D^{*-} decays into $\overline{D}^0$ and π^- mesons. Now the flavour of the D^0 can be determined from both the charge of the μ^+ and the π^-, hence it being labelled double tagged. The full decay chain is then, $B^+ \to \left[D^{*-} \to \left[\overline{D}^0 \to \left[K^0_S \to \pi^+\pi^-\right] K^+K^-\right] \pi^-\right] \mu^+\nu$.

We further split the data into two categories depending on where the K^0_S decayed. If the K^0_S decayed inside the VELO, then the two π pass through all the tracking systems, they are refered to as long tracks. Alternatively if the K^0_S decays outside the VELO but the π pass through all the tracking stages, these tracks are refered to as downstream tracks. Every sample is then split into LL (long-long) and DD (downstream-downstream) subsamples.

4.2 Monte Carlo simulation

We use a Monte Carlo (MC) simulation sample [117], which undergoes the same trigger lines and offline selection as data. Broadly MC simulation undergoes two stages: genration using Pythia [118], and EvtGen [119]; and simulation using Geant4 [120, 121].

We produce MC using the same production methods as we study in data: Prompt decays, where a D^{*+} originates from the primary vertex, $D^{*+} \to \left[D^0 \to K^0_S K^+ K^-\right] \pi^+$; and secondary decays from a B meson,

$B^+ \to \left[\overline{D}^0 \to K^0_S K^+ K^-\right] \mu^+ \nu$ and $B^0 \to \left[D^{*-} \to \left[\overline{D}^0 \to K^0_S K^+ K^-\right] \pi^-\right] \mu^+ \nu$. We also construct a "mis-reconstructed" secondary decays MC sample where secondary decays that pass the prompt trigger lines are reconstructed as prompt decays.

Two distinct samples of MC were produced for this analysis, first a sample where the MC was generated with a phase-space only distribution, and a second where the MC was generated with a simple amplitude model to ensure a sufficient number of events in the $\phi\,(1020)$ resonance region. In each case, the production steps and reconstruction was identical and the samples are then combined.

We use a truth matching procedure in the MC. This is possi because the MC sample includes truth level information about the generated event, including the type of particle (encoded via the 'PID' variable). This truth level information is then required to correspond to the expected signal particles. For prompt production decays we require: The D^{*+}, D^0 and the soft π PID to be correctly reconstructed; The D^0 to not be a background candidate; The PID of the D^0 mother to match that of the D^{*+}; and the PID of the D^0 mother and soft π mother to be the same.

For secondary decays we require: The B, D^0, and μ PID to be correctly reconstructed; The D^0 to not be a background candidate; for single tagged decays, the PID of the D^0 mother and μ mother to be the same; and for double tagged decays the PID of the D^0 grandmother and μ mother to be the same.

4.3 Trigger Requirements

As was shown in Section 2.2 the LHCb trigger consists of three stages: Level 0 hardware trigger (L0), High Level Trigger 1 (HLT1), and High Level Trigger 2 (HLT2). For the prompt production and the semi-leptonic production we have different trigger requirements at each stage. Here we now introduce a further distinction of data within the prompt sample that arises from different trigger requirements. We split the prompt production sample into a prompt sample, and a Lifetime Unbiased (LTUNB) sample. The LTUNB sample has a different trigger requirement that was designed to reduce the bias in the lifetime measurement of the D^0 meson. We now have eight distinct samples, which are listed below for completeness:

- Prompt LL
- Prompt DD

- LTUNB LL
- LTUNB DD
- SL Single Tagged LL
- SL Single Tagged DD
- SL Double Tagged LL
- SL Double Tagged DD

Here SL refers to semi-leptonic production, and LL and DD refer to the K^0_S decaying inside the VELO and outside the VELO respectively. Each sample is statistically independent, and as such any overlap of candidates between the samples is removed. The procedure for the overlap removal is described in Section 4.5.

For all the prompt production samples we make the requirement that the event has to meet the hardware trigger (L0) requirements either independently of the D^{*+} decay products, `Dst_L0Global_TIS`, or because the decay products of the D^0 candidate meet the hadron-trigger requirements, `D0_L0HadronDecision_TOS`. Here `TIS` and `TOS` refer to Trigger independent of Signal and Trigger on Signal respectively. A candidate is considered to be `TOS` with respect to a trigger selection if it was accepted by that trigger selection. More precisely, if the LHCbIDs [2] of each of the final state particles of the candidate accepted by the trigger selection overlap for more than 70% with the LHCbIDs of final state particles of the offline particles. For semi-leptonic candidates we require that the event passes the `mu_L0MuonDecision_TOS` line, meaning that the μ meets the hardware trigger requirements.

Moving to the next stage of the trigger we distinguish for the first time between the prompt and LTUNB samples. For the prompt samples we require that the candidates meet the requirements of either the one-track `D0_Hlt1TrackMVADecision_TOS`, or two-track `D0_Hlt1TwoTrackMVADecision_TOS` HLT1 trigger. For the LTUNB sample, we make no explicit HLT1 requirement at the HLT1 level. This is to ensure we maintain the lifetime unbiased nature of the sample as it has been shown the HLT1 one-track and two-track MVA lines bias the lifetime of the D^0 in non-trivial ways. For the SL samples we require the candidates meet the requirements of either the one-track, `mu_Hlt1TrackMuonDecision_TOS`, or one-track MVA, `mu_Hlt1TrackMuonMVADecision_TOS`, HLT1 trigger.

[2] Every single LHCb sub-detector element has an LHCbID which is unique across the whole detector. Physics objects, such as tracks, can be defined as sets of LHCbID objects.

For the final stage of the trigger we have the HLT2 requirements. A full reconstruction is done at the HLT2 level, meaning that downstream tracks (which are not reconstructed at the HLT1 level) are also reconstructed, hence we now distinguish between the LL and DD samples. For the prompt sample we require the candidates meet the requirements of the `Hlt2CharmHadDstp2D0Pip_D02KS0KmKp_KS0{LL,DD}Turbo` HLT2 lines, and `Hlt2CharmHadDstp2D0Pip_D02KS0KmKp_KS0{LL,DD}_LTUNBTurbo` for the LTUNB samples. The requirements within these lines are given in Table 4.1. For the semi-leptonic samples the candidates are required to meet the criteria of either the two-, three-, or four-body topological lines, `B_Hlt2TopoMu{2,3,4}BodyDecision_TOS` [122,123]. They are further required to pass an offline stripping line and the requirements are given in Table 4.2.

All the selected candidates are processed using `DecayTreeFitter` [124] (DTF) which constrains the mass of the candidate particle to that of the known mass in the PDG [69]. The `DecayTreeFitter` is a kinematic refit of all the final state particle 4-vectors subject to different possible physics contraints. It allows external information, such as the products of a decay must orginate from the same point in space, to be incorporated into the reconstruction to improve the resolution of different variables Multiple fit results with DTF are saved, including: A simple refit, with no contraints on particle masses; the K^0_S mass constrained to its known value (taken from the PDG [69]); and the K^0_S and D^0 mass constrained to known values. For each of these fits the D^{*+} is constrained to have come from the PV. This gives a better mass resolution and improves the ability to distinguish between signal and background in the invariant mass distributions.

4.4 Offline Selection Requirements

A final offline selection is applied to the candidates and is summarised in Tables 4.3 and 4.4. Further track clones can occur in LHCb data. These are defined to be when two tracks share at least 70% of hits in the VELO and 70% of hits in the T-stations seeding region. To remove clones it is required that all tracks have a unique set of hits within an event.

4.5 Overlap Removal

In order to ensure that the samples are statistically independent we have to remove any candidates that are found in more than one sample.

If a candidate is found to be in both the prompt and LTUNB samples it is removed from the prompt sample and left in the LTUNB sample. This is

Particle	Variable	Requirement
D^*	Mass	$\in [-4.57018, 35.42982]$ MeV/c^2
	Vertex-fit χ^2/ndf	< 10
	$m_{D^*} - m_{D^0} - m_\pi$	$\in [-4.57018, 25.42982]$ MeV/c^2
soft $\pi^\pm$	Track χ^2/ndf	< 3.0
	Track-based ghost probability	< 0.25
	Transverse momentum	> 200.0 MeV/c
	Momentum	> 1000.0 MeV/c
D^0	M	$\in [1765.0, 1965.0]$ MeV/c^2
	Mass	$\in [1740.0, 1990.0]$ MeV/c^2
	$\sum p_T$	> 1500.0 MeV/c
	Transverse momentum	> 1800.0 MeV/c
	Vertex-fit χ^2/ndf	< 5.0
	Direction angle	$> \cos(0.0356)$ (Prompt)
		$> \cos(0.1415)$ (LTUNB)
	χ^2 separation from Primary Vertex	> 20.0 (Prompt)
	Proper lifetime	> 0.0001 (Prompt)
		> 0.00025 (LTUNB)
	Daughter vertex distance χ^2	$> e^5$
$K^\pm$	Track χ^2/ndf	< 3.0
	Track-based ghost probability	< 0.4
	Momentum	> 1000.0 MeV/c
	Transverse momentum	> 500.0 MeV/c (LTUNB)
	Minimum IP χ^2	> 4.0 (Prompt)
	PIDK	> 5
K^0_S	Vertex z-position	$\in [-100, 500.0]$ (LL)
		$\in [300, 2275.0]$ (DD)
	Mass	$\in [35, 50]$ MeV/c^2 (LL)
		$\in [64, 80]$ MeV/c^2 (DD)
	Vertex χ^2/ndf	< 30
	Proper lifetime	> 2.0 ps (Prompt)
	z distance from PV	> 400.0 mm (DD)
$\pi^\pm$	Track χ^2/ndf	< 3 (LL)
		< 4 (DD)
	Minimum IP χ^2	> 36 (LL)
	Momentum	> 3000 MeV/c (DD)
	Transverse momentum	> 175 MeV/c (DD)

Table 4.1: *Prompt Hlt2 selection requirements.*

Particle	Variable	Requirement
B	Mass	$\in [2500, 6000]$ MeV/c^2
	Vertex-fit χ^2/ndf	< 6
	Corrected mass	$\in [4000, 6000]$ MeV/c^2
	Momentum	> 10000 MeV/c
	Transverse momentum	> 1700 MeV/c
	Track χ^2/ndf	< 4
	Minimum IP_χ^2 of Primary Vertex	> 16
	Minimum IP of Primary Vertex	> 0.1 mm
	$\cos\theta$ between momentum and flight	> 0.999
K^0_S	Transverse momentum	> 500 MeV/c
	Momentum	> 5000 MeV/c
	Track χ^2/ndf	< 4
	χ^2 separation from Primary Vertex	> 1000
	Mass	$\in [467, 527]$ MeV/c^2
	$\left\lvert m(\pi^+\pi^-) - m^{\mathrm{PDG}}_{K^0_\mathrm{S}} \right\rvert$	< 64 MeV/c^2 (DD)
		35 MeV/c^2 (LL)
	Vertex-fit χ^2/ndf	< 25 (DD)
	χ^2 separation from Primary Vertex	> 4 (LL)
	x vertex χ^2	< 30 (LL)
$\pi^\pm$ of K^0_S	Momentum	> 2000 MeV/c^2 (DD)
	Minimum IP-χ^2 of Primary Vertex	> 4 (DD)
		> 9 (LL)
	π^+, π^- distance of closest-approach χ^2	< 25 (DD)
		< 30 (LL)
$K^\pm$	Track χ^2/ndf	< 4
	Transverse momentum	> 100 MeV/c
	Momentum	> 1000 MeV/c
	Minimum IP-χ^2 of Primary Vertex	> 4
	Track-based ghost probability	< 0.4
	K^+, K^- distance of closest-approach	< 0.5 mm
Soft $\pi^\pm$s	Track χ^2/ndf	< 4
	Transverse momentum	> 100 MeV/c
	Momentum	> 1000 MeV/c
	Minimum IP-χ^2 of Primary Vertex	> 4
	Track-based ghost probability	< 0.4
D^*	D^0, π distance of closest-approach	< 0.5 mm
	$\left\lvert m(D^0\pi) - m^{PDG}_{D^*} \right\rvert$	< 600 MeV/c^2
	Vertex-fit χ^2/ndf	< 10
	χ^2 separation from Primary Vertex	> 36
	$\cos\theta$ between momentum and flight	> 0
D^0	$m\left(D^*\right) - m\left(D^0\right)$	< 200 MeV/c^2
	$\sum p_T$	> 1800 MeV/c
	Mass	$\in [1765, 1965]$ MeV/c^2
	Vertex-fit χ^2/ndf	< 10
	χ^2 separation from Primary Vertex	> 36
	$\cos\theta$ between momentum and flight	> 0
μ	Track χ^2/ndf	< 4
	Transverse momentum	> 100 MeV/c
	Momentum	> 1000 MeV/c
	Minimum IP-χ^2 of Primary Vertex	> 4
	Track-based ghost probability	< 0.4

Table 4.2: *Semi-leptonic stripping line selection requirements.*

Particle	Variable	Requirement
D^{*+}	Mass	$\in [2004.5, 2020]$ MeV/c^2
	Δm $(m_{D^{*+}} - m_{D^0})$	$\in [139.57, 156]$ MeV/c
	Vertex-fit χ^2/ndf	$\in [0, 6]$
D^0	Mass	$\in [1840, 1890]$ MeV/c^2
	Vertex-fit χ^2/ndf	> 0
	Decay-time	$[0.3, 8]\,\tau$
	Impact parameter χ^2	< 9
	|Transverse impact parameter|	$> 80\,\mu$m
	End Vertex χ^2	< 15
	Pseudorapidity	< 4.4
K^0_S	Mass	[485,510] MeV/c^2 (LL)
		[478,520] MeV/c^2 (DD)
	Logarithm of the decay-length χ^2	> 5
	Transverse momentum	> 200 MeV/c
	Vertex-fit χ^2/ndf	$\in [0, 6]$
	Decay time	> 0
$K^{\pm}$	Track-based ghost probability	< 0.5
	ProbNNK	> 0.1
$\pi^{+}{}_{\text{soft}}$	Transverse momentum	> 200 MeV/c
	Impact parameter χ^2	< 25
	Track-based ghost probability	< 0.25
	PIDe	< 4

Table 4.3: *Prompt offline selection requirements.*

to ensure we minimise the bias to the LTUNB sample. A similar procedure is performed between the single and double tagged semi-leptonic samples. Due to mis-reconstruction of double tagged candidates as single tagged candidates, we found a number of candidates in both the single and double tagged semi-leptonic samples. In this case we remove the candidate from the single tagged sample and keep it in the double tagged sample.

It is possible for more than one singal candidate to be reconstructed in a single *pp* interation ('event'). These are referred to as multiple candidates. They treat them we look over all the candidates and check if two or more candidates share the same event number and run number. In the case that we find a set of candidates with the same event number and run number, we randomly choose one to retain and the rest are removed from the sample [125]. This process removes $\mathcal{O}\,(1\%)$ of events.

Once these steps are completed we are satisfied that all samples are statistically independent.

Particle	Variable	Requirement
D^{*+}	Mass	$\in [2004.5, 2020]$ MeV/c^2
	Δm ($m_{D^{*+}} - m_{D^0}$)	$\in [139.57, 156]$ MeV/c
	Vertex-fit χ^2/ndf	$\in [0, 6]$
D^0	Mass	$\in [1840, 1890]$ MeV/c^2
	Vertex-fit χ^2/ndf	> 0
	Decay-time	$[0.3, 8]\,\tau$
	Impact parameter χ^2	< 9
	|Transverse impact parameter|	$> 80\,\mu$m
	End Vertex χ^2	< 15
	Pseudorapidity	< 4.4
K^0_{S}	Mass	[485,510] MeV/c^2 (LL)
		[478,520] MeV/c^2 (DD)
	Logarithm of the decay-length χ^2	> 5
	Transverse momentum	> 200 MeV/c
	Vertex-fit χ^2/ndf	$\in [0, 6]$
	Decay time	> 0
$K^{\pm}$	Track-based ghost probability	< 0.5
	ProbNNK	> 0.1
$\pi^{+}{}_{\mathrm{soft}}$	Transverse momentum	> 200 MeV/c
	Impact parameter χ^2	< 25
	Track-based ghost probability	< 0.25
	PIDe	< 4

Table 4.4: *Semi-leptonic offline selection requirements.*

4.6 Control channel

A sample of $D_s^+ \to K^+K^-\pi^+$ candidates is selected in order to validate the measurement of y_{CP} as well as to study systematic uncertainties. Unlike the $D^0 \to K^0_{\mathrm{S}}K^+K^-$ sample used for the measurement of y_{CP}, the $D_s^+ \to K^+K^-\pi^+$ consists of a single sample of promptly-produced candidates. In order to be able to properly validate the technique used, it is important that the selection is as close to the $D^0 \to K^0_{\mathrm{S}}K^+K^-$ channel as possible. The candidates go through an almost identical procedure of online and offline selection with some differences in the precise selection criteria used at each stage.

The candidates are required to pass the requirements of the L0 trigger either independently of the D_s^+ decay products, `Dplus_L0Global_TIS`, or because the decay products of the D_s^+ candidate meet the hadron-trigger requirements, `Dplus_L0HadronDecision_TOS`. The candidates are then required to pass the requirements of either the one-track `Dplus_Hlt1TrackMVADecision_TOS`, or two-track `Dplus_Hlt1TwoTrackMVADecision_TOS` HLT1 trigger lines. Finally in the online selection the candidates are required to pass the requirements of the `Hlt2CharmHadDspToKmKpPipTurbo` HLT2 line. The online requirements of the HLT2 line are given in Table 4.5.

Particle	Variable	Requirement
D_s^+	Mass	$\in [1889.0, 2049.0]$ MeV/c^2
	$\sum p_T$	> 3000.0 MeV/c
	Transverse momentum	> 1000.0 MeV/c
	Vertex-fit χ^2/ndf	< 6.0
	Direction angle	$> \cos(0.0141)$
	Proper lifetime	> 0.0002
$K^\pm$	Track χ^2/ndf	< 3.0
	Track-based ghost probability	< 0.4
	Momentum	> 1000.0 MeV/c
	Transverse momentum	> 200.0 MeV/c
	Minimum IP χ^2	> 4.0
	PIDK	> 5
π^+	Track χ^2/ndf	< 3.0
	Track-based ghost probability	< 0.4
	Momentum	> 1000.0 MeV/c
	Transverse momentum	> 200.0 MeV/c
	Minimum IP χ^2	> 4.0
	PIDK	< 5

Table 4.5: *Control channel, $D_s^+ \to K^+K^-\pi^+$, Hlt2 selection requirements .*

Particle	Variable	Requirement
D^0	Mass	$\in [1890, 2050]$ MeV/c^2
	Vertex-fit χ^2/ndf	> 0
	Decay-time	$[0.4, 8.5]\,\tau$
	Impact parameter χ^2	< 9
	End Vertex χ^2	< 15
	Pseudorapidity	$\in [2.1, 4.4]$
	Momentum	< 1.8 GeV/c
	Transverse momentum	$\in [0.3, 10]$ GeV/c
$K^\pm$	Track-based ghost probability	< 0.5
	ProbNNK	> 0.1
	$m(K^+K^-)$	< 1070 MeV/c^2
π^+	Track-based ghost probability	< 0.5

Table 4.6: *Control channel, $D_s^+ \to K^+K^-\pi^+$, offline selection requirements.*

Again an offline selection procedure is applied and the criteria is summarised in Table 4.6.

Finally an identical procedure to the one described in Section 4.5 is performed to remove any clones and multiple candidates.

4.7 Resolution

The experimental resolution on the measured decay time is not accounted for in this thesis. The decay time resolution is determined using simulation by studying the difference between the generated and reconstructed decay times of the events. The resolution can have an impact on the analysis by inducing

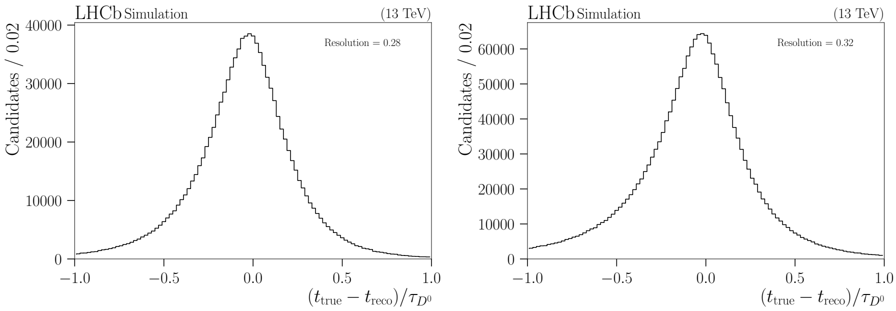

Figure 4.3: *Distribution of the difference between generated and reconstructed decay time, as determined by simulation, for the semi-leptonic single tag samples. Left LL and right DD samples.*

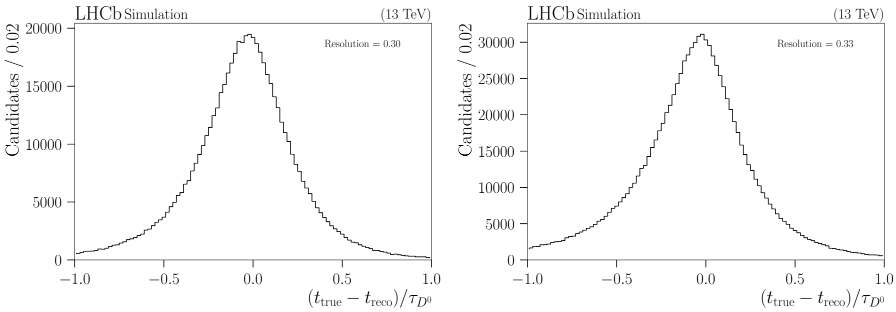

Figure 4.4: *Distribution of the difference between generated and reconstructed decay time, as determined by simulation, for the semi-leptonic double tag samples. Left LL and right DD samples.*

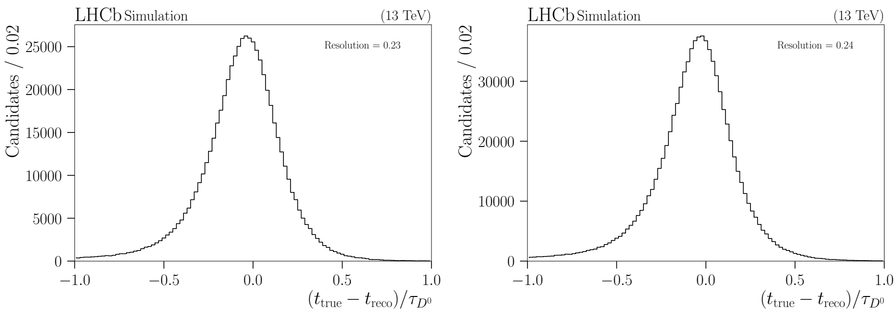

Figure 4.5: *Distribution of the difference between generated and reconstructed decay time, as determined by simulation, for the prompt samples. Left LL and right DD samples.*

a migration of events from one decay time bin to another. However the resolutions found are small in comparison to the width of the decay time bins and thus are not expected to induce any large biases. The difference between the generated and reconstructed decay times is shown in Figs. 4.3 to 4.6, for the semi-leptonic, prompt, and LTUNB samples respectively.

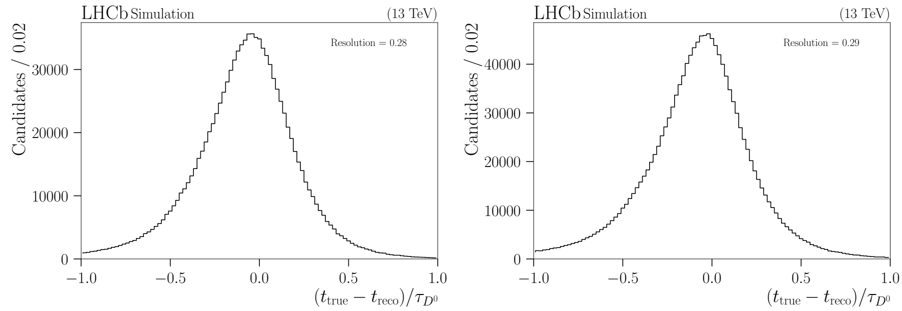

Figure 4.6: *Distribution of the difference between generated and reconstructed decay time, as determined by simulation, for the LTUNB samples. Left LL and right DD samples.*

4.8 Efficiency variation as a function of decay time

The efficiency variation as a function of decay time, or decay time acceptance, is determined through a fit of the reconstructed decay time distribution of the simulated samples. To model the reconstructed decay time distribution, we take an exponential with the known lifetime that is convolved with a resolution function determined from Section 4.7. This is then multiplied with an empircal acceptance function and a Heaveside function, which is given by,

$$\epsilon(t) = \theta(t - t_0)\,\frac{(t - t_0)^n}{1 + [\alpha\,(t - t_0)]^n}\,e^{\beta t}. \tag{4.1}$$

In this the parameters α, β, and n are allowed to float freely and t_0 is taken to be the minimum decay time in the sample being fitted. The fits to the simulated samples and extracted decay time acceptance distributions are shown in Figs. 4.7 to 4.10.

The low efficiency at small decay times is in large part due to displacement requirements on the D^0. The decay time acceptance is expected to be the same across the ON- and OFF-resonance regions, and thus any effects with cancel out in the ratio between the two regions. The acceptance function is used to generate realistic pseudoexperiments but otherwise is not used.

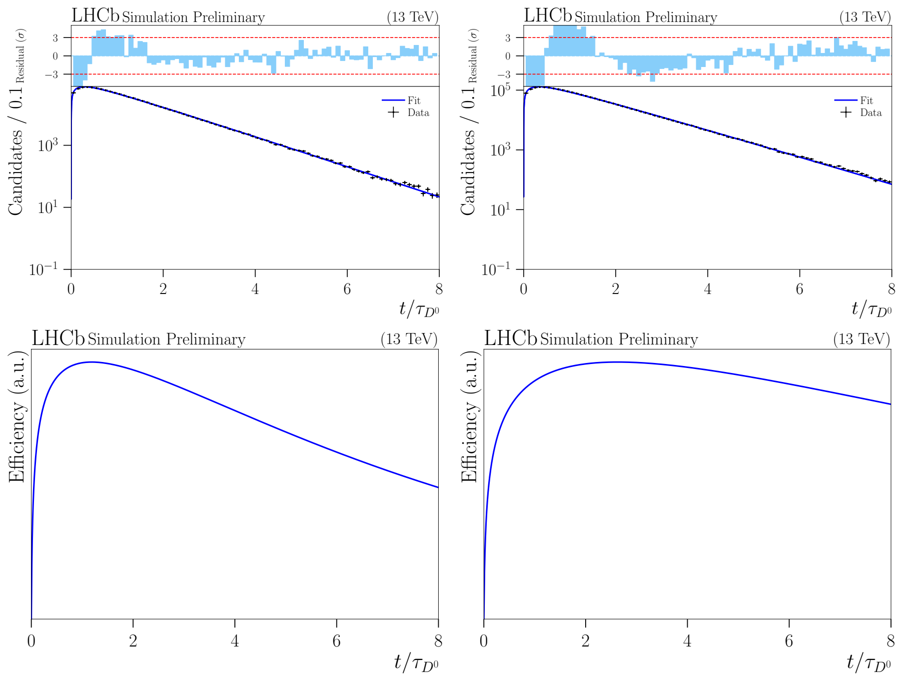

Figure 4.7: *(Top) Fits to the simulated semi-leptonic single tag decay time distributions and (Bottom) the pdf describing the decay time acceptance given in Equation* (4.1). *For the LL (left) and DD (right) samples.*

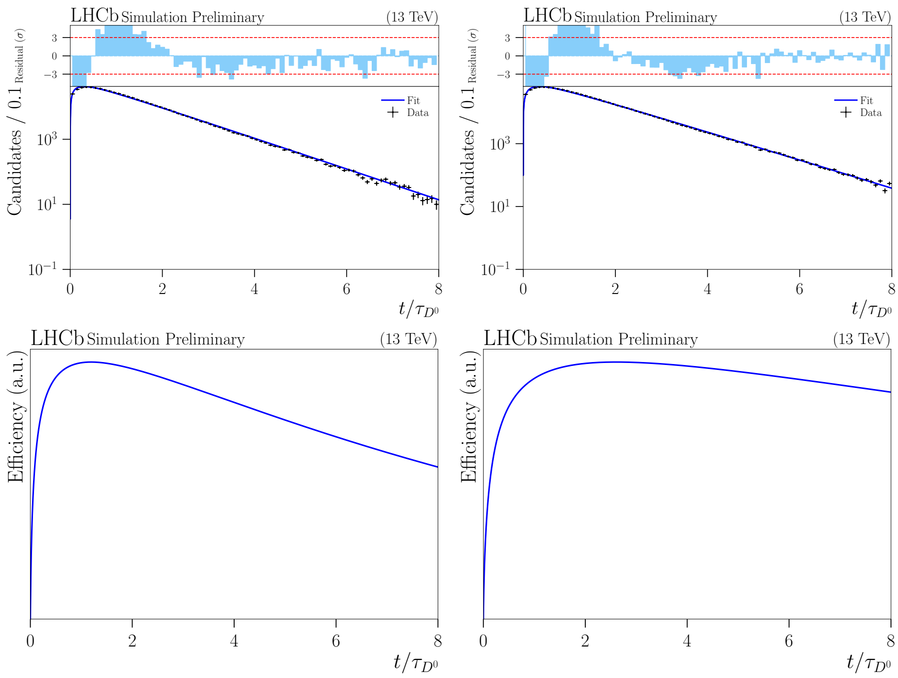

Figure 4.8: *(Top) Fits to the simulated semi-leptonic double tag decay time distributions and (Bottom) the pdf describing the decay time acceptance given in Equation* (4.1)*. For the LL (left) and DD (right) samples.*

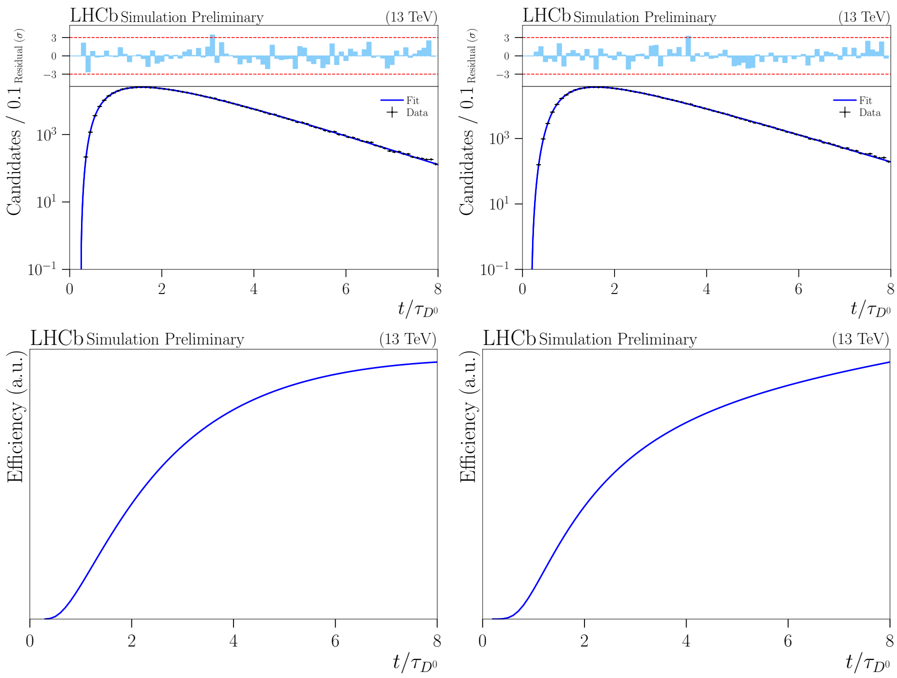

Figure 4.9: *(Top) Fits to the simulated prompt decay time distributions and (Bottom) the pdf describing the decay time acceptance given in Equation* (4.1)*. For the LL (left) and DD (right) samples.*

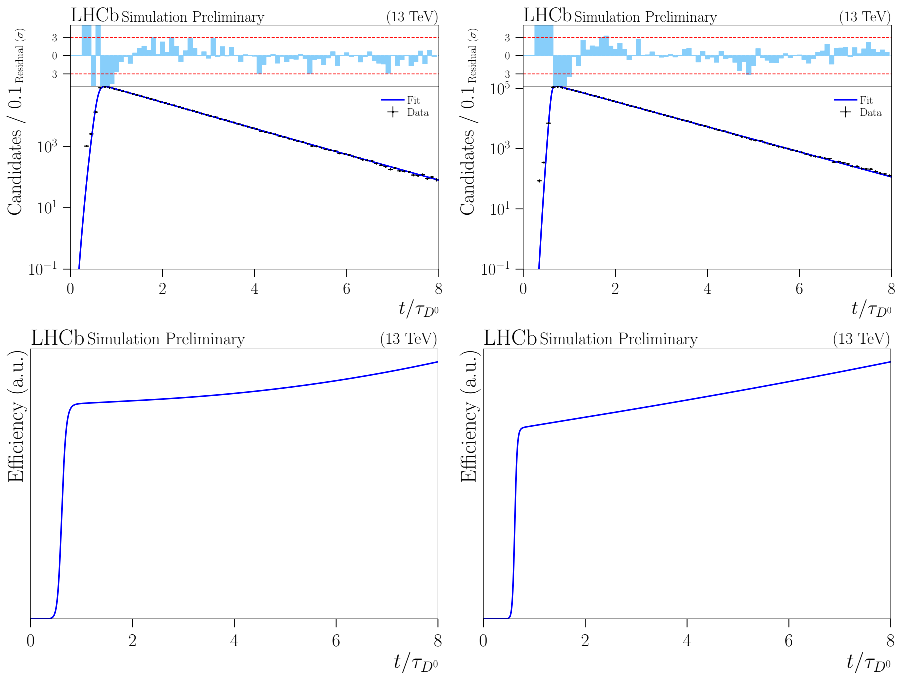

Figure 4.10: *(Top) Fits to the simulated LTUNB decay time distributions and (Bottom) the pdf describing the decay time acceptance given in Equation* (4.1)*. For the LL (left) and DD (right) samples.*

5 Measurement

5.1 Fit Model

In order to separate the signal events from background we perform a fit to the data. For the prompt and LTUNB samples we fit the D^{*+} mass[1] distribution in the range $m\left(D^0\pi^+\right) \in [2004.5, 2020]$ MeV/c^2 and for the semi-leptonic samples we fit the D^0 mass distribution in the range $m\left(K_S^0 K^+ K^-\right) \in [1800, 1930]$ MeV/c^2.

In both cases we model the distribution as the sum of a signal (either the D^{*+} or D^0 signal) and a smooth background dominated by combinatorial background. For the prompt and LTUNB samples, this is due to real D^0 decays being incorrectly combined with a pion that is not associated with the D^0 in a D^{*+} decay, and for SL samples due to random combinations of particles consistent with a D^0 signal.

$$\mathscr{P} = N_{\mathrm{sig}} \mathscr{P}_{\mathrm{sig}}(x) + N_{\mathrm{bkg}} \mathscr{P}_{\mathrm{bkg}}(x)\,, \tag{5.1}$$

where x is $m\left(D^0\pi^+\right)$ for prompt decays and $m\left(K_S^0 K^+ K^-\right)$ for semi-leptonic decays.

For the prompt and LTUNB samples, we model the signal as the sum of a Johnson S_U distribution and two Gaussian functions. The Johnson S_U is defined as [126]:

$$\mathscr{J}\left(x|\mu,\sigma,\delta,\gamma\right) = \frac{1}{\mathscr{N}_J} \frac{e^{-\frac{1}{2}\left[\gamma+\delta\sinh^{-1}\left(\frac{x-\mu}{\sigma}\right)\right]^2}}{\sqrt{1+\left(\frac{x-\mu}{\sigma}\right)^2}}\,, \tag{5.2}$$

where δ and γ are tail parameters.

One of the Gaussian functions shares a mean with the Johnson S_U, while the other is allowed a possible mean shift of $\Delta\mu$. In order to remove correlations, all three shapes share a common width σ, but the two Gaussians are allowed a width scaling factor $s_{1,2}$ respectively. The total signal pdf is then described

[1]Charge conjugation is implied unless otherwise explicitly states.

as:

$$\begin{aligned}\mathscr{P}_{\text{sig}}\left(x|\mu,\sigma,\delta,\gamma,\Delta\mu,s_1,s_2,f_1,f_2\right) = {} & f_1\mathscr{J}\left(x|\mu,\sigma,\delta,\gamma\right)\\ & + \left(1-f_1\right)f_2\mathscr{G}_1\left(x|\mu,s_1\times\sigma\right)\\ & + \left(1-f_1\right)\left(1-f_2\right)\mathscr{G}_2\left(x|\mu+\Delta\mu,s_2\times\sigma\right)\end{aligned} \tag{5.3}$$

The background pdf for both the prompt and LTUNB samples is described using an empirical function based on a two-body phase-space model:

$$\mathscr{P}_{\text{bkg}}\left(x|x_{\text{thr}},\alpha,\beta\right) = \left(x_{\text{thr}}-x\right)^{\alpha}\left[1+e^{\beta\left(x_{\text{thr}}-x\right)}\right], \tag{5.4}$$

where x_{thr} is the threshold set to the known mass of a charged pion, and α and β are floating parameters. Fits to the prompt and LTUNB data samples are shown in Fig. 5.1.

For the semi-leptonic samples we model the signal as the sum of a Johnson S_U distribution and a Birfurcated Gaussian distribution. The Birfurcated Gaussian is defined as:

$$\mathscr{B}\left(x|\mu,\sigma_L,\sigma_R\right) = \begin{cases}\frac{A}{\mathscr{N}_B}e^{-\frac{1}{2}\left(\frac{x-\mu}{\sigma_L}\right)^2} & \text{for } x<\mu,\\ \frac{A}{\mathscr{N}_B}e^{-\frac{1}{2}\left(\frac{x-\mu}{\sigma_R}\right)^2} & \text{for } x\geq\mu,\end{cases} \tag{5.5}$$

where $A = \sqrt{2/\pi}\left(\sigma_L+\sigma_R\right)^{-1}$. The Johnson S_U and Birfurcated Gaussian share a common mean μ but have independent widths. The total signal pdf is then described as:

$$\mathscr{P}_{\text{sig}}\left(x|\mu,\sigma,\delta,\gamma,\sigma_L,\sigma_R\right) = \mathscr{J}\left(x|\mu,\sigma,\delta,\gamma\right) + f_1\mathscr{B}\left(x|\mu,\sigma_L,\sigma_R\right). \tag{5.6}$$

The background pdf for the semi-leptonic samples is described using second order Chebyshev polynomials. Fits to the semi-leptonic samples are shown in Fig. 5.2.

When a fit is performed, it is considered successful if the fit converges, the covariance matrix is well defined, and the estimated distance to the minimum is less that 1.

For the measurement of y_{CP} the fits are performed separately in bins of decay time. In each decay time bin a simultaneous fit is performed between the ON- and OFF-resonance regions, where the signal parameters are shared but the background parameters are allowed to float independently. Fits to the decay time integrated sample are perfomed to get starting values for the parameters in the decay time binned fits, which assists with convergence, but all parameters are still allowed to float independently in each decay time bin.

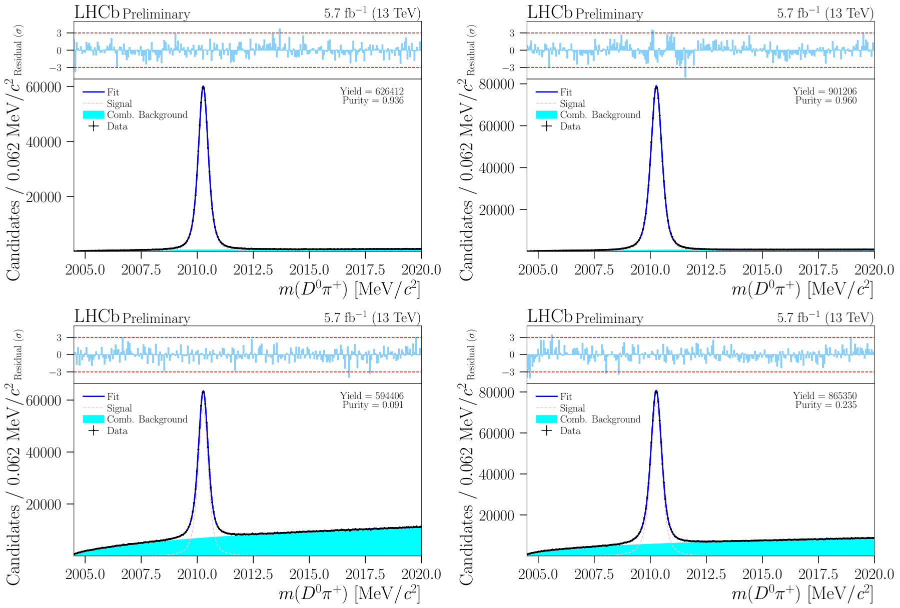

Figure 5.1: *Fits to the D^{*+} mass distribution for the prompt and LTUNB samples. The top plots show the prompt samples, while the bottom plots show the LTUNB samples. The left plots show the LL samples, while the right plots show the DD samples.*

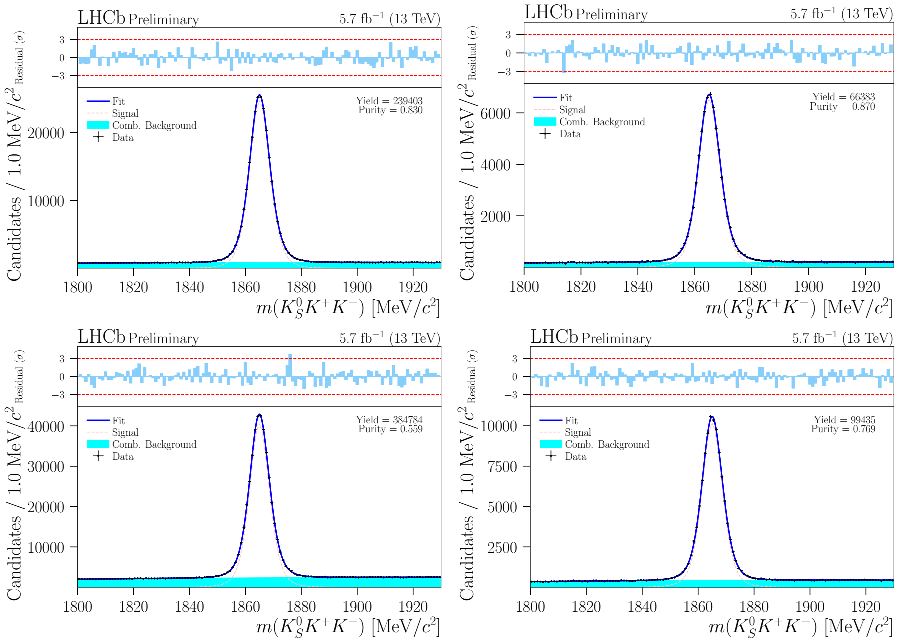

Figure 5.2: *The fit results for the D^0 mass distribution for the semi-leptonic samples. The top plots are for the LL samples, and the bottom for DD samples. The left plots are the single tagged samples, and the right are the double tagged samples.*

5.2 MC Reweighting

It is well known that MC simulation does not perfectly match the data. In order to be able to use our MC to accurately describe and model efficiency effects found in data we need to find a way to improve the agreement between the MC and data. In this analysis we follow a procedure called MC reweighting, in which we weight each event in the MC sample such that the full MC sample better matches the data. Reweighting is the procedure of finding weights for an original distribution, that makes the distribution of one or several variables identical in the original and target distribution. There are a number of different algorithms that can be used for this purpose. In this analysis we utilize the `GBRewighter` algorithm [127].

In this procedure we define the original distribution as the MC sample, and the target distribution as the data. Further we set the initial weights of the MC sample to 1 and the weights of the data are `sWeights` claculated using the `sPlot` technique [128] obtained from the mass fits described in the previous section. We use a folding technique to ensure that the predictions will be unbiased. We use three folds for the reweighter, this means that the data is split randomly into three chunks. The predictions for each chunk will be calculated from the model trained on the other two chunks, and as such the predictions will not be calculated from a model trained on itself.

For all of the samples we use the same input variables in the reweighter: $P\left(D^0\right)$, $P_T\left(D^0\right)$, $\eta\left(D^0\right)$, and $\phi\left(D^0\right)$. Due to differences in conditions between years and polarities, this procedure is performed separately for each year and polarity combination. The results are shown in Figs. 5.3 to 5.10.

We perform a number of sanity checks to ensure that the reweighter is behaving as expected and the predicted weights look acceptable.

5.3 Removal of D^0 decay time-momentum correlations

In this analysis we measure the yields of signal in the ON- and OFF-resonance regions in bins of decay time and fit the ratio of these yields. By taking the ratio of the signal yields we are cancelling out a number of asymmetries such as any time-integrated asymmetries or phase-space integrated asymmetries. These get absorbed into the $\mathcal{R}$ term in the expression Equation (3.26). However, there are still some asymmetries that are not cancelled out. In particular, there are asymmetries that are due to the D^0 decay time-momentum correlations. If we consider an efficiency effect that is both dependent on t and $m_{K^+K^-}$,

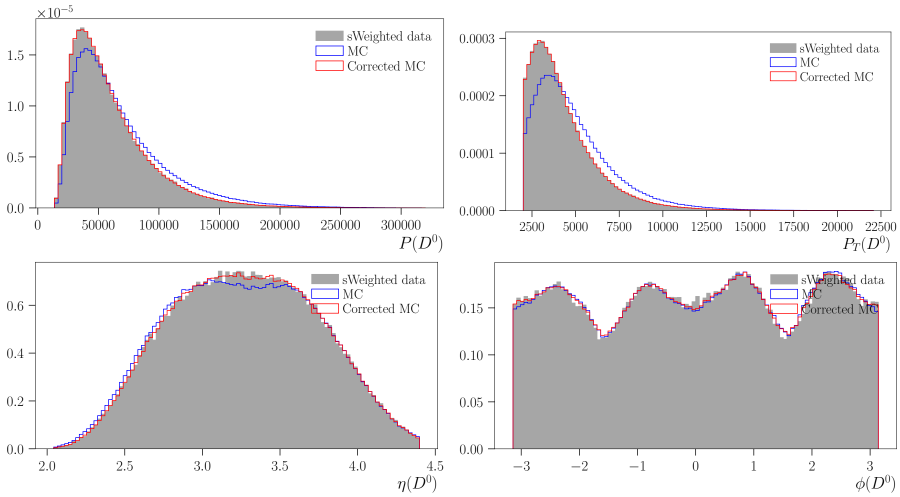

Figure 5.3: *Reweighting of the semi-leptonic LL single tag MC sample to match the background subtracted data for the $P\left(D^0\right)$, $P_T\left(D^0\right)$, $\eta\left(D^0\right)$, and $\phi\left(D^0\right)$ variables. The plots show the background subtracted (`sWeighted`) data, with the MC before and after reweighting, where the weights we calculated using the `GBReweighter` algorithm.*

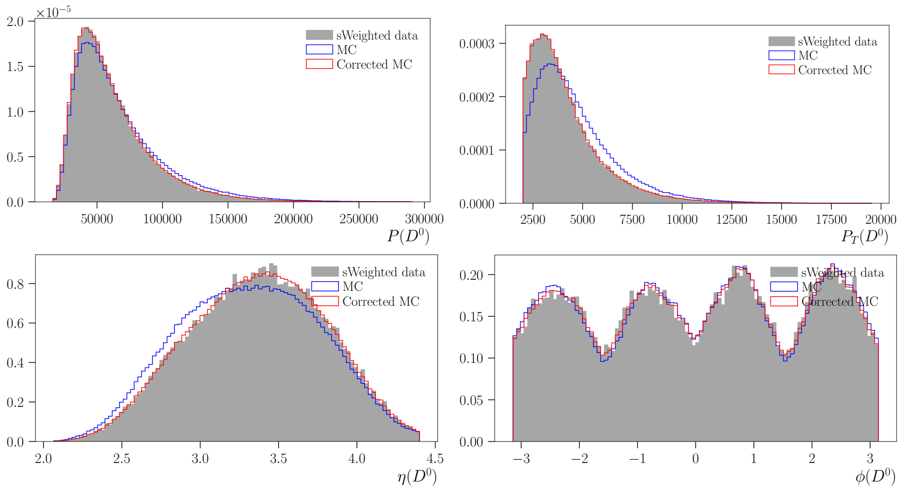

Figure 5.4: *Reweighting of the semi-leptonic LL double tag MC sample to match the background subtracted data for the $P\left(D^0\right)$, $P_T\left(D^0\right)$, $\eta\left(D^0\right)$, and $\phi\left(D^0\right)$ variables. The plots show the background subtracted (`sWeighted`) data, with the MC before and after reweighting, where the weights we calculated using the `GBReweighter` algorithm.*

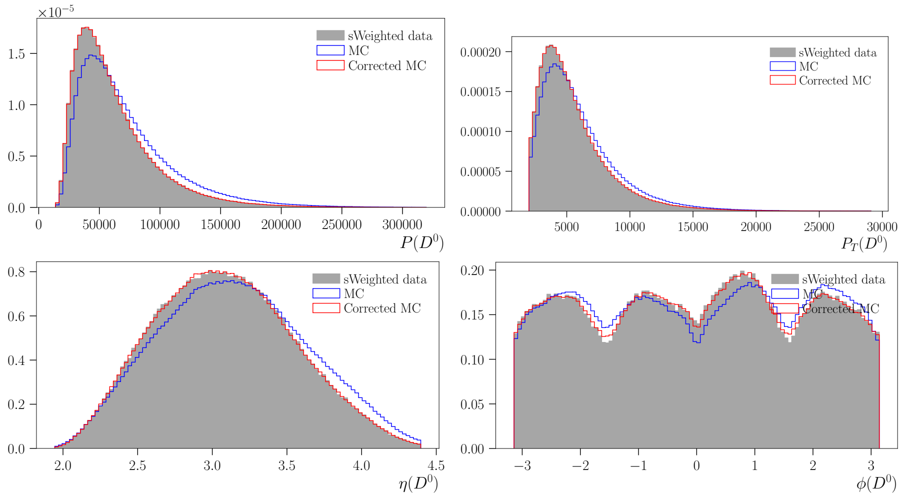

Figure 5.5: *Reweighting of the semi-leptonic DD single tag MC sample to match the background subtracted data for the $P\left(D^0\right)$, $P_T\left(D^0\right)$, $\eta\left(D^0\right)$, and $\phi\left(D^0\right)$ variables. The plots show the background subtracted (`sWeighted`) data, with the MC before and after reweighting, where the weights we calculated using the `GBReweighter` algorithm.*

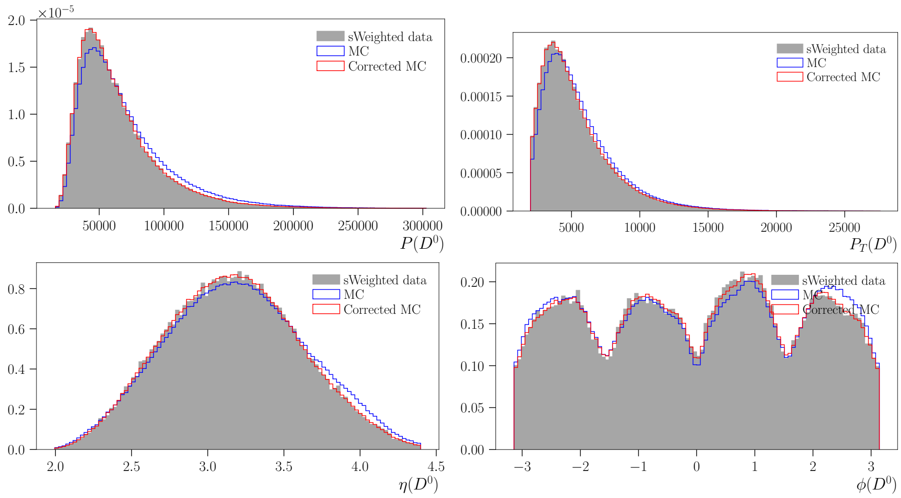

Figure 5.6: *Reweighting of the semi-leptonic DD double tag MC sample to match the background subtracted data for the $P\left(D^0\right)$, $P_T\left(D^0\right)$, $\eta\left(D^0\right)$, and $\phi\left(D^0\right)$ variables. The plots show the background subtracted (`sWeighted`) data, with the MC before and after reweighting, where the weights we calculated using the `GBReweighter` algorithm.*

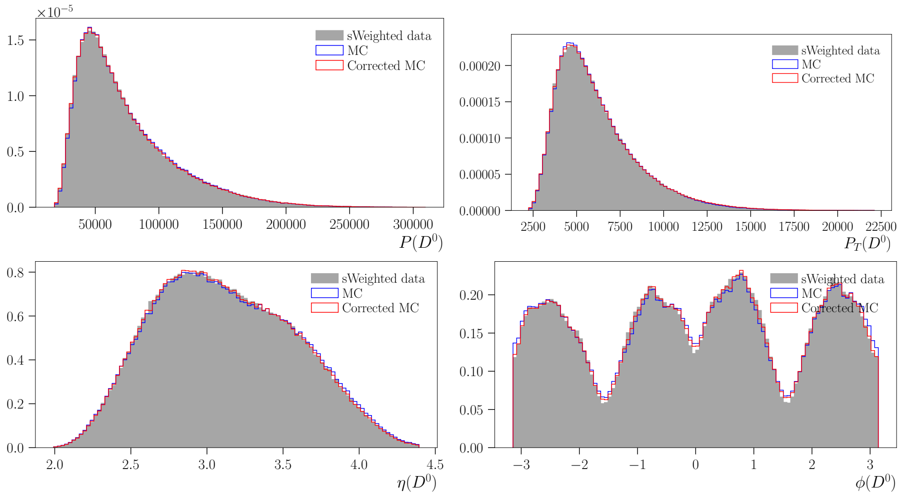

Figure 5.7: *Reweighting of the prompt LL MC sample to match the background subtracted data for the $P\left(D^0\right)$, $P_T\left(D^0\right)$, $\eta\left(D^0\right)$, and $\phi\left(D^0\right)$ variables. The plots show the background subtracted (`sWeighted`) data, with the MC before and after reweighting, where the weights we calculated using the `GBReweighter` algorithm.*

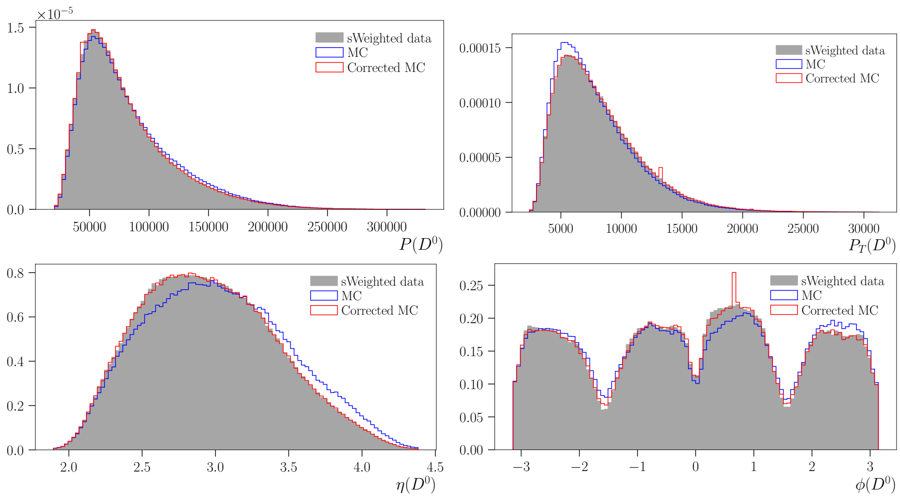

Figure 5.8: *Reweighting of the prompt DD MC sample to match the background subtracted data for the $P\left(D^0\right)$, $P_T\left(D^0\right)$, $\eta\left(D^0\right)$, and $\phi\left(D^0\right)$ variables. The plots show the background subtracted (`sWeighted`) data, with the MC before and after reweighting, where the weights we calculated using the `GBReweighter` algorithm.*

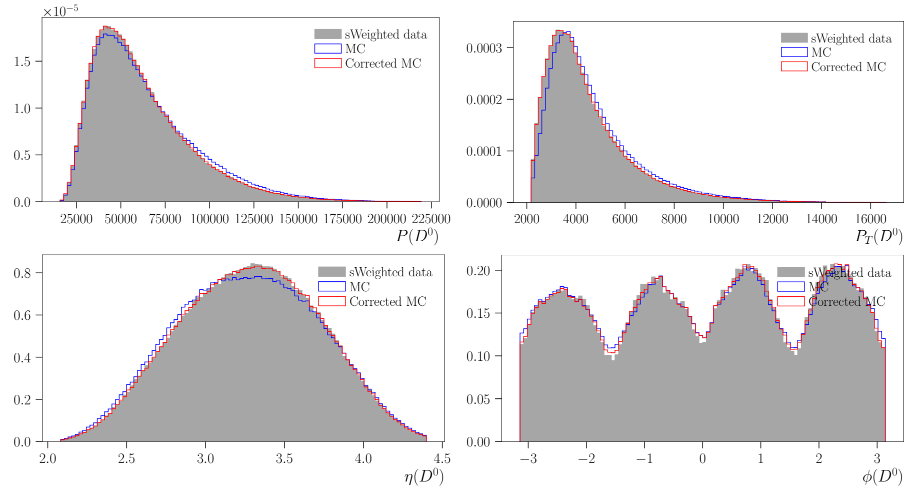

Figure 5.9: *Reweighting of the LTUNB LL MC sample to match the background subtracted data for the $P\left(D^0\right)$, $P_T\left(D^0\right)$, $\eta\left(D^0\right)$, and $\phi\left(D^0\right)$ variables. The plots show the background subtracted (`sWeighted`) data, with the MC before and after reweighting, where the weights we calculated using the `GBReweighter` algorithm.*

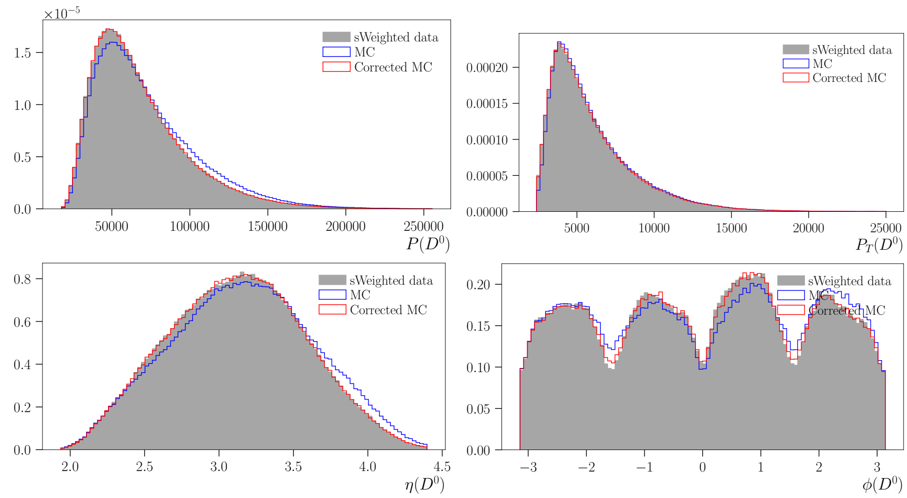

Figure 5.10: *Reweighting of the LTUNB DD MC sample to match the background subtracted data for the $P\left(D^0\right)$, $P_T\left(D^0\right)$, $\eta\left(D^0\right)$, and $\phi\left(D^0\right)$ variables. The plots show the background subtracted (`sWeighted`) data, with the MC before and after reweighting, where the weights we calculated using the `GBReweighter` algorithm.*

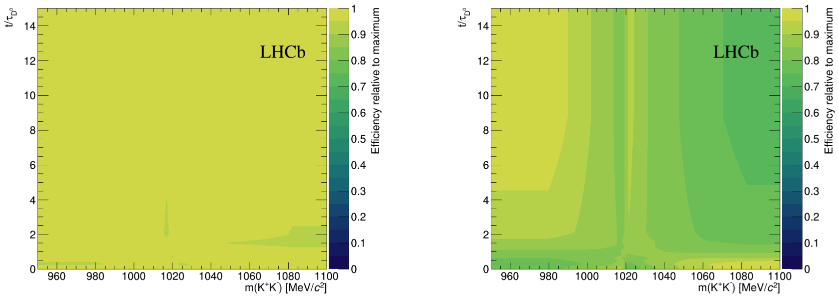

Figure 5.11: *Correlations between t and $m_{K^+K^-}$ for the SL single tagged LL (left) and DD (right) samples.*

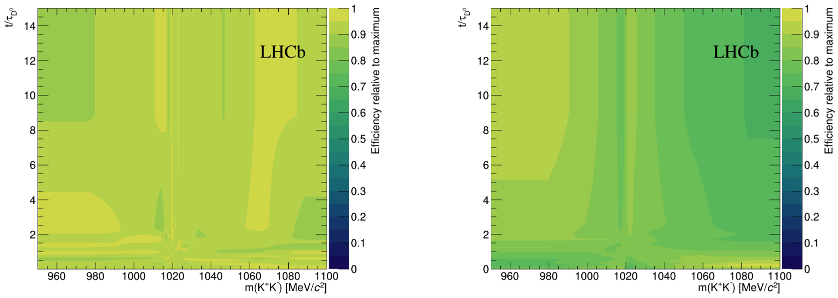

Figure 5.12: *Correlations between t and $m_{K^+K^-}$ for the SL double tagged LL (left) and DD (right) samples.*

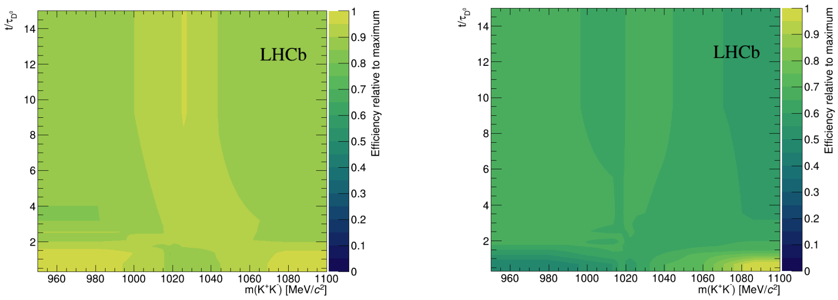

Figure 5.13: *Correlations between t and $m_{K^+K^-}$ for the prompt LL (left) and DD (right) samples.*

$\epsilon\left(t, m_{K^+K^-}\right)$, then we have,

$$\frac{dN_{\mathrm{ON}}}{dN_{\mathrm{OFF}}} \rightarrow \frac{dN_{\mathrm{ON}}\epsilon\left(t, m^{\mathrm{ON}}_{K^+K^-}\right)}{dN_{\mathrm{OFF}}\epsilon\left(t, m^{\mathrm{OFF}}_{K^+K^-}\right)} \tag{5.7}$$

These correlations can be seen in Figs. 5.11 to 5.14

We can either use a data driven technique to obtain the efficiency or by using a simulated sample. Both techniques have their advantages and draw-

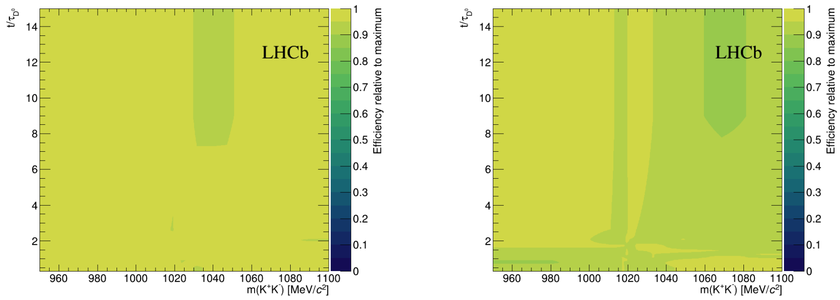

Figure 5.14: *Correlations between t and $m_{K^+K^-}$ for the LTUNB LL (left) and DD (right) samples.*

backs. In the data driven technique you can be confident you have enough statistics to perform the correction. However, we understand these correlations to come from the High Level Trigger, for the prompt sample from the `D0_Hlt1TrackMVA_Line` and `D0_Hlt1twoTrackMVA_Line`, and for the semi-leptonic sample, from the `B_Hlt2TopoMu{2,3,4}Body_Line`. It is then very difficult to distinguish between what correlations in the data are due to the selection requirements and what are due to mixing - the very thing we are trying to measure. There are ways to make this method work, such as in Ref. [68]. The alternative is to use a simulated sample, as is done in Ref. [129]. If the simulated sample is generated without mixing being included then we can be sure that the correlations we see are induced by selection requirements. Conversely we require a large simulated sample in order to have enough statistics to accurately describe the correlations. Further we know that simulation does not perfectly describe the data and considerations need to be made to account for this.

For this analysis a simulated sample is used to obtain the decay time-momentum correlations and perform a correction to the data. The broad steps to perform this correction are as follows:

- Generate a simulated sample of D^0 mesons with no mixing. Use the same amplitude model used to create the signal simulated sample. This sample is referred to as the *generator level* sample, as no reconstruction is performed.

- Add in a decay time acceptance, calculated in Section 4.8 and shown in Figs. 4.7 to 4.10, to the generator level sample.

- Reweight the reconstructed MC sample to the generator level MC sample.

- Use the model trained in the previous step to predict an efficiency for each event in the data.

- Weight each event in data with the inverse of the efficiency predicted in the previous step.

For the first step we generate a sample of D^0 mesons in an identical fashion to the MC described in Section 4.2. Here we use the EvtGen generator [119], that generates the underlying decay that is passed to the LHCb simulation and reconstruction framework. The exact same resonant model is used, but the output is taken directly from the EvtGen generator. We are then left with a generator level sample of D^0 mesons, and by generator level we mean that directly produced from the generator, no interaction with the detector or reconstruction is simulated. For practical reasons, in order to make the reweighter used in the process more efficient, we add a decay time acceptance effect calculated in Section 4.8 to the generator level sample. Critically this sample does not contain any decay time-momentum correlations (that are induced by the detector, and more specifically the HLT1 trigger).

As the generator level sample contains no decay time-momentum correlations, if we were able to find a function that maps the reconstructed MC to the generator level MC, we would then have a function that describes the decay time-momentum correlations. For this we again make use of the `GBReweighter` algorithm. The model is trained to reweight the reconstructed MC to the generator level MC.

Thus we train a `GBReweighter` model reweighting the generated MC to the generator level MC. The model is trained on the following variables:

- The decay time, t.

- The squared invariant masses of the $K^0_S K^+$, $K^0_S K^-$, and K^+K^- pairs, $m^2_{K^0_S K^+}$, $m^2_{K^0_S K^-}$, and $m^2_{K^+K^-}$.

This model reweights any correlation effects we have between variables and the results of the reweighter are shown in Figs. 5.15 to 5.22.

The trained model is then taken an used to predict the weights for the data. The predicted weights are the correlation efficiencies between the decay time and momentum. Each event in data is weighted with the inverse of the predicted correction efficiency. This removes the decay time-momentum correlations from the data, and this weighted dataset is then used in the fits to data.

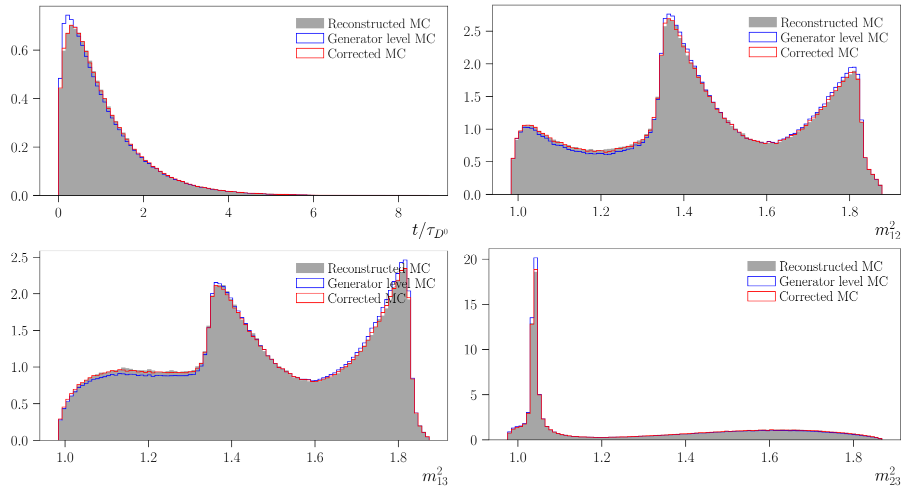

Figure 5.15: *The reweighter trained on the semi-leptonic LL single tag D^0 sample. The top left shows the decay time, and the right column shows the reweighter trained on the squared invariant masses.*

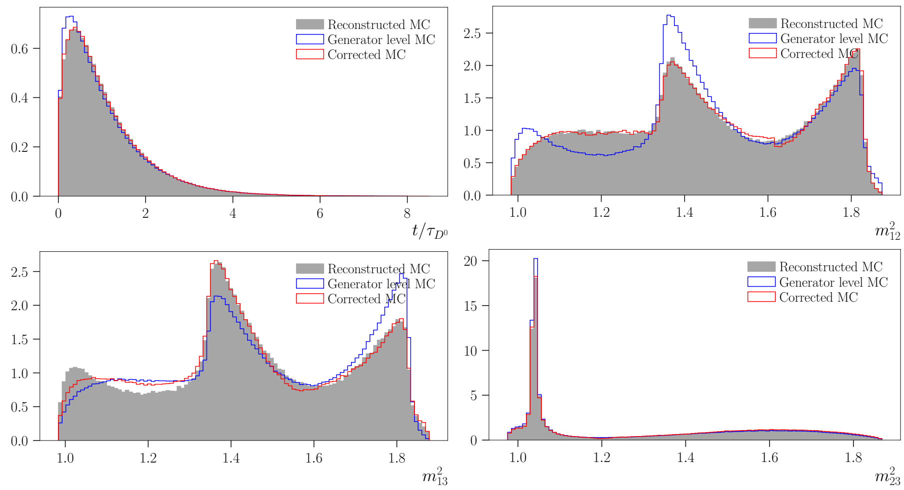

Figure 5.16: *The reweighter trained on the semi-leptonic LL double tag D^0 sample. The top left shows the decay time, and the right column shows the reweighter trained on the squared invariant masses.*

5.4 Calculation of $\langle t \rangle$ and $\langle t^2 \rangle$

When we fit the ratio of the number of events ON- and OFF-resonance, as given in Equation (3.26), we are fitting the ratio of the yields in bins of decay time. Therefore what we are actually fitting is,

$$\langle \frac{dN_{\mathrm{ON}}}{dN_{\mathrm{OFF}}} \rangle_j = \mathcal{R} \left(1 - 2 \left(f_{\mathrm{ON}} - f_{\mathrm{OFF}} \right) \frac{\langle t \rangle_j}{\tau_{D^0}} y_{CP} \right) \tag{5.8}$$

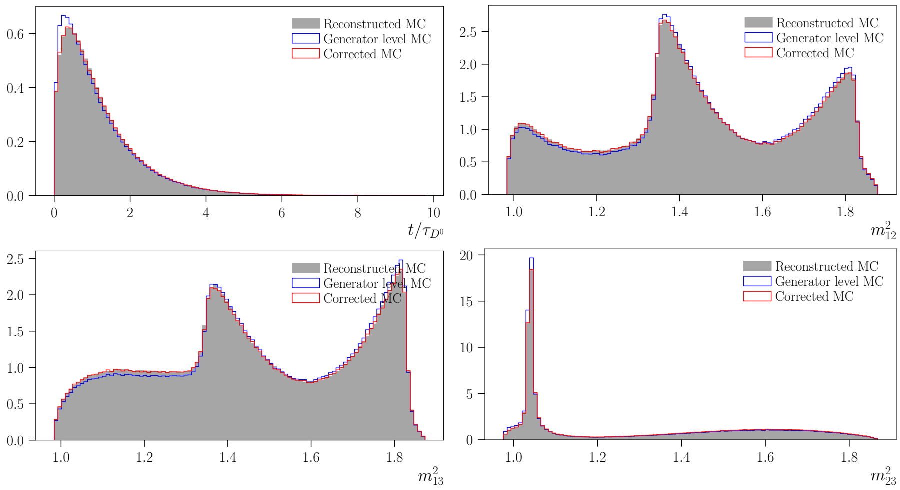

Figure 5.17: *The reweighter trained on the semi-leptonic DD single tag D^0 sample. The top left shows the decay time, and the right column shows the reweighter trained on the squared invariant masses.*

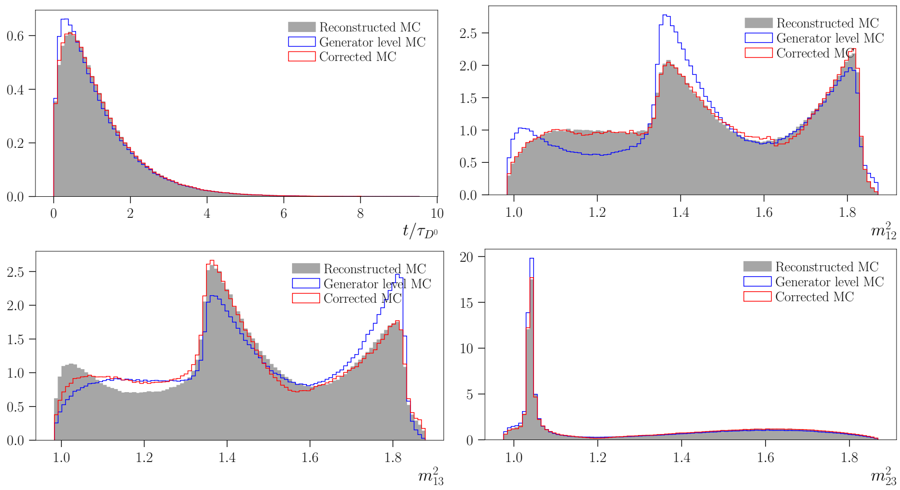

Figure 5.18: *The reweighter trained on the semi-leptonic DD double tag D^0 sample. The top left shows the decay time, and the right column shows the reweighter trained on the squared invariant masses.*

where j is the decay time bin. Therefore it is necessary to know the average values of the decay time, $\langle t \rangle_j$, and the average squared decay time, $\langle t^2 \rangle_j$ (which we take to be the uncertainty of the bin center in each decay time bin), in each bin.

A statistically pure decay-time distribution of D^0 mesons is obtained by subtracting the background using the `sWeights` derived from the mass fits of candidates within each decay, such as shown in Figs. 5.1 and 5.2. The average

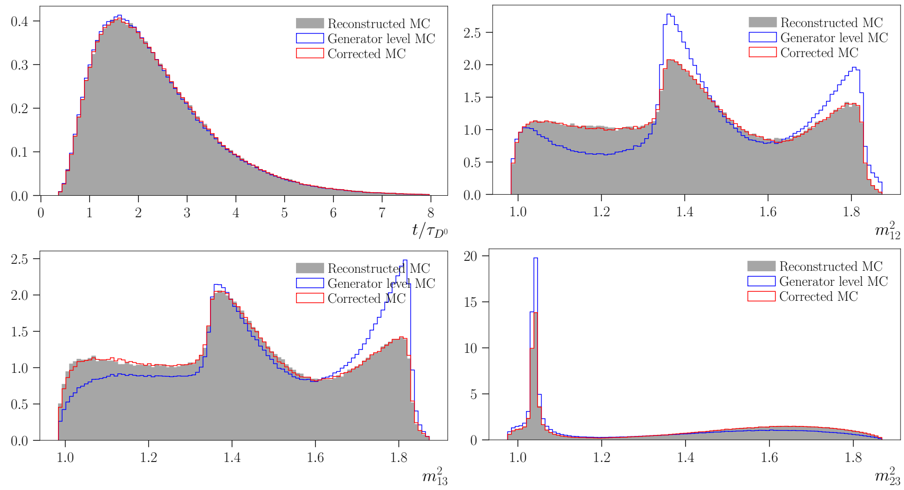

Figure 5.19: *The reweighter trained on the prompt LL D^0 sample. The top left shows the decay time, and the right column shows the reweighter trained on the squared invariant masses.*

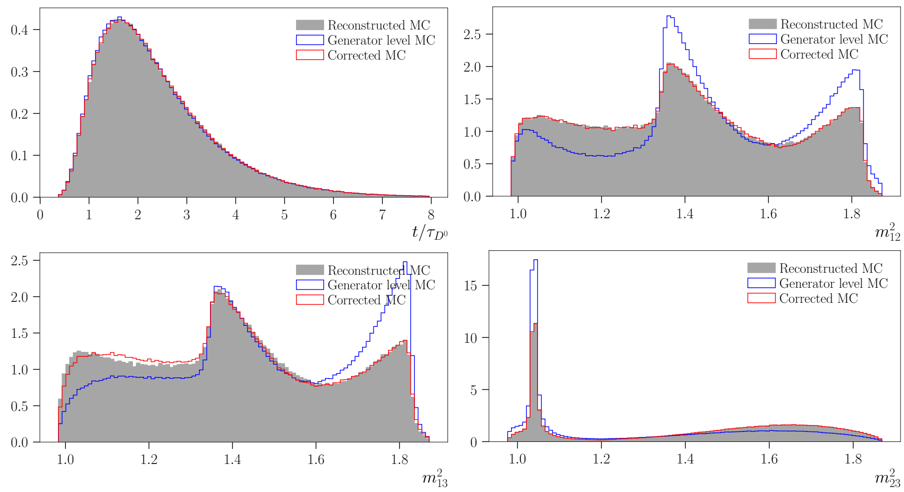

Figure 5.20: *The reweighter trained on the prompt DD D^0 sample. The top left shows the decay time, and the right column shows the reweighter trained on the squared invariant masses.*

decay time and squared decay time are calculated as

$$\langle t \rangle_j = \frac{\sum_i t_i w_i}{\sum_i w_i} \quad \text{and} \quad \langle t^2 \rangle_j = \frac{\sum_i t_i^2 w_i}{\sum_i w_i}, \tag{5.9}$$

where the sum goes over all the candidates populating the decay time bin j and w_i is the weight of the candidate i with decay time t_i. The weight is the product of the `sWeight` and the weight associated with the correction of the decay time-momentum correlations.

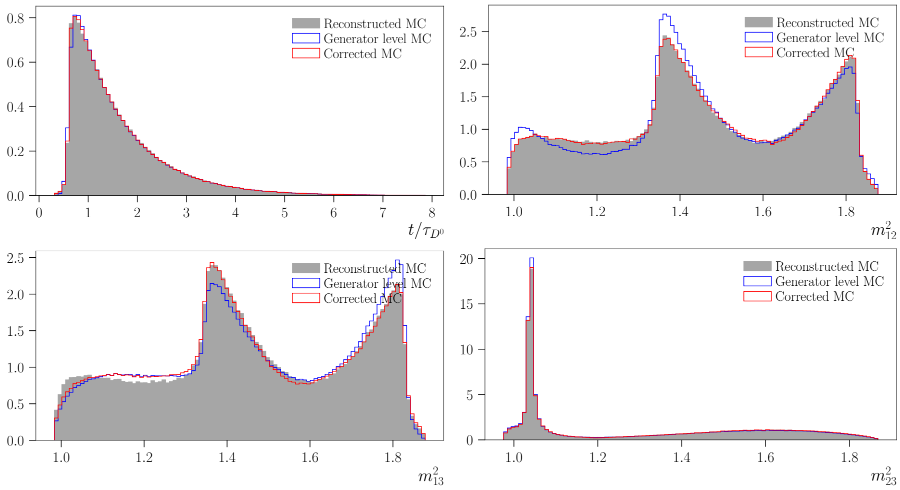

Figure 5.21: *The reweighter trained on the LTUNB LL D^0 sample. The top left shows the decay time, and the right column shows the reweighter trained on the squared invariant masses.*

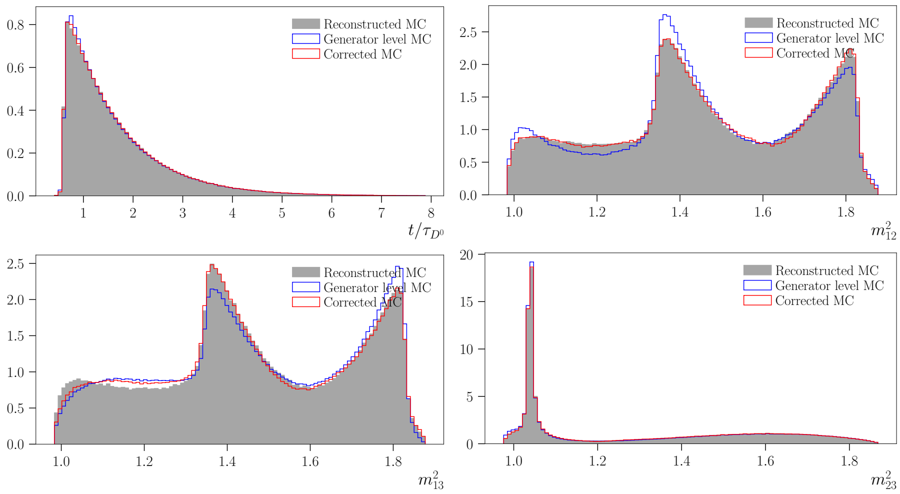

Figure 5.22: *The reweighter trained on the LTUNB DD D^0 sample. The top left shows the decay time, and the right column shows the reweighter trained on the squared invariant masses.*

5.5 Blinding strategy

In keeping with LHCb procedure for an unpublished analysis, the results of this analysis are kept blind. This is done to ensure that the results are not influenced by the physicist performing the analysis and thus to limit any bias.

The blinding strategy consists of both visual and numerical blinding. A random number, $\delta_{y_{CP}}$, between -1.5% and 1.5% is generated (but not known) and used to numerically offset the measured value of y_{CP}, $y_{CP} \to y_{CP} + \delta y_{CP}$.

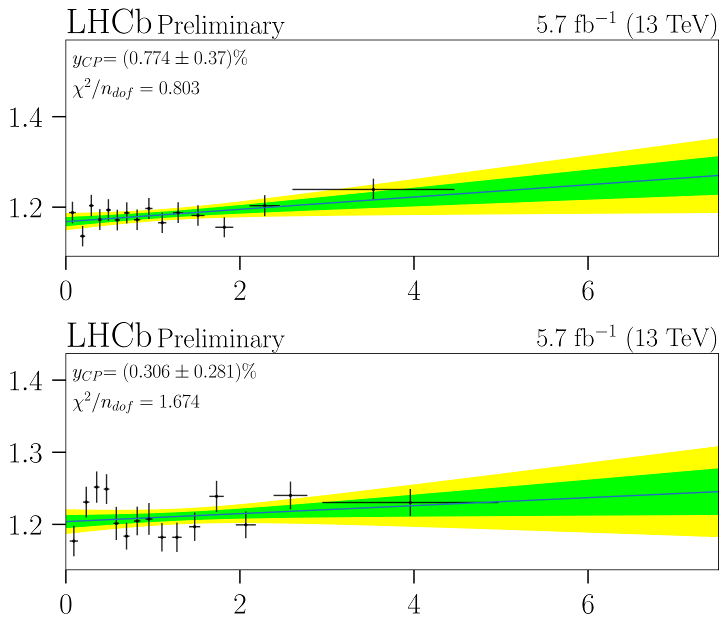

Figure 5.23: *The y_{CP} measurement for the semi-leptonic single tag LL (top) and DD (bottom) samples.*

The range for the random offset is taken to be roughly twice the world average of y_{CP}. Then the data points in the y_{CP} measurement plots Figs. 5.23 to 5.26 are shifted by $-2\,(f_{\mathrm{ON}} - f_{\mathrm{OFF}})\,\frac{t}{\tau_{D^0}}\delta_{y_{CP}}$ thus meaning the fit is to,

$$\frac{dN_{\mathrm{ON}}}{dN_{\mathrm{OFF}}} = 1 - 2\,(f_{\mathrm{ON}} - f_{\mathrm{OFF}})\,\frac{t}{\tau_{D^0}}\,(y_{CP} + \delta_{y_{CP}})\,. \tag{5.10}$$

Therefore the measurement is $y_{CP} + \delta_{y_{CP}}$ and thus is blind.

5.6 Determination of the y_{CP} parameter

Once the analysis procedure has been completed, we have eight statistically independent measurements of the y_{CP} parameter. We fit the function Equation (3.26), to the distributions of $dN_{\mathrm{ON}}/dN_{\mathrm{OFF}}$ for each of the eight samples. The results of the fits are shown in Figs. 5.23 to 5.26. These can then be combined to give a single measurement of y_{CP}. We make the assumption that the measurements are independent and normally distributed and therefore we calculate the weighted average of the measurements [130],

$$x = \frac{\sum_i x_i/\sigma_i^2}{\sum_i 1/\sigma_i^2} \tag{5.11}$$

and the associated uncertainty,

$$\sigma_x = \frac{1}{\sum_i 1/\sigma_i^2}. \tag{5.12}$$

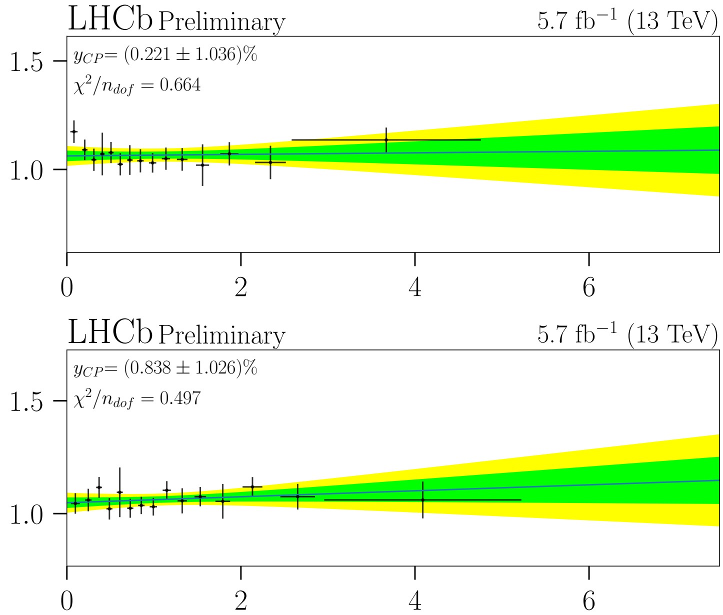

Figure 5.24: *The y_{CP} measurement for the semi-leptonic double tag LL (top) and DD (bottom) samples.*

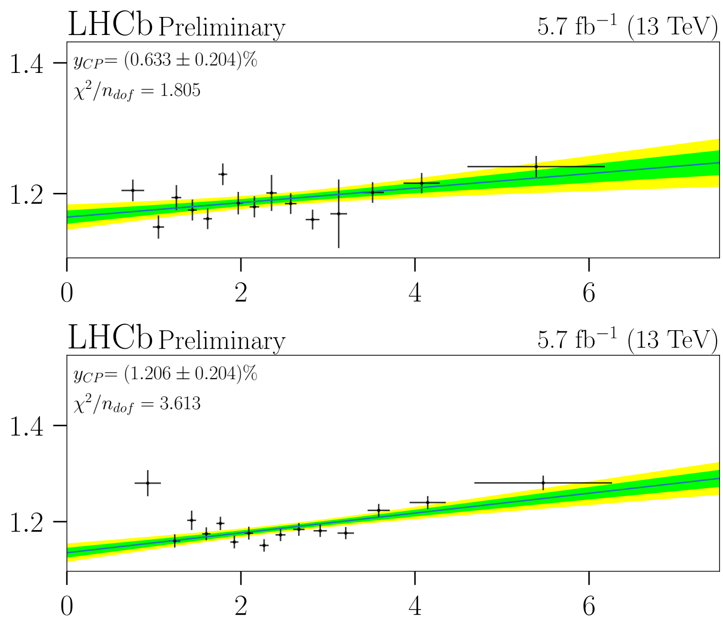

Figure 5.25: *The y_{CP} measurement for the prompt LL (top) and DD (bottom) samples.*

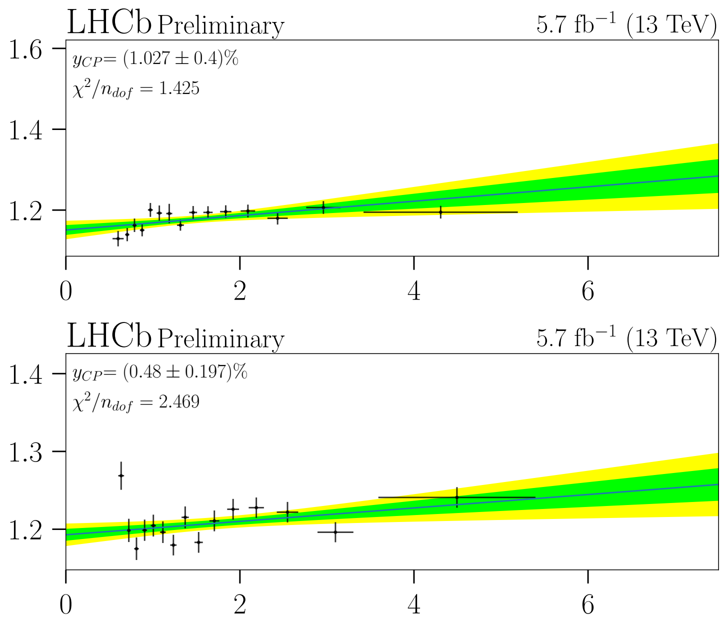

Figure 5.26: *The y_{CP} measurement for the LTUNB LL (top) and DD (bottom) samples.*

The combined result is shown in Fig. 5.27.

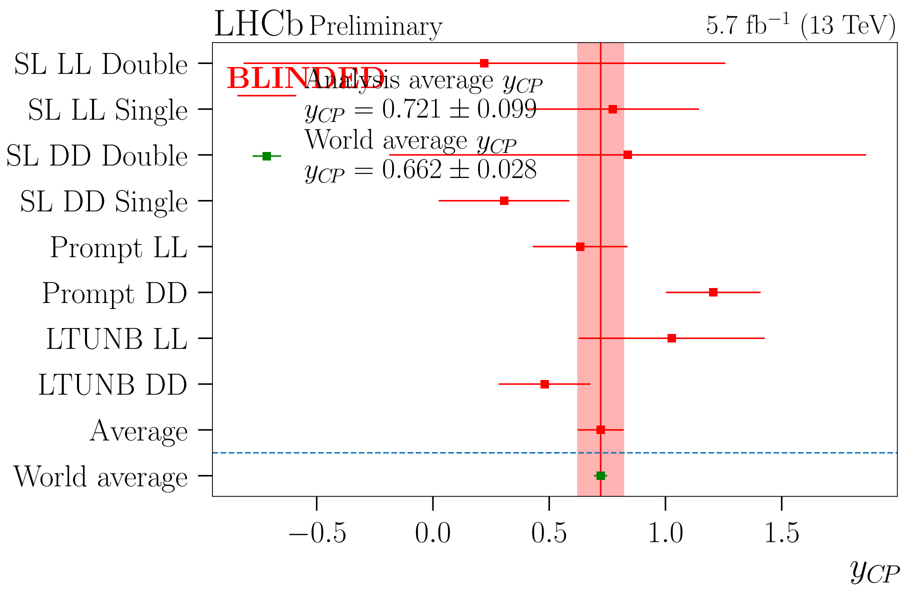

Figure 5.27: *The combined measurement of y_{CP}. The green line shows the world average y_{CP} and its uncertainty. The value of the world average has been shifted to allow comparison of the uncertainties.*

6 Systematic Uncertainties

In this chapter we identify and estimate the systematic uncertainties associated with the measurement of y_{CP}. There are four main systematics identified: secondaries contamination of the prompt sample, decorrelation procedure, uncertainty on the amplitude model, and uncertainty due to choice of binning. All of these are discussed in detail in the following sections.

6.1 Secondaries Contamination

The promptly produced data samples contain a contamination of D^0 mesons which were not produced at the primary vertex, but instead originate from the decay of a B meson, i.e. a secondary decay. The schemes for a true prompt production of a D^0 meson and that originating from a secondary B meson decay are shown in Fig. 6.1. The decay time of the D^0 is calculated as,

$$t = \frac{lm}{p}, \tag{6.1}$$

where l is the flight distance of the D^0, m its mass, and p its momentum. The flight distance, l, candidates reconstructed as prompt is calculated between the primary vertex and the decay vertex of the D^0. Therefore if the D^0 came from the decay of a B meson, the flight distance will be overestimated, and thus the measured decay time too will be overestimated. This can result in a fairly significant overestimation of the decay time as the effective lifetime of the B meson (assuming a mixture of B^0 and B^+) is $\tau_B \approx 1.57\,\text{ps} = 3.83\tau_{D^0}$ [131], compared to a D^0 meson lifetime of $\tau_{D^0} \approx 0.41\,\text{ps}$.

This contamination has a material effect on the measurement of y_{CP} in the prompt sample. The overestimation of the decay time of these mis-reconstructed D^0 decays causes candidates with lower decay times (thus with less time to oscillate) to migrate into higher decay time bins. The decay time of a mis-reconstructed event can be written as,

$$t = t_{D^0} + \delta t, \tag{6.2}$$

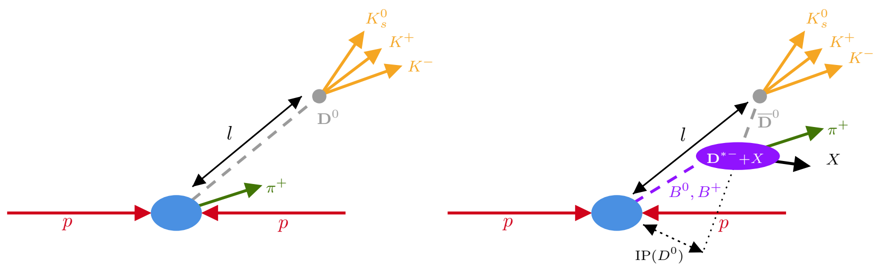

Figure 6.1: *Schematic diagram of the mis-reconstruction of semi-leptonic sample as promptly produced* $D^0 \to K_S^0 K^+ K^-$.

where δt accounts for the difference in decay time between the true D^0 decay time and the reconstructed one. Therefore the average decay time in each decay time bin, j, becomes,

$$\langle t \rangle_j \to (1 - f_{\text{sec}}) \langle t^{\text{prompt}} \rangle_j + f_{\text{sec}} \left(\langle t^{\text{sec.}} \rangle_j + \langle \delta t \rangle_j \right). \tag{6.3}$$

Here we define f_{sec} as,

$$f_{\text{sec}}(t) = \frac{N_{\text{sec.}}(t)}{N_{\text{sec.}}(t) + N_{\text{prompt}}(t)} \tag{6.4}$$

Our strategy to deal with this secondary contamination is two-fold. Firstly we try to remove as much of these secondary decays from the promptly produced samples. Then we estimate the bias the secondaries have on the measurement of y_{CP} and assign an uncertainty to the measurement.

We find that there is a strong discriminating power between the true promptly produced candidates and secondary candidates in the $\log\left(\chi^2_{\text{IP}}\left(D^0\right)\right)$ distribution, as shown in Figs. 6.2 to 6.5. The $\chi^2_{\text{IP}}\left(D^0\right)$ is the χ^2 of the D^0 decay vertex impact parameter (IP) with respect to the prmary vertex. The impact parameter can be seen in Fig. 6.1.

Therefore in order to remove as many secondary decays as possible while also not removing too many true promptly produced candidates, we apply a cut on the $\log\left(\chi^2_{\text{IP}}\left(D^0\right)\right)$ distribution requiring $\chi^2_{\text{IP}}\left(D^0\right) < 9$, as is seen in Table 4.3.

To estimate the bias the secondaries have on the measurement of y_{CP}, we first have to estimate $f_{\text{sec}}(t)$. This is done by fitting the $\log\left(\chi^2_{\text{IP}}\left(D^0\right)\right)$ distribution of the promptly produced data. The data is the same as used in Chapter 5, and is required to satisfy the same selection criteria as described in Chapter 4, except with some slightly looser offline selection requirements. All of the criteria in Table 4.3 are required to be satisfied except for the $\log\left(\chi^2_{\text{IP}}\left(D^0\right)\right)$ cut, the transverse impact parameter, |TIP|, of the D^0 cut, and the vertex-fit χ^2/ndf. This allows us to make a more accurate estimation f_{sec}, and we also estimate $f_{\text{sec}}(t)$ when the $\chi^2_{\text{IP}}\left(D^0\right) < 9$ requirement is applied. This gives us an conservative estimate for f_{sec} found in the promptly produced data used for

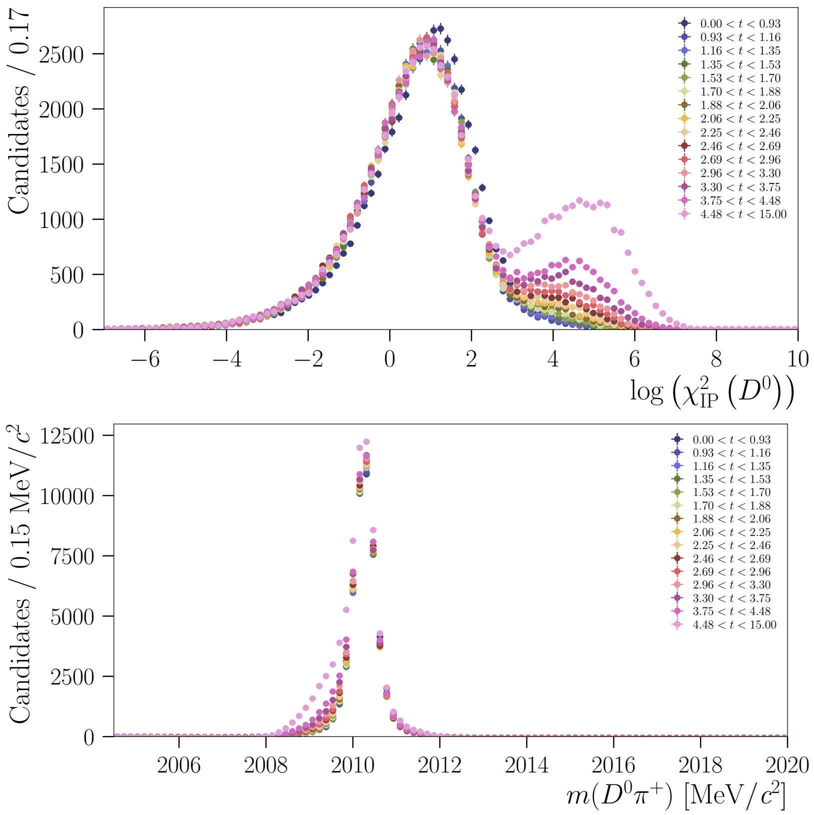

Figure 6.2: *The* $\log\left(\chi^2_{IP}\left(D^0\right)\right)$ *(top) and* $m\left(D^0\pi^+\right)$ *(bottom) distributions for the prompt LL sample. The distributions are split into bins of decay time showing the effect of mis-reconstruction as a function of decay time.*

the measurement. The |TIP| and vertex-fit χ^2/ndf cuts were found to effect the $\log\left(\chi^2_{\rm IP}\left(D^0\right)\right)$ distribution only at high values of $\log\left(\chi^2_{\rm IP}\left(D^0\right)\right)$ (well above 9). Therefore it was judged that these cuts have a negligible effect in the estimate of $f_{\rm sec}$ with $\log\left(\chi^2_{\rm IP}\left(D^0\right)\right) < 9$, and thus the estimate of $f_{\rm sec}$ in the data was valid even without applying these cuts.

In order to determine the appropriate models for the prompt and secondary component of the $\log\left(\chi^2_{\rm IP}\left(D^0\right)\right)$, two MC samples are used. The first is a sample of promptly produced $D^{*+} \to \left(D^0 \to K^0_{\rm S} K^+ K^-\right)\pi^+$ events, again it goes though the same procedure as described in Chapter 4, and again with the same exceptions as described above for the data. The second is a cocktail of secondary B meson decays to D^0, the same MC used for the semi-leptonic sample in Chapter 4. However this time the events are required to undergo an identical reconstruction and selection procedure as the promptly produced data. This allows us to accurately parametrize the mis-reconstructed secondary D^0 decays.

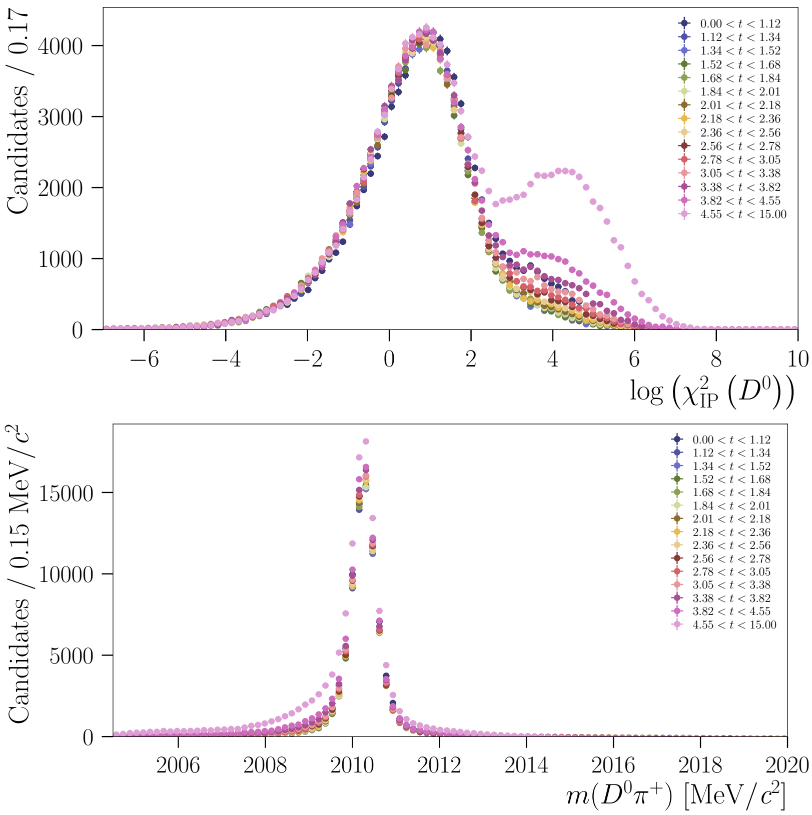

Figure 6.3: *The* $\log\left(\chi^2_{IP}\left(D^0\right)\right)$ *(top) and* $m\left(D^0\pi^+\right)$ *(bottom) distributions for the prompt DD sample. The distributions are split into bins of decay time showing the effect of mis-reconstruction as a function of decay time.*

In order to extract $f_{\mathrm{sec}}\left(t\right)$, we fit the $\log\left(\chi^2_{\mathrm{IP}}\left(D^0\right)\right)$ distribution in bins of decay time and in each bin calculate f_{sec} according to Equation (6.4).

In order to get a statistically pure prompt data sample, we fit the D^{*+} mass distribution, $m\left(D^0\pi^+\right)$. We then use the `sPlot` technique [128] to obtain the `sWeights`, which we can use to construct a statistically pure sample of $D^0 \to K^0_{\mathrm{S}}K^+K^-$ decays, with the combinatorial background subtracted. The fit model is the same as the one described in Section 5.1. This model was found to be satisfactory to fit the data without the $\chi^2_{\mathrm{IP}}\left(D^0\right)$ cut where a larger tail at low D^{*+} mass is seen as shown in Fig. 6.6.

In order to parametrize the $\log\left(\chi^2_{\mathrm{IP}}\left(D^0\right)\right)$ distribution for the prompt and secondaries components we use the respective MC samples.

Both components are modelled as the sum of a Johnson SU Equation (5.2) and a Crystal Ball function [132]. The Crystal Ball line shape is defined as,

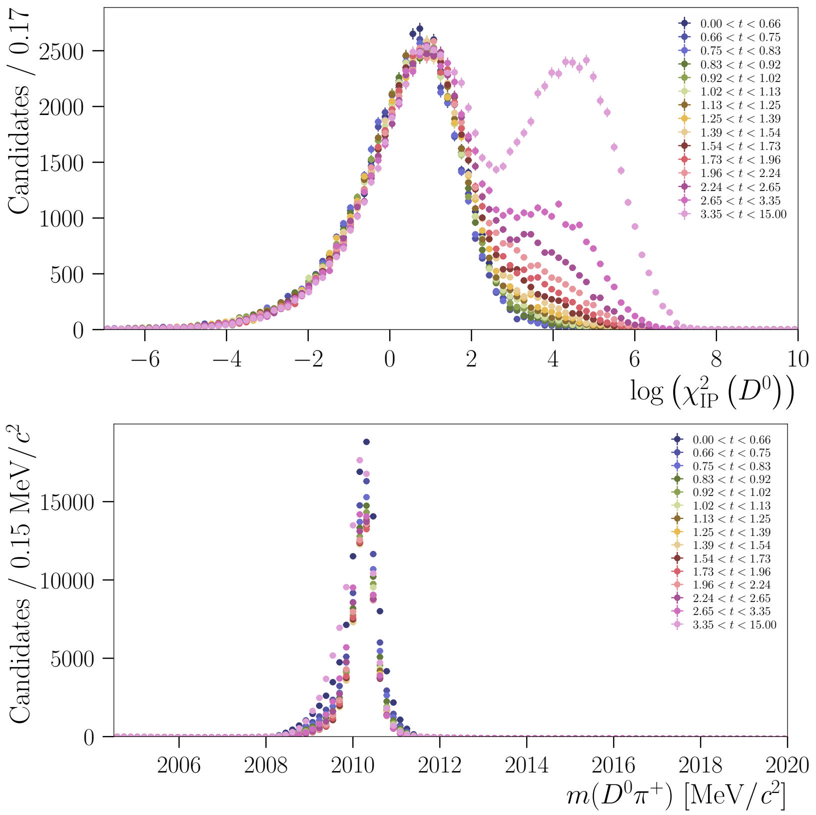

Figure 6.4: *The* $\log\left(\chi^2_{IP}\left(D^0\right)\right)$ *(top) and* $m\left(D^0\pi^+\right)$ *(bottom) distributions for the LTUNB LL sample. The distributions are split into bins of decay time showing the effect of mis-reconstruction as a function of decay time.*

$$\mathscr{CB}\left(x;\mu,\sigma,\alpha,n\right) = \begin{cases}\exp\left(-\frac{1}{2}\cdot\left[\frac{x-\mu}{\sigma_L}\right]^2\right), & \text{for } \frac{x-\mu}{\sigma} > -\alpha \;\; A\cdot(B-\frac{x-\mu}{\sigma})^{-n},\end{cases} \tag{6.5}$$

times some normalization factor, where

$$A = \left(\frac{n}{|\alpha|}\right)^n \cdot \exp\left(-\frac{|\alpha|^2}{2}\right) \; B \qquad = \frac{n}{|\alpha|} - |\alpha| \tag{6.6}$$

and x is $\log\left(\chi^2_{\text{IP}}\left(D^0\right)\right)$.

The total distribution to fit the prompt or secondaries shapes is then,

$$\mathscr{P}_{\text{prompt, sec.}}\left(x;\mu,\sigma,r,s_1,\delta,\gamma,\alpha,n,f\right) = f\,\mathscr{J}\left(x;\mu,r\times\sigma,\delta,\gamma\right) \tag{6.7}$$

$$+\left(1-f\right)\mathscr{CB}\left(x;\mu,r\times s_1\times\sigma,\alpha,n\right). \tag{6.8}$$

In this r is a common resolution scaling factor. In the fits to MC it is fixed to 1 but for the data fits it is allowed to float to account for any common resolution

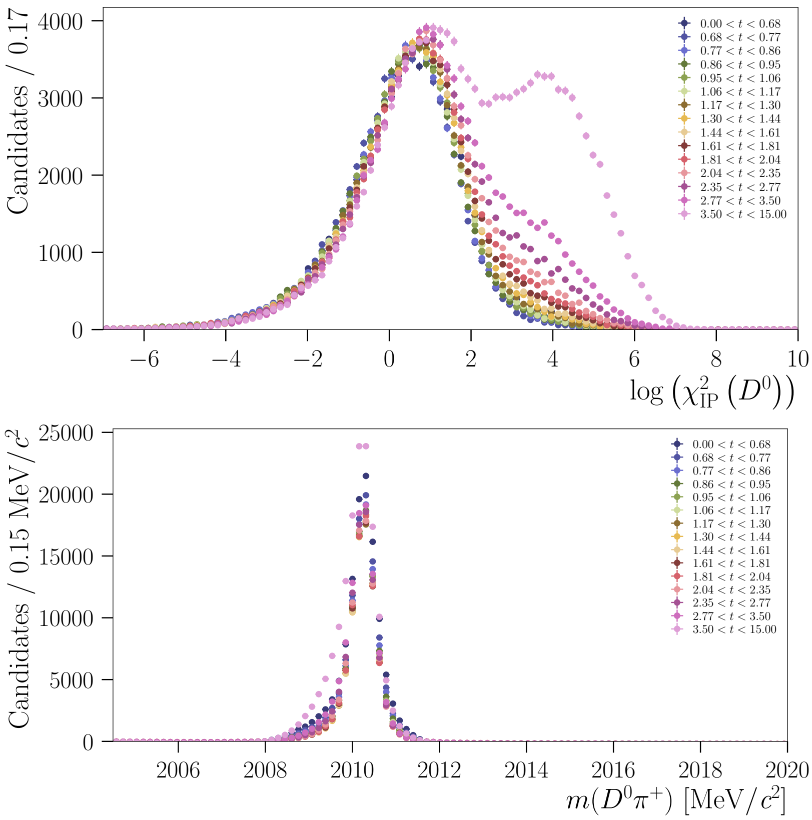

Figure 6.5: *The* $\log\left(\chi^2_{IP}\left(D^0\right)\right)$ *(top) and* $m\left(D^0\pi^+\right)$ *(bottom) distributions for the LTUNB DD sample. The distributions are split into bins of decay time showing the effect of mis-reconstruction as a function of decay time.*

discrepancies between data and MC. The fits to both the promptly produced and secondary reconstructed as promptly produced $\log\left(\chi^2_{\text{IP}}\left(D^0\right)\right)$ distributions are shown in Figs. 6.7 and 6.8.

The total pdf for the $\log\left(\chi^2_{\text{IP}}\left(D^0\right)\right)$ distribution is then,

$$\mathscr{P} = N_{\text{prompt}}\mathscr{P}_{\text{prompt}}\left(x\right) + N_{\text{sec.}}\mathscr{P}_{\text{sec.}}\left(x\right). \tag{6.9}$$

Initially we fit the $\log\left(\chi^2_{\text{IP}}\left(D^0\right)\right)$ distributions in each decay time bin to the prompt and secondary MC samples. From these fits, all parameters are fixed with the exception of N_{prompt}, $N_{\text{sec.}}$, μ_{prompt}, $\mu_{\text{sec.}}$, and r, which are allowed to float. We then fit the background subtracted data (using `sWeights`) with only the remaining parameters allowed to float. and from this we can calculate f_{sec}. Example fits to the decay time integrated data are shown in Fig. 6.9.

f_{sec} is also calculated when a cut is applied to the data of $\chi^2_{\text{IP}}\left(D^0\right) < 9$ to reflect the fraction of secondaries we expect to find in the data used to perform the y_{CP} measurement. The TIP and vertex cut are not included as

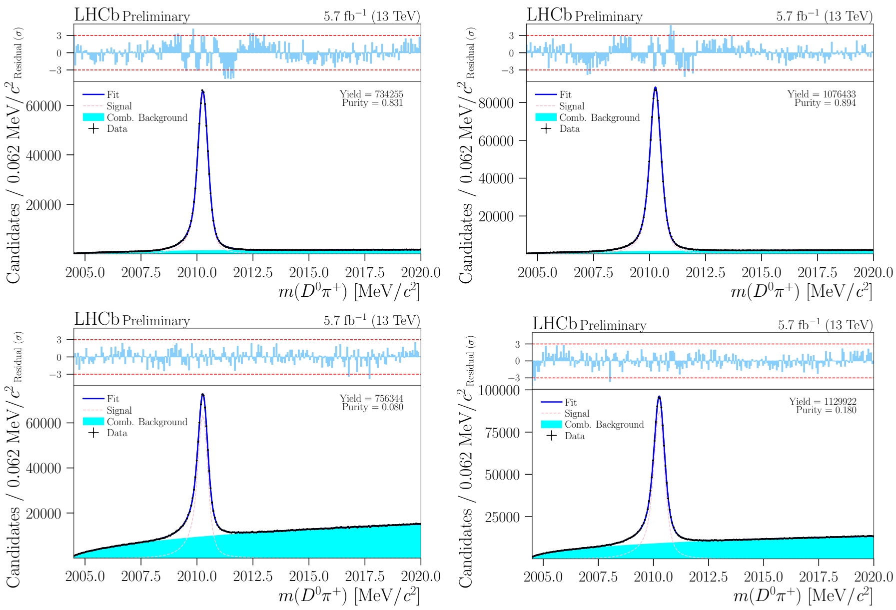

Figure 6.6: *Fits to the D^{*+} mass distribution for the prompt and LTUNB samples with no requirements on the* $\log\left(\chi^2_{IP}(D^0)\right)$. *The top plots show the prompt samples, while the bottom plots show the LTUNB samples. The left plots show the LL samples, while the right plots show the DD samples.*

the effect of these cuts was seen to only be significant at high $\chi^2_{\rm IP}(D^0)$, thus their effect at $\chi^2_{\rm IP}(D^0) < 9$ is expected to be negligible. Further, the fit is also performed in the ON- and OFF-resonance regions of data separately to look for any differences in the $f_{\rm sec}$ values. However the fits to the MC are always performed using the full phase-space integrated sample to ensure sufficient statistics.

The distribution of $f_{\rm sec}(t)$ with and without the $\chi^2_{\rm IP}(D^0)$ is shown in Fig. 6.10.

The secondary reconstructed as promptly produced MC can also be used to estimate the difference between the true D^0 decay time and the reconstructed decay time, δt. Defining,

$$\delta t = t_{\rm reco} - t_{\rm true}, \tag{6.10}$$

we can calculate the average $\langle \delta t \rangle$ within each decay time bin, as shown in Fig. 6.11

With all this information, we can now estimate the systematic uncertainty on y_{CP} due to secondary contamination of the promptly produced sample. To do this we make use of a series of pseudoexperiments, where data is produced using a Monte Carlo technique that includes an amplitude model in the generation of the events. However the simulation is not passed through the detector or

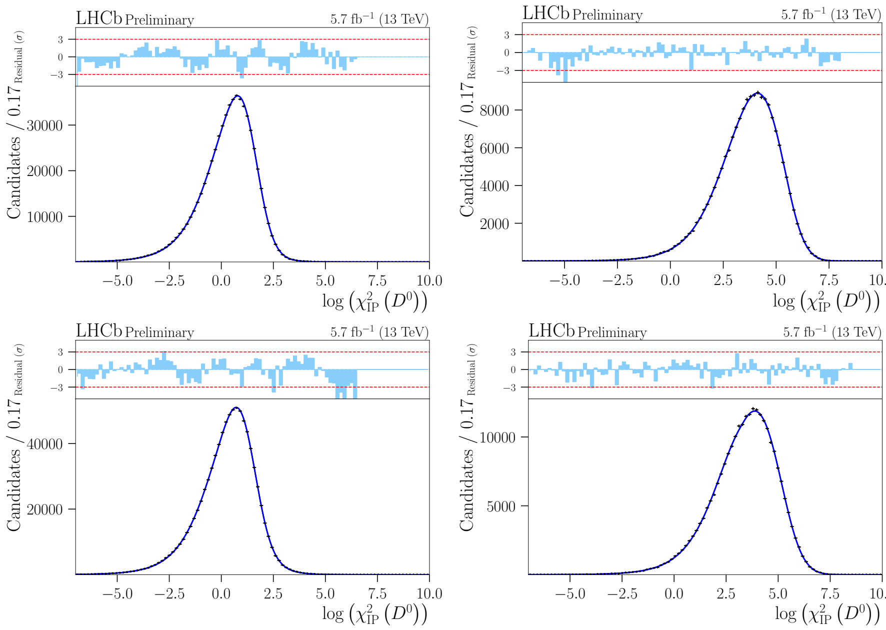

Figure 6.7: *Fits to the decay time integrated* $\log\left(\chi^2_{IP}(D^0)\right)$ *distribution for the prompt promptly produced (left) and secondary reconstructed as promptly produced (right) MC samples. The top plots show the LL samples, while the bottom plots show the DD samples.*

reconstructed using the LHCb framework. Kinematic variables are calculated straight from the generated events. A large number (~ 1000) of pseudoexperiments are generated, and from here they are referred to as 'toys'.

Initially around 1000 toy datasets are produced using the amplitude model published in 2010 by the BaBar collaboration [115]. For each of these toys we measure the value of y_{CP} and build a distribution of y_{CP} values. We can test the validity of our method by calculating a pull distribution of the measured y_{CP} values from the toys. The pull is defined as,

$$\text{Pull} = \frac{y_{CP}^{\text{meas.}} - y_{CP}^{\text{gen.}}}{\sigma_{y_{CP}^{\text{meas.}}}}, \tag{6.11}$$

where $y_{CP}^{\text{meas.}}$ is the measured y_{CP} value from the toy, $y_{CP}^{\text{gen.}}$ is the true y_{CP} value from the amplitude model, and $\sigma_{y_{CP}^{\text{meas.}}}$ is the uncertainty on the measured y_{CP} value from the toy. The toys were all generated with a value of $y_{CP} = 0.6\%$. The distribution of pulls as well as the raw measured values of y_{CP} is shown in Fig. 6.12.

Effects due to secondary contamination of the prompt sample are then added to the toy datasets. This is done by taking each event at random, and generating a random number between 1 and 0. If that random number is less than the value of f_{sec} in the decay time bin the events is in, the event is

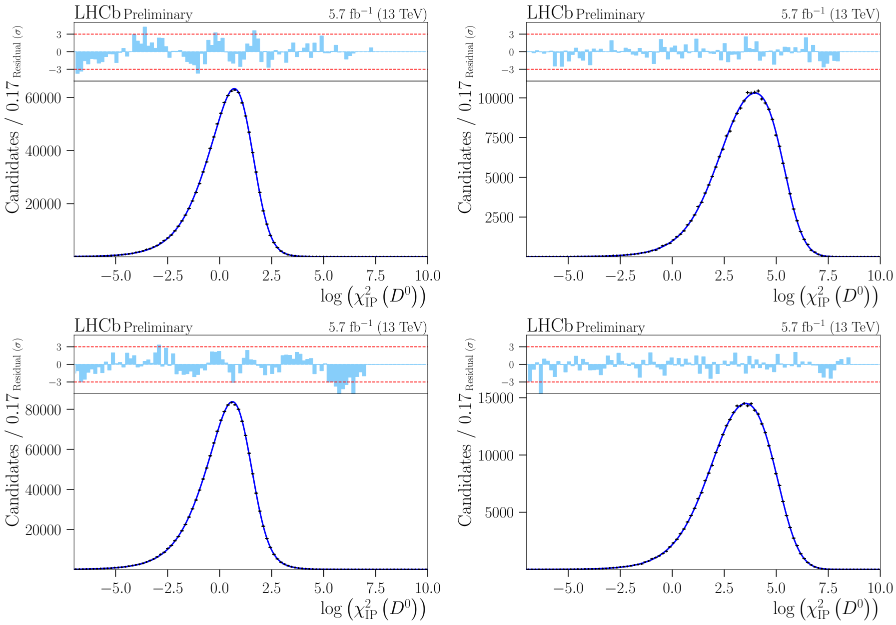

Figure 6.8: *Fits to the decay time integrated* $\log\left(\chi^2_{IP}(D^0)\right)$ *distribution for the LTUNB promptly produced (left) and secondary reconstructed as promptly produced (right) MC samples. The top plots show the LL samples, while the bottom plots show the DD samples.*

considered to be a secondary decay. The value of decay time is then modified by adding the average $\langle\delta t\rangle$ to the true decay time,

$$t_{\mathrm{reco}} = t_{\mathrm{true}} + \langle\delta t\rangle_j. \tag{6.12}$$

Where j is the decay time bin the event is in and the values of $\langle\delta t\rangle_j$ is shown in Fig. 6.11. For each toy the value of y_{CP} is then measured and a distribution of the difference between the measured y_{CP} values in the updated toys and the original generator toys is built. This distribution is shown in Fig. 6.13. This difference shows the bias on the measurement of y_{CP} due to secondary contamination of the prompt sample. As we have a non-negligable, non-zero bias on the measurement of y_{CP} due to the effects of secondary contamination, we assign an uncertainty. We take the width of the distribution, as the systematic uncertainty on y_{CP} due to secondary contamination of the prompt sample, which is summarised in Table 6.1.

6.2 Decorrelation procedure

In order to determine the systematic uncertainty due to the decorrelation procedure outlined in Section 5.3, a control channel, $D_s^+ \to K^+K^-\pi^+$, is studied.

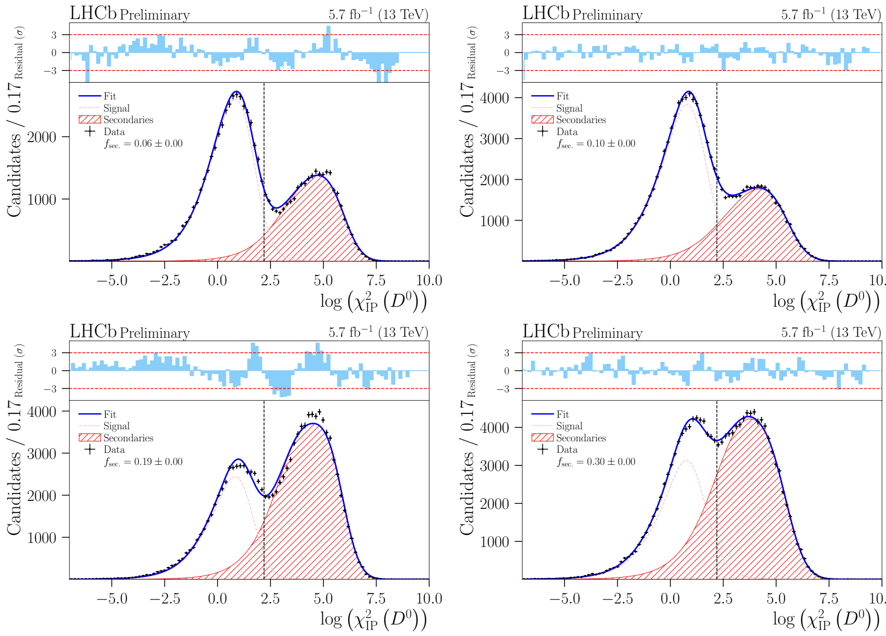

Figure 6.9: *Fits to the decay time integrated* $\log\left(\chi^2_{IP}(D^0)\right)$ *distribution for the data. The top plots show the prompt samples, while the bottom plots show the LTUNB samples. On the left is the LL samples, and right is DD samples.*

Sample	K^0_S Type	$\sigma^{(sec.)}_{y_{CP}}$ [%]
Prompt	LL	0.14
Prompt	DD	0.16
LTUNB	LL	0.07
LTUNB	DD	0.10

Table 6.1: *The systematic uncertainty on* y_{CP} *due to secondary contamination of the prompt sample.*

The control channel is chosen due to its similar topology to the $D^0 \to K^0_S K^+ K^-$ channel, in particular the presence of a strong $\phi(1020)$, *CP*-odd resonance in the $m^2_{K^+K^-}$ Dalitz variable. Critically as the D^+_s meson is charged, it does not undergo any neutral meson mixing, allowing us to test the methodology of the analysis without having to be concerned about the unknown values of mixing parameters. It is expected that by applying the same technique to measure y_{CP} in the $D^+_s \to K^+K^-\pi^+$ channel, the measured value of y_{CP} should be 0. Thus a measurement of $y_{CP} = 0$ in the control channel (within its uncertainty) would provide validation of the technique used to measure y_{CP} in the $D^0 \to K^0_S K^+ K^-$ channel.

The exact same procedure is used to measure y_{CP} in the $D^+_s \to K^+K^-\pi^+$ channel as was used in the $D^0 \to K^0_S K^+ K^-$ channel. The data is first `sWeighted` to extract a statistically pure background subtracted data distri-

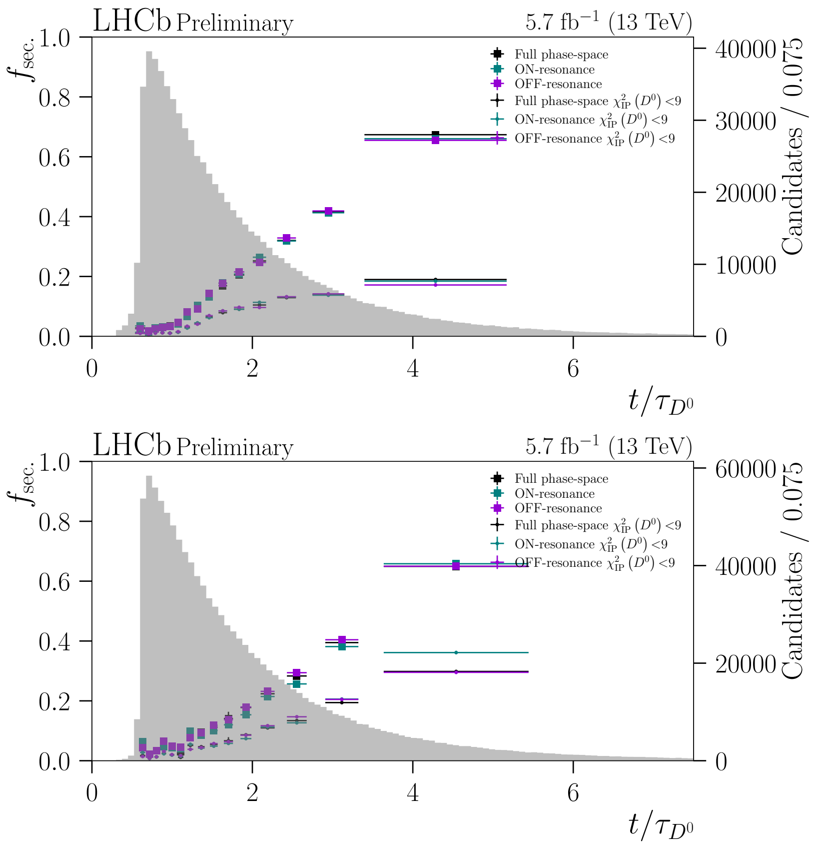

Figure 6.10: *The distribution of f_{sec} as a function of decay time, calculated from fits to the $\log\left(\chi^2_{IP}\left(D^0\right)\right)$ distributions in bins of decay time. Shown is LTUNB LL (top) and DD (bottom) samples.*

bution, shown in Fig. 6.14. This is then used to calculate 15 approximately equally populated bins in decay time. An identical decorrelation procedure is performed, by weighting the reconstructed MC to a sample of generator level MC (described in more detail in Section 5.3), then using the model trained for this reweighting to calculate efficiency correlation weights in the dataset.

The measurement to calculate y_{CP} is then performed by a simultaneous fit between the ON- and OFF-resonance to extract the ratio of yields in each bin and this distribution of ratio of yields is fitted. y_{CP} consistent with zero provides validation of the technique and we take the uncertainty on the measurement of y_{CP} in the control channel to be the systematic uncertainty resulting from the decorrelation procedure. The fit to the $dN_{\mathrm{ON}}/dN_{\mathrm{OFF}}$ distribution is shown in Fig. 6.17, and the associated uncertainty on y_{CP} is $\pm 0.066\%$. The fit shown in Fig. 6.17 is not quite sufficient to validate the method yet and improvements are required in order to . It was found during the analyis that

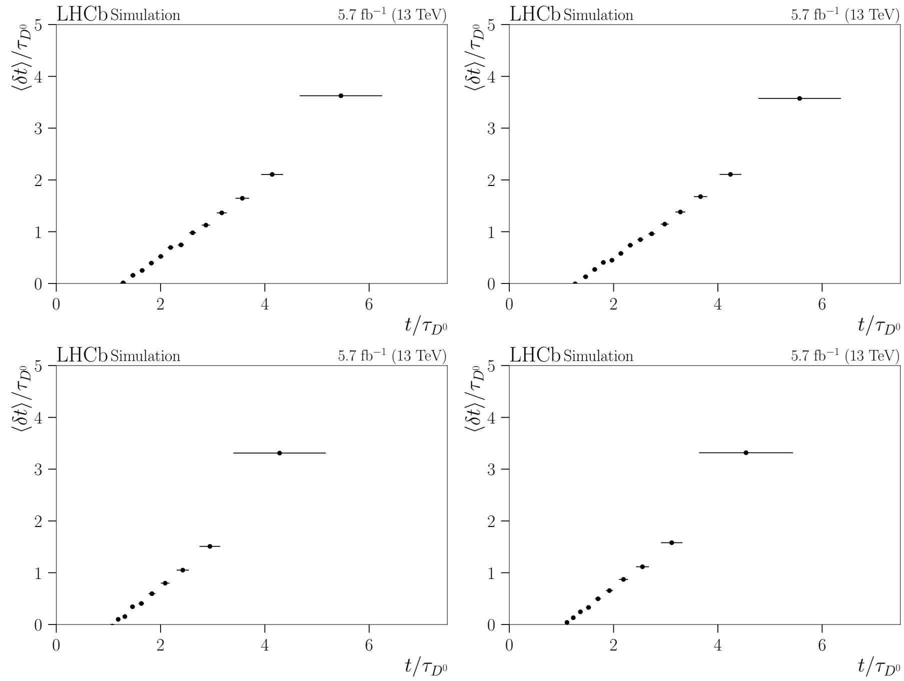

Figure 6.11: *The average difference between the true and reconstructed decay time, $\langle \delta t \rangle$, as a function of decay time. Shown is prompt LL (top left), DD (top right), LTUNB LL (bottom left), and DD (bottom right) samples.*

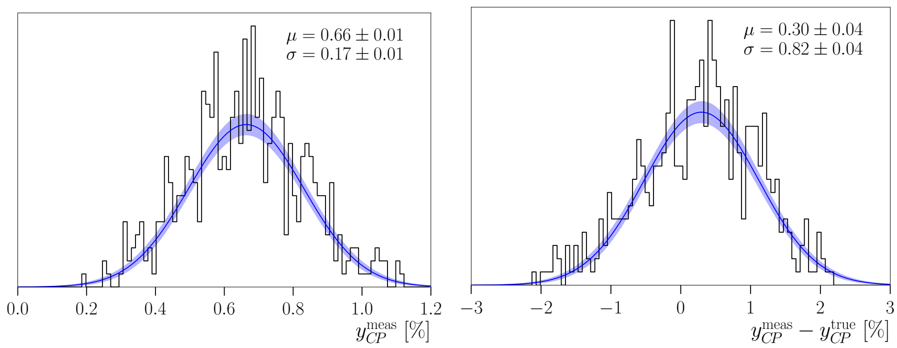

Figure 6.12: *The distribution of the measured y_{CP} values (right) and pulls (left) from the toys.*

due to the large statistics of the channel, improvements could be made to the decorrelation procedure by increasing the size of the architecture used in the reweighter. Successive increases in the number of estimators and depth of the decision tree found improvements to the correction. This in turn increased the training time and computing resources required. It is expected with additional computing resources that the decorrelation procedure could be improved further, but for now the uncertainty on the current measurement is taken as an

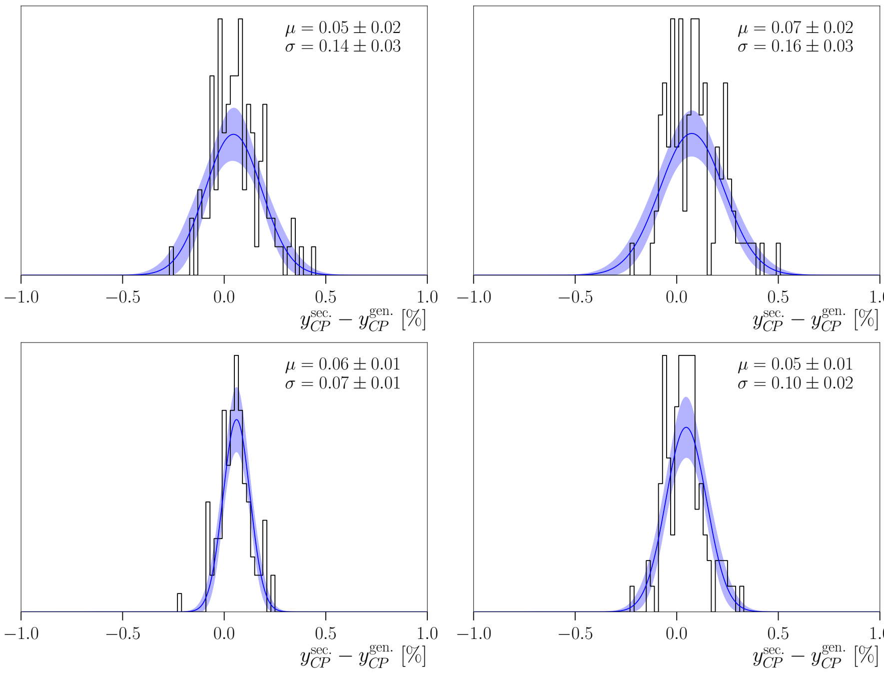

Figure 6.13: *The distribution of the difference of the measured y_{CP} values between the generator toys and the toys that include effects of secondary contamination. Shown is prompt LL (top left), DD (top right), LTUNB LL (bottom left), and DD (bottom right) samples.*

1548 approximation of the systematic uncertainty.

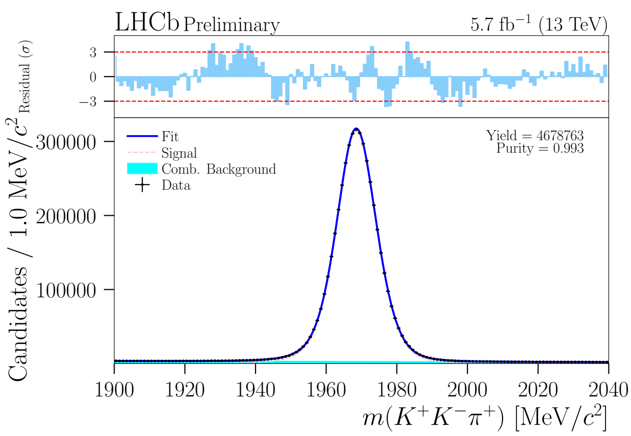

Figure 6.14: *Fit to the D_s^+ mass distribution.*

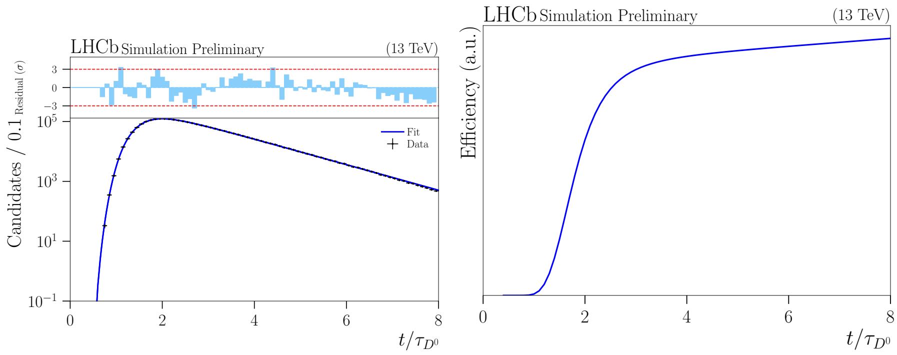

Figure 6.15: *Fit to the simulated decay time distribution (left) and the calculated decay time acceptance (right), for the control sample.*

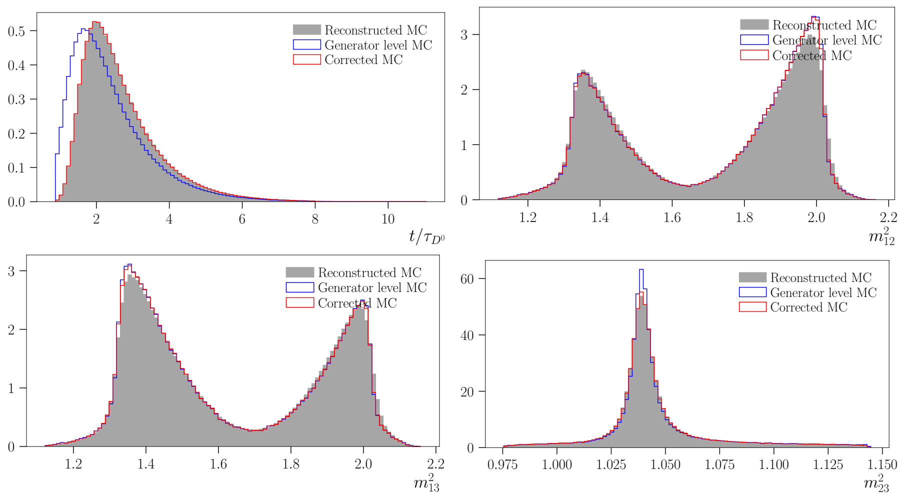

Figure 6.16: *The reweighter trained on the control $D_s^+ \to K^+K^-\pi^+$ sample. The top left shows the decay time, and the right column shows the reweighter trained on the squared invariant masses.*

6.3 Model Uncertainties

As was shown in Chapter 3 the technique for the measurement of y_{CP} is slightly model dependent, in that the parameter $f_{\mathrm{ON}} - f_{\mathrm{OFF}}$ needs to be calculated from an amplitude model. In the analysis, the central value of $f_{\mathrm{ON}} - f_{\mathrm{OFF}}$ was calculated using an amplitude model published by the BaBar collaboration [115]. However, as the amplitude model has an uncertainty on it, in the fitted amplitude and phases, there is also an uncertainty of the value of $f_{\mathrm{ON}} - f_{\mathrm{OFF}}$. This uncertainty needs to be propagated from the fitted values to an uncertainty on $f_{\mathrm{ON}} - f_{\mathrm{OFF}}$. Further there is also other amplitude models for the $D^0 \to K^0_{\mathrm{S}} K^+ K^-$ decay that may give a different central value for $f_{\mathrm{ON}} - f_{\mathrm{OFF}}$.

In the estimation of the systematic uncertainties, two amplitude models are

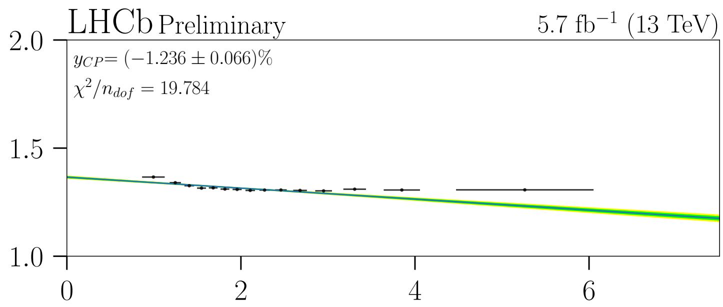

Figure 6.17: *The y_{CP} measurement for the control sample.*

	Dalitz Model I [114]	Dalitz Model II [115]	
Component	Fit Fraction (%)	Fit Fraction (%)	η_{CP}
$K^0_S f_0(980)$	0.4	-	$+1$
$K^0_S a_0(980)^0$	66.4	55.8	$+1$
$K^0_S \phi(1020)$	45.9	44.9	-1
$K^0_S f_2(1270)$	-	0.3	$+1$
$K^0_S f_0(1370)$	3.8	0.1	$+1$
$K^0_S a_0(1450)^0$	-	12.6	$+1$
$K^- a_0(980)^+$	13.4	16.0	
$K^- a_0(1450)^+$	-	21.8	
$K^+ a_0(980)^-$	0.8	0.7	
$\sum$	130.7	152.3	

Table 6.2: *Resonant structure and fitted fractions of each resonant component in the two published amplitude models considered. The value of η_{CP} is the eigenvalue pf the CP operator for the given intermediate state.*

considered. Both from the BaBar collaboration, one published in 2008 [114], the other in 2010 [115]. For simplicity they are labelled Dalitz Model I and Dalitz Model II for the 2008 and 2010 models respectively. The models are summarised in Table 6.2, showing the resonant composition of each model and the respective resonance fit fractions. The fit fraction is defined as the integral over the Dalitz Plot ($\mathcal{DP}$) of a single resonant component divided by the coherent sum of all components[1]:

$$\text{Fit fraction} \equiv \frac{\int \left|a_r e^{i\phi_r} \mathcal{A}_r\right|^2 d\mathcal{DP}}{\int \left|\sum_r a_r e^{i\phi_r} \mathcal{A}_r\right|^2 d\mathcal{DP}} \tag{6.13}$$

A summary of the components within each Dalitz model and their amplitudes and phases are shown in Tables 6.3 and 6.4.

As Dalitz Model II was used in the analysis to calculate the central value of $f_{\mathrm{ON}} - f_{\mathrm{OFF}}$, this shall be focussed on. The model consists of eight resonant

[1] In general the sum of the fit fractions of all components in not equal to unity due to interference.

Dalitz Model I				
Resonance	Mass [MeV]	Width [MeV]	Amplitude	Phase (deg.)
$a_0(980)^0$	999	$g_{\eta\pi} = 324$ $g_{K\overline{K}} = 550 \pm 10$	1.0	0.0
$\phi(1020)$	1019.63 ± 0.07	4.28 ± 0.13	0.437ś0.060	109 ± 6
$f_0(1370)$	1370	200	0.435 ± 0.165	-151 ± 41
$a_0(980)^+$	$m_{a^0(980)^0}$	$g_{\eta\pi}, g_{K\overline{K}}$	0.460 ± 0.059	206 ± 12

Table 6.3: *Amplitudes (a_r), phases ϕ_r, masses, and widths of the resonances in the BaBar 2008 amplitude model [114].*

Dalitz Model I				
Resonance	Mass [MeV]	Width [MeV]	Amplitude	Phase (deg.)
$a_0(980)^0$	999	$g_{\eta\pi} = 324$ $g_{K\overline{K}} = 550 \pm 10$	1.0	0.0
$\phi(1020)$	1019.43 ± 0.02	4.59319 ± 0.00004	0.227ś0.005	-56.2 ± 1.0
$f_2(1270)$	1275.1	184.2	0.261 ± 0.020	-9 ± 6
$f_0(1370)$	1434	173	0.04 ± 0.06	-2 ± 80
$a_0(1450)^0$	1474	265	0.65 ± 0.09	-95 ± 10
$a_0(980)^+$	$m_{a^0(980)^0}$	$g_{\eta\pi}, g_{K\overline{K}}$	0.562 ± 0.015	179 ± 3
$a_0(1450)^+$	$m_{a^0(1450)^0}$	$\Gamma_{a^0(1450)^0}$	0.84 ± 0.04	97 ± 4
$a_0(980)^-$	$m_{a^0(980)^0}$	$g_{\eta\pi}, g_{K\overline{K}}$	0.118 ± 0.015	1138 ± 7

Table 6.4: *Amplitudes (a_r), phases ϕ_r, masses, and widths of the resonances in the BaBar 2010 amplitude model [115].*

contributions: four *CP*-even, one *CP*-odd, and three flavour eigenstates, with no non-resonant contribution. The overall instantaneous amplitude for $D^0 \to K^0_S K^+ K^-$, following the isobar model in Equations (3.10) and (3.11) is then given by,

$$\begin{aligned}
\mathcal{A}(s_0, s_+) = \;& a_{a_0(980)^0} e^{i\phi_{a_0(980)^0}} \mathcal{A}_{a_0(980)^0}(s_0, s_+) \\
&+ a_{\phi(1020)} e^{i\phi_{\phi(1020)}} \mathcal{A}_{\phi(1020)}(s_0, s_+) \\
&+ a_{f_2(1270)} e^{i\phi_{f_2(1270)}} \mathcal{A}_{f_2(1270)}(s_0, s_+) \\
&+ a_{f_0(1370)} e^{i\phi_{f_0(1370)}} \mathcal{A}_{f_0(1370)}(s_0, s_+) \\
&+ a_{a_0(1450)^0} e^{i\phi_{a_0(1450)^0}} \mathcal{A}_{a_0(1450)^0}(s_0, s_+) \\
&+ a_{a_0(980)^+} e^{i\phi_{a_0(980)^+}} \mathcal{A}_{a_0(980)^+}(s_0, s_+) \\
&+ a_{a_0(1450)^+} e^{i\phi_{a_0(1450)^+}} \mathcal{A}_{a_0(1450)^+}(s_0, s_+) \\
&+ a_{a_0(980)^-} e^{i\phi a_0(980)^-} \mathcal{A}_{a_0(980)^-}(s_0, s_+)\,.
\end{aligned} \tag{6.14}$$

In the limit of no direct *CP* violation, $a_r = \overline{a}_r$ and $\phi_r = \overline{\phi}_r$, the overall instantaneous amplitude for the $\overline{D}^0 \to K^0_S K^+ K^-$ is,

$$
\begin{aligned}
\overline{\mathcal{A}}(s_0, s_+) = \overline{\mathcal{A}}(s_0, s_-) = \; & a_{a_0(980)^0} e^{i\phi_{a_0(980)^0}} \mathcal{A}_{a_0(980)^0}(s_0, s_+) \\
& - a_{\phi(1020)} e^{i\phi_{\phi(1020)}} \mathcal{A}_{\phi(1020)}(s_0, s_+) \\
& + a_{f_2(1270)} e^{i\phi_{f_2(1270)}} \mathcal{A}_{f_2(1270)}(s_0, s_+) \\
& + a_{f_0(1370)} e^{i\phi_{f_0(1370)}} \mathcal{A}_{f_0(1370)}(s_0, s_+) \\
& + a_{a_0(1450)^0} e^{i\phi_{a_0(1450)^0}} \mathcal{A}_{a_0(1450)^0}(s_0, s_+) \\
& + a_{a_0(980)^+} e^{i\phi_{a_0(980)^+}} \mathcal{A}_{a_0(980)^+}(s_0, s_-) \\
& + a_{a_0(1450)^+} e^{i\phi_{a_0(1450)^+}} \mathcal{A}_{a_0(1450)^+}(s_0, s_-) \\
& + a_{a_0(980)^-} e^{i\phi a_0(980)^-} \mathcal{A}_{a_0(980)^-}(s_0, s_-) \,.
\end{aligned}
\tag{6.15}
$$

In order to estimate the uncertainty on $f_{\mathrm{ON}} - f_{\mathrm{OFF}}$, *CP* violation is assumed to be zero.

The model is built and the value of $f_{\mathrm{ON}} - f_{\mathrm{OFF}}$ is calculated according to Equation (3.24) by numerical integration. The calculation is repeated around 1000 times, each time the parameters that go into the model are varied within their prescribed uncertainties. This means that for each time the value of $f_{\mathrm{ON}} - f_{\mathrm{OFF}}$ is calculated, every parameter (that is fitted by BaBar and thus has an uncertainty) is determined randomly from a gaussian distribution with a mean of the value published and a width of the uncertainty on that parameter. This builds up a distribution of values of $f_{\mathrm{ON}} - f_{\mathrm{OFF}}$. The uncertainty on $f_{\mathrm{ON}} - f_{\mathrm{OFF}}$ is then taken to be the width of the distribution of $f_{\mathrm{ON}} - f_{\mathrm{OFF}}$ values. The distributions of $f_{\mathrm{ON}} - f_{\mathrm{OFF}}$, f_{ON}, f_{OFF}, are shown in Figs. 6.18 and 6.19.

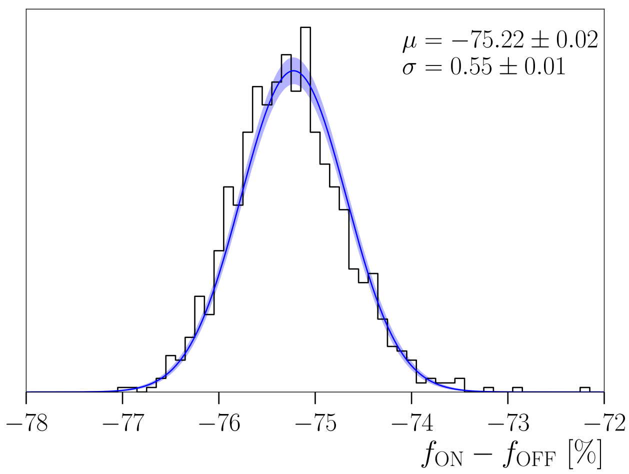

Figure 6.18: *The distribution for $f_{ON} - f_{OFF}$ from the BaBar 2010 model [115], where all the parameters within the model are varied within their prescribed uncertainties.*

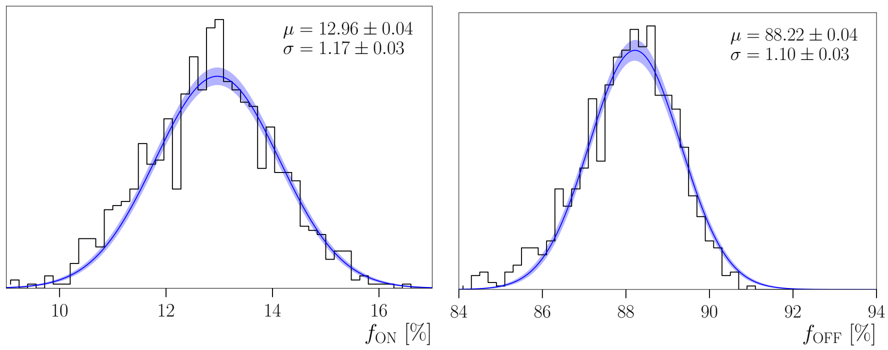

Figure 6.19: *The distributions for f_{ON} (left) and f_{OFF} (right) from the BaBar 2010 model [115], where all the parameters within the model are varied within their prescribed uncertainties.*

Sample	K^0_S Type	Tag	10	15	20	Binning Uncertainty [%]
Prompt	LL		0.561	0.633	1.145	0.0339
Prompt	DD		1.214	1.206	0.961	0.0037
LTUNB	LL		1.594	1.027	0.901	0.2670
LTUNB	DD		1.132	0.480	0.940	0.3072
SL	LL	Single	0.971	0.774	0.748	0.0929
SL	DD	Single	0.249	0.306	0.277	0.0265
SL	LL	Double	-1.398	0.221	0.094	0.7635
SL	DD	Double	0.858	0.838	0.947	0.0094

Table 6.5: *The uncertainty on y_{CP} due to the choice of binning.*

6.4 Binning Uncertainty

In the analysis we make a choice on the number of bins to split the data into. The choice is 15 bins in decay time and this was chosen to optimise the precision of the fit to the $dN_{\mathrm{ON}}/dN_{\mathrm{OFF}}$ distribution while also ensuring sufficient statistics in each bin to allow stable maximum likelihood fits. This choice of binning presents a systematic uncertainty as the choice of binning could in itself bias the measurement of y_{CP}. To account for this uncertainty we perform a very simple study. For each sample we calculate binnings for the case of 10, 15, and 20 bins. We then reperform the measurement of y_{CP} for each sample with each binning. To estimate the uncertainty due to the choice of binning we then take the standard deviation of the resulting y_{CP} values. The results of this study are shown in Table 6.5.

6.5 Systematic uncertainties summary

In this section we evalulated the systematic uncertainties associated with the measurement of y_{CP} due to: secondary contamination of the prompt sample, the decorrelation procedure, uncertainty on the amplitude model, and the choice of binning. The results of this evaluation are summarised in Table 6.6.

<table>
<tr><th colspan="3">Sample</th><th colspan="5">Systematic</th></tr>
<tr><th></th><th></th><th></th><th>Decorrelation</th><th>Secondaries</th><th>Model</th><th>Binning</th><th>Total</th></tr>
<tr><td>Prompt</td><td>LL</td><td></td><td rowspan="8">0.066%</td><td>0.14%</td><td rowspan="8">0.0055%</td><td>0.034%</td><td>±0.158%</td></tr>
<tr><td>Prompt</td><td>DD</td><td></td><td>0.16%</td><td>0.004%</td><td>±0.173%</td></tr>
<tr><td>LTUNB</td><td>LL</td><td></td><td>0.07%</td><td>0.267%</td><td>±0.284%</td></tr>
<tr><td>LTUNB</td><td>DD</td><td></td><td>0.10%</td><td>0.307%</td><td>±0.330%</td></tr>
<tr><td>SL</td><td>LL</td><td>Single</td><td></td><td>0.093%</td><td>±0.114%</td></tr>
<tr><td>SL</td><td>DD</td><td>Single</td><td></td><td>0.026%</td><td>±0.071%</td></tr>
<tr><td>SL</td><td>LL</td><td>Double</td><td></td><td>0.764%</td><td>±0.766%</td></tr>
<tr><td>SL</td><td>DD</td><td>Double</td><td></td><td>0.009%</td><td>±0.066%</td></tr>
</table>

Table 6.6: *Summary of the systematic uncertainties.*

7 Summary

The final result for the y_{CP} measurement is,

$$y_{CP} = X.XX \pm 0.099\,(\text{stat}) \pm 0.083\,(\text{syst})\%, \tag{7.1}$$

where the first uncertainty is statistical and the second is systematic. A summary of the statistical and systematic uncertainties is shown in Table Table 7.1. The final result is still blinded in line with LHCb policy to ensure that the measurement is not biased. Once the analysis is finalised, the procedure will be frozen and the final result unblinded to be published.

Sample			Uncertainty	
			Statistical	Systematic
Prompt	LL		±0.204%	±0.147%
Prompt	DD		±0.204%	±0.169%
LTUNB	LL		±0.400%	±0.282%
LTUNB	DD		±0.197%	±0.328%
SL	LL	Single	±0.370%	±0.109%
SL	DD	Single	±0.281%	±0.062%
SL	LL	Double	±1.036%	±0.766%
SL	DD	Double	±1.026%	±0.057%

Table 7.1: *Summary of the statistical and systematic uncertainties.*

To average the result we take the approach from HFLAV [113]. We have eight statistically independent measurements of y_{CP}, thus the statistical error on each measurement is uncorrelated.

The covariance matrix describing the uncertainties of different measurements and their correlations is constructed, $\mathbf{V} = \mathbf{V}_{\text{stat}} + \mathbf{V}_{\text{syst}}$. As the measurements are from independent data samples, then $\mathbf{V}_{\text{stat}}$ is diagonal, but $\mathbf{V}_{\text{syst}}$

contains correlations. The variance on the average $\hat{x}$ can be written as,

$$\begin{aligned}\sigma_{\hat{x}}^2 = \frac{1}{\sum_{i,j}\mathbf{V}_{ij}^{-1}} &= \frac{\sum_{i,j}\left(\mathbf{V}^{-1}\mathbf{V}\mathbf{V}^{-1}\right)_{ij}}{\left(\sum_{i,j}\mathbf{V}^{-1}\right)^2} \\ &= \frac{\sum_{i,j}\left(\mathbf{V}^{-1}\left[\mathbf{V}_{\text{stat}}+\mathbf{V}_{\text{syst}}\right]\mathbf{V}^{-1}\right)_{ji}}{\left(\sum_{i,j}\mathbf{V}^{-1}\right)^2} \\ &= \sigma_{\text{stat}}^2+\sigma_{\text{syst}}^2.\end{aligned} \tag{7.2}$$

As can be seen in Equation (7.1) the analysis is still statistically limited. The uncertainty on this measurement is roughly four times that of the world average (mainly due to the most recent measurement of y_{CP} which substantially improved the world average precision by ≈ 4 [74]). However as the analysis is statistically limited it will gain significantly from the increased statistics that will be available during Run III of the LHCb detector, and thus could be a very useful analysis to reperform with the increased statistics on Run III. This is the first time that such an analysis has been performed at a hadron collider and in the future a sensible choice of trigger requirements could further enhance its sensitivity.

Part III

Trigger

8 Introduction

Run III of the LHCb experiment began in 2022. With it there was an upgraded detector and a completely new trigger system. The design luminosity in Run III is a factor of five higher than that of Runs I and II. The new trigger system is designed to cope with the increased luminosity as well as the increased pile-up in the detector and to allow more precise physics to be studied using data from Run III.

One significant change in the online trigger system between Runs II and III is the removal of the hardware L0 trigger. The entire trigger is now software based, capable of reading out the detector in real time. Like Run II the trigger consists of two stages, HLT1 and HLT2. Another major change between Runs II and III is the HLT1 trigger has been moved on Graphics Processing Units (GPUs) under the Allen project [133, 134]. This allows the HLT1 trigger to read out the detector at the full 30 MHz rate.

The HLT2 trigger operates in a very similar way to the Run II trigger. While at the HLT1 level only a partial reconstruction of each event is performed with information from a select group of subdetectors, at the HLT2 level a full event reconstruction is performed with full PID information. This allows the HLT2 trigger to operate $\mathcal{O}(1000)$ trigger lines, which are able to perform individual selection for a wide vary of decay channels. The updated trigger system is shown schematically in Fig. 8.1.

In this section we describe how the upgraded LHCb trigger system can be utilised to improve selection on the $D^0 \to K^0_S h^+ h^-$ decay channels.

8.1 Triggering strategies in Run III

As was seen in Section 5.3, the measurements involving the $D^0 \to K^0_S K^+ K^-$ decay channel are limited by severe decay time-momentum correlations. This is also seen in other analysis, such as those using the charm ‘golden channel’ $D^0 \to K^0_S \pi^+ \pi^-$ [68, 129]. It has been found that in Run II of LHCb the decay-time momentum correlations arose at the HLT1 level due to a flight distance cut on the D^0 that was included in the MVA trigger.

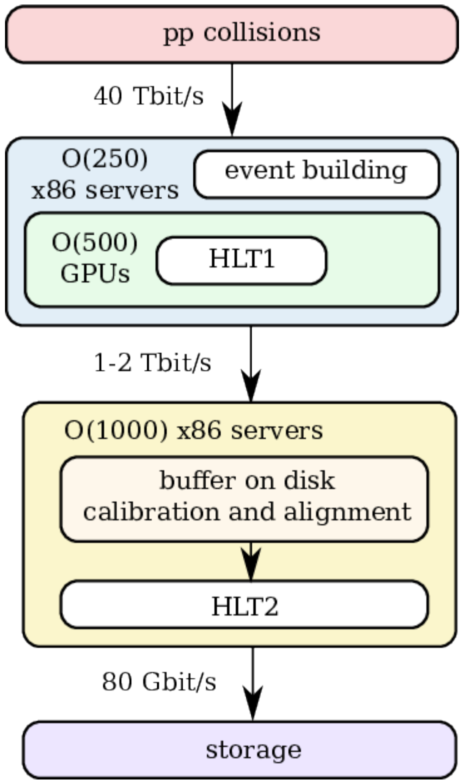

Figure 8.1: *The GPU enhanced LHCb data aquisition and trigger system [133].*

A similar one-track and two-track MVA trigger will be used in Run III, but in order to avoid inducing decay-time momentum correlations again, a new dedicated and exclusive HLT1 trigger line has been designed to select $D^0 \to K^0_S h^+ h^-$ decays. Similar to the LTUNB trigger lines from Run II, in Run III there are ‘Low Bias’ HLT2 trigger lines included that have been designed with looser cuts and minimal cuts on the decay time and other biasing variables.

8.2 The HLT1 trigger

The HLT1 trigger is operated on a GPU trigger farm, where each GPU receives a complete event from the event building unit and handles several thousand events at once. As all the events are independent of each other they can be processed across separate GPUs without the need for communication between them. The raw detector data is copied to the GPU and the full HLT1 sequence is performed on the GPU. Only selection decisions and objects used for the selections, such as tracks and primary vertices, are copied back to the CPU. This avoids the need for costly copies of information between the GPUs and

CPUs during the HLT1 sequence.

The information from the tracking detectors and the muon system is required for HLT1 decisions. Information from the VELO, tracking stations, and muon systems is used, and broadly the HLT1 sequence consists of the following tasks, executed on the GPU:

- Decoding the raw input into coordinates in the LHCb global coordinate system.
- Clustering of measurements caused by the passage of the same particle into single coordinates ("hits"), depending on the detector type.
- Finding combinations of hits originating from the same particle trajectory (pattern recognition).
- Describing the track candidates from the pattern recognition step with a track model (track fitting).
- Reconstructing primary and secondary vertices from the fitted tracks (vertex finding).

Due to the algorithms being performed on a GPU, the algorithms themselves can be highly parallelised and certain tasks can be performed that are otherwise too costly in terms of time on CPUs. This high level of parallelisation is utilised to design a dedicated HLT1 trigger line to select $D^0 \to K^0_S\pi^+\pi^-$ decays.

The algorithm to select $D^0 \to K^0_S\pi^+\pi^-$ broadly works by selecting two vertices, which are reconstructed in an upstream algorithm [1]. The trigger line looks for a K^0_S vertex and a $\pi^+\pi^-$ vertex , and requires that the reconstructed mass of the K^0_S and $\pi^+\pi^-$ vertex falls within a mass window around the mass of the D^0 meson.

It is the parallelisation afforded by the GPUs that allows this task to be performed. The algorithm requires looping over each pair of vertices in every event and looking for a combination of vertices that satisfy the requirements. This would be extremely time expensive on a CPU due to the high combinatorics of the task, and thus is ideally suited to a GPU where each pair of vertices can be evaluated in parallel.

The efficiency of this new line is shown in Fig. 8.2. It can be compared to the one track and two track MVA lines that have been developed for the new HLT1 trigger and are shown in Fig. 8.3. The efficiencies of the one track and two track MVA lines are slightly better than the new $D^0 \to K^0_S\pi^+\pi^-$

[1] Upstream in this context meaning an algorithm that has been performed earlier in the sequence and thus its output is available to later algorithms.

line, however in a similar way to Run II they are likely to induce decay-time momentum correlations. It is expected that improvements can be made to the efficiency of the new $D^0 \to K^0_S\pi^+\pi^-$ line in the future, meaning there is potential great benefit to a range of analysis in Run III, that can utilise this line with less decay time-momentum correlations.

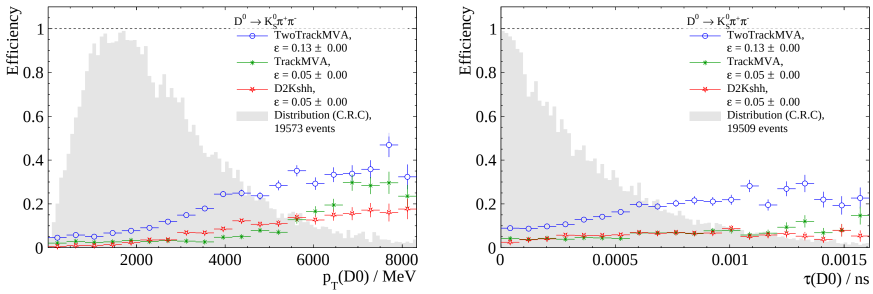

Figure 8.2: *The efficiency of the HLT1 trigger line for $D^0 \to K^0_S\pi^+\pi^-$ decays.*

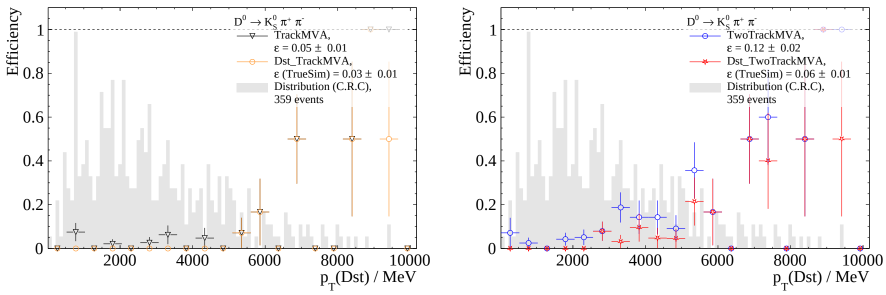

Figure 8.3: *The efficiencies of the one track and two track MVA trigger lines for $D^0 \to K^0_S\pi^+\pi^-$ decays.*

References

[1] Wikipedia, *Democritus*, https://en.wikipedia.org/wiki/Democritus#CITEREFBerryman2016. Accessed: January 2023.

[2] I. Newton, *Opticks, or a Treatise of the reflections, refractions, inflections and colours of light.*, 1718.

[3] CDF, F. Abe *et al.*, *Observation of top quark production in $\bar{p}p$ collisions*, Phys. Rev. Lett. **74** (1995) 2626, arXiv:hep-ex/9503002.

[4] D0, S. Abachi *et al.*, *Observation of the top quark*, Phys. Rev. Lett. **74** (1995) 2632, arXiv:hep-ex/9503003.

[5] DONUT, K. Kodama *et al.*, *Observation of tau neutrino interactions*, Phys. Lett. B **504** (2001) 218, arXiv:hep-ex/0012035.

[6] ATLAS, G. Aad *et al.*, *Observation of a new particle in the search for the Standard Model Higgs boson with the ATLAS detector at the LHC*, Phys. Lett. B **716** (2012) 1, arXiv:1207.7214.

[7] CMS, S. Chatrchyan *et al.*, *Observation of a New Boson at a Mass of 125 GeV with the CMS Experiment at the LHC*, Phys. Lett. B **716** (2012) 30, arXiv:1207.7235.

[8] M. B. Gavela, P. Hernandez, J. Orloff, and O. Pène, *Standard model CP violation and baryon asymmetry*, Mod. Phys. Lett. **A9** (1994) 795, arXiv:hep-ph/9312215.

[9] M. B. Gavela *et al.*, *Standard model CP violation and baryon asymmetry. Part 2: Finite temperature*, Nucl. Phys. **B430** (1994) 382, arXiv:hep-ph/9406289.

[10] P. Huet and E. Sather, *Electroweak baryogenesis and standard model CP violation*, Phys. Rev. **D51** (1995) 379, arXiv:hep-ph/9404302.

[11] SNO, Q. R. Ahmad *et al.*, *Measurement of the rate of $\nu_e + d \rightarrow p + p + e^-$ interactions produced by ^8B solar neutrinos at the Sudbury Neutrino Observatory*, Phys. Rev. Lett. **87** (2001) 071301, arXiv:nucl-ex/0106015.

[12] Super-Kamiokande, Y. Fukuda *et al.*, *Evidence for oscillation of atmospheric neutrinos*, Phys. Rev. Lett. **81** (1998) 1562, arXiv:hep-ex/9807003.

[13] S. Mertens, *Direct Neutrino Mass Experiments*, J. Phys. Conf. Ser. **718** (2016), no. 2 022013, arXiv:1605.0157.

[14] M. Gell-Mann and A. Pais, *Behavior of neutral particles under charge conjugation*, Phys. Rev. **97** (1955) 1387.

[15] F. Muller *et al.*, *Regeneration and mass difference of neutral k mesons*, Phys. Rev. Lett. **4** (1960) 418.

[16] H. Albrecht *et al.*, *Observation of b0-b0 mixing*, Physics Letters B **192** (1987), no. 1 245.

[17] CDF, A. Abulencia *et al.*, *Observation of $B_s^0 - \bar{B}_s^0$ Oscillations*, Phys. Rev. Lett. **97** (2006) 242003, arXiv:hep-ex/0609040.

[18] BaBar, B. Aubert *et al.*, *Evidence for $D^0 - \overline{D}^0$ Mixing*, Phys. Rev. Lett. **98** (2007) 211802, arXiv:hep-ex/0703020.

[19] BELLE, M. Staric *et al.*, *Evidence for D^0 - $\bar{D}^0$ Mixing*, Phys. Rev. Lett. **98** (2007) 211803, arXiv:hep-ex/0703036.

[20] LHCb collaboration, R. Aaij *et al.*, *Observation of D^0–$\overline{D}^0$ oscillations*, Phys. Rev. Lett. **110** (2013) 101802 CERN-PH-EP-2012-333 LHCb-PAPER-2012-038, arXiv:1211.1230.

[21] G. Altarelli and S. Forte, in *Gauge Theories and the Standard Model*, H. Schopper, ed., pp. 7–33, Springer International Publishing, Cham, 2020.

[22] A. A. Penzias and R. W. Wilson, *A Measurement of Excess Antenna Temperature at 4080 Mc/s.*, apj **142** (1965) 419.

[23] A. D. Sakharov, *Violation of CP Invariance, C asymmetry, and baryon asymmetry of the universe*, Pisma Zh. Eksp. Teor. Fiz. **5** (1967) 32.

[24] J. H. Christenson, J. W. Cronin, V. L. Fitch, and R. Turlay, *Evidence for the 2π decay of the k_2^0 meson*, Phys. Rev. Lett. **13** (1964) 138.

[25] BaBar, B. Aubert *et al.*, *Observation of CP violation in the B^0 meson system*, Phys. Rev. Lett. **87** (2001) 091801, arXiv:hep-ex/0107013.

[26] Belle, K. Abe *et al.*, *Observation of large CP violation in the neutral B meson system*, Phys. Rev. Lett. **87** (2001) 091802, `arXiv:hep-ex/0107061`.

[27] LHCb collaboration, R. Aaij *et al.*, *Observation of CP violation in charm decays*, Phys. Rev. Lett. **122** (2019) 211803 LHCb-PAPER-2019-006 CERN-EP-2019-042, `arXiv:1903.0872`.

[28] M. Kobayashi and T. Maskawa, *CP-violation in the renormalizable theory of weak interaction*, Prog. Theor. Phys. **49** (1973) 652.

[29] S. L. Glashow, J. Iliopoulos, and L. Maiani, *Weak Interactions with Lepton-Hadron Symmetry*, Phys. Rev. D **2** (1970) 1285.

[30] S. W. Herb *et al.*, *Observation of a dimuon resonance at 9.5 gev in 400-gev proton-nucleus collisions*, Phys. Rev. Lett. **39** (1977) 252.

[31] Belle, A. Zupanc *et al.*, *Measurement of y(CP) in D0 meson decays to the K0(S) K+ K- final state*, Phys. Rev. D **80** (2009) 052006, `arXiv:0905.4185`.

[32] A. Zupanc, *Measurement of D^0 Mixing in $D^0 \to \phi K_s^0$ Decays*, PhD thesis, Ljubljana U., 2009.

[33] D. Tong, *Line Operators in the Standard Model*, JHEP **07** (2017) 104, `arXiv:1705.0185`.

[34] H. Fritzsch, M. Gell-Mann, and H. Leutwyler, *Advantages of the color octet gluon picture*, Physics Letters B **47** (1973), no. 4 365.

[35] D. J. Gross and F. Wilczek, *Ultraviolet behavior of non-abelian gauge theories*, Phys. Rev. Lett. **30** (1973) 1343.

[36] D. J. Gross and F. Wilczek, *Asymptotically free gauge theories. i*, Phys. Rev. D **8** (1973) 3633.

[37] H. D. Politzer, *Reliable perturbative results for strong interactions?*, Phys. Rev. Lett. **30** (1973) 1346.

[38] S. Weinberg, *Non-abelian gauge theories of the strong interactions*, Phys. Rev. Lett. **31** (1973) 494.

[39] S. L. Glashow, *Partial-symmetries of weak interactions*, Nuclear Physics **22** (1961), no. 4 579.

[40] S. Weinberg, *A model of leptons*, Phys. Rev. Lett. **19** (1967) 1264.

[41] A. Salam, in *Elementary Particle Theory*, N. Svartholm, ed., p. 367, Almquist and Wiksells, Stockholm, 1969.

[42] Particle Data Group, R. L. Workman and Others, *Review of Particle Physics*, PTEP **2022** (2022) 083C01.

[43] J. Ellis, *Higgs Physics*, in *2013 European School of High-Energy Physics*, pp. 117–168, 2015. `arXiv:1312.5672`. doi: 10.5170/CERN-2015-004.117.

[44] F. Englert and R. Brout, *Broken Symmetry and the Mass of Gauge Vector Mesons*, Phys. Rev. Lett. **13** (1964) 321.

[45] P. W. Higgs, *Broken symmetries, massless particles and gauge fields*, Phys. Lett. **12** (1964) 132.

[46] P. W. Higgs, *Broken Symmetries and the Masses of Gauge Bosons*, Phys. Rev. Lett. **13** (1964) 508.

[47] G. S. Guralnik, C. R. Hagen, and T. W. B. Kibble, *Global Conservation Laws and Massless Particles*, Phys. Rev. Lett. **13** (1964) 585.

[48] T. W. B. Kibble, *Symmetry breaking in nonAbelian gauge theories*, Phys. Rev. **155** (1967) 1554.

[49] J. Woithe, G. J. Wiener, and F. F. V. der Veken, *Let's have a coffee with the standard model of particle physics!*, Physics Education **52** (2017) 034001.

[50] C. Burgard, *Standard model of physics programmed in tikz*, `https://texample.net/tikz/examples/model-physics/`. Accessed: January 2023.

[51] E. Sudarshan and R. Marshak, *TheNatureoftheFourFermionInteraction*, in *Padua-Venice Conference on Mesons and Recently Discovered Particles* , 1957.

[52] R. P. Feynman and M. Gell-Mann, *Theory of the fermi interaction*, Phys. Rev. **109** (1958) 193.

[53] Wikipedia, *Standard model of physics programmed in tikz*, `https://en.wikipedia.org/wiki/Chirality_%28physics%29`. Accessed: January 2023.

[54] T. D. Lee and C. N. Yang, *Question of parity conservation in weak interactions*, Phys. Rev. **104** (1956) 254.

[55] C. S. Wu *et al.*, *Experimental test of parity conservation in beta decay*, Phys. Rev. **105** (1957) 1413.

[56] LHCb, F. Betti, *Observation of direct CP violation in D^0 meson decays at LHCb*, `arXiv:1905.0542`.

[57] A. D. Sakharov, *Violation of cp invariance, c asymmetry, and baryon asymmetry of the universe*, Soviet Physics Uspekhi **34** (1991) 392.

[58] G. W. S. Hou, *Source of CP Violation for the Baryon Asymmetry of the Universe*, Int. J. Mod. Phys. D **20** (2011) 1521, `arXiv:1101.2161`.

[59] N. Cabibbo, *Unitary symmetry and leptonic decays*, Phys. Rev. Lett. **10** (1963) 531.

[60] H.-J. He and L. Maiani, *50 years of the gim mechanism*, CERN Courier (2020).

[61] J. J. Aubert *et al.*, *Experimental observation of a heavy particle j*, Phys. Rev. Lett. **33** (1974) 1404.

[62] J. E. Augustin *et al.*, *Discovery of a narrow resonance in e^+e^- annihilation*, Phys. Rev. Lett. **33** (1974) 1406.

[63] L. Wolfenstein, *Parametrization of the kobayashi-maskawa matrix*, Phys. Rev. Lett. **51** (1983) 1945.

[64] CKMfitter group, J. Charles *et al.*, *CP violation and the CKM matrix: Assessing the impact of the asymmetric B factories*, Eur. Phys. J. **C41** (2005) 1, `arXiv:hep-ph/0406184`, updated results and plots available at `http://ckmfitter.in2p3.fr/`.

[65] E. Schrödinger, *An undulatory theory of the mechanics of atoms and molecules*, Phys. Rev. **28** (1926) 1049.

[66] A. L. Kagan and L. Silvestrini, *Dispersive and absorptive CP violation in $D^0 - \overline{D^0}$ mixing*, Phys. Rev. D **103** (2021), no. 5 053008, `arXiv:2001.0720`.

[67] C. A. Chavez, R. F. Cowan, and W. S. Lockman, *Charm meson mixing: An experimental review*, Int. J. Mod. Phys. A **27** (2012) 1230019, `arXiv:1209.5806`, [Erratum: Int.J.Mod.Phys.A 27, 1292006 (2012)].

[68] LHCb collaboration, R. Aaij *et al.*, *Observation of the mass difference between neutral charm-meson eigenstates*, Phys. Rev. Lett. **127** (2021) 111801 LHCb-PAPER-2021-009, CERN-EP-2021-099, `arXiv:2106.0374`.

[69] Particle Data Group, R. L. Workman *et al.*, *Review of particle physics*, Prog. Theor. Exp. Phys. **2022** (2022), no. 8 083C01.

[70] LHCb collaboration, R. Aaij *et al.*, *Measurement of the difference of time-integrated CP asymmetries in $D^0 \to K^-K^+$ and $D^0 \to \pi^-\pi^+$ decays*, Phys. Rev. Lett. **116** (2016) 191601 LHCb-PAPER-2015-055 CERN-EP-2016-022, `arXiv:1602.0316`.

[71] LHCb collaboration, R. Aaij *et al.*, *Measurement of CP asymmetry in $D^0 \to K^-K^+$ and $D^0 \to \pi^-\pi^+$ decays*, JHEP **07** (2014) 041 CERN-PH-EP-2014-082 LHCb-PAPER-2014-013, `arXiv:1405.2797`.

[72] LHCb, *Measurement of the time-integrated CP asymmetry in $D^0 \to K^-K^+$ decays*, `arXiv:2209.0317`.

[73] Heavy Flavor Averaging Group, Y. Amhis *et al.*, *Averages of b-hadron, c-hadron, and τ-lepton properties as of 18 July 2022*, updated results and plots available at `https://hflav.web.cern.ch`.

[74] LHCb collaboration, R. Aaij *et al.*, *Measurement of the charm mixing parameter $y_{CP} - y_{CP}^{K\pi}$ using two-body D^0 meson decays*, Phys. Rev. **D105** (2022) 092013 LHCb-PAPER-2021-041,CERN-EP-2022-022, `arXiv:2202.0910`.

[75] Heavy Flavor Averaging Group, Y. Amhis *et al.*, *Averages of b-hadron, c-hadron, and τ-lepton properties as of 2018*, Eur. Phys. J. **C81** (2021) 226, `arXiv:1909.1252`, updated results and plots available at `https://hflav.web.cern.ch`.

[76] E791, E. M. Aitala *et al.*, *Measurements of lifetimes and a limit on the lifetime difference in the neutral D meson system*, Phys. Rev. Lett. **83** (1999) 32, `arXiv:hep-ex/9903012`.

[77] FOCUS, J. M. Link *et al.*, *A Measurement of lifetime differences in the neutral D meson system*, Phys. Lett. B **485** (2000) 62, `arXiv:hep-ex/0004034`.

[78] CLEO, S. E. Csorna *et al.*, *Lifetime differences, direct CP violation and partial widths in D0 meson decays to K+ K- and pi+ pi-*, Phys. Rev. D **65** (2002) 092001, `arXiv:hep-ex/0111024`.

[79] Belle, M. Starič *et al.*, *Measurement of $D^0\bar{D}^0$ mixing and search for CP violation in $D^0 \to K^+K, \pi^+\pi$ decays with the full Belle data set*, Phys. Lett. B **753** (2016) 412, `arXiv:1509.0826`.

[80] Belle, M. Nayak *et al.*, *Measurement of the charm-mixing parameter y_{CP} in $D^0 \to K^0_S\omega$ decays at Belle*, Phys. Rev. D **102** (2020), no. 7 071102, `arXiv:1912.1091`.

[81] BaBar, J. P. Lees *et al.*, *Measurement of $D^0 - \bar{D}^0$ Mixing and CP Violation in Two-Body D^0 Decays*, Phys. Rev. D **87** (2013), no. 1 012004, `arXiv:1209.3896`.

[82] BESIII, M. Ablikim *et al.*, *Measurement of y_{CP} in $D^0 - \overline{D}^0$ oscillation using quantum correlations in $e^+e^- \to D^0\overline{D}^0$ at $\sqrt{s}$ = 3.773 GeV*, Phys. Lett. B **744** (2015) 339, `arXiv:1501.0137`.

[83] LHCb collaboration, R. Aaij *et al.*, *Measurement of the charm-mixing parameter y_{CP}*, Phys. Rev. Lett. **122** (2019) 011802 LHCb-PAPER-2018-038 CERN-EP-2018-270, `arXiv:1810.0687`.

[84] E. Mobs, *The CERN accelerator complex - August 2018. Complexe des accélérateurs du CERN - Août 2018*, , General Photo.

[85] ATLAS, G. Aad *et al.*, *The ATLAS Experiment at the CERN Large Hadron Collider*, JINST **3** (2008) S08003.

[86] CMS, S. Chatrchyan *et al.*, *The CMS Experiment at the CERN LHC*, JINST **3** (2008) S08004.

[87] ALICE, K. Aamodt *et al.*, *The ALICE experiment at the CERN LHC*, JINST **3** (2008) S08002.

[88] LHCb, A. A. Alves, Jr. *et al.*, *The LHCb Detector at the LHC*, JINST **3** (2008) S08005.

[89] LHCb, R. Aaij *et al.*, *LHCb Detector Performance*, Int. J. Mod. Phys. A **30** (2015), no. 07 1530022, `arXiv:1412.6352`.

[90] LHCb collaboration, C. Elsässer, *$\bar{b}b$ production angle plots*, Accessed: January 2023.

[91] L. collaboration, *Lhcb operation plots webpage*, 2018. Accessed: January 2023.

[92] R. Aaij *et al.*, *Performance of the LHCb Vertex Locator*, JINST **9** (2014) P09007, `arXiv:1405.7808`.

[93] LHCb collaboration, *LHCb VELO (VErtex LOcator): Technical Design Report*, CERN-LHCC-2001-011.

[94] LHCb collaboration, *LHCb reoptimized detector design and performance: Technical Design Report*, CERN-LHCC-2003-030.

[95] U. of Zurich, *Lhcb silicon tracker - material for publications,*, 2012. Accessed: January 2023.

[96] LHCb collaboration, *LHCb inner tracker: Technical Design Report*, CERN-LHCC-2002-029.

[97] LHCb collaboration, *LHCb outer tracker: Technical Design Report*, CERN-LHCC-2001-024.

[98] LHCb Outer Tracker Group, R. Arink *et al.*, *Performance of the LHCb Outer Tracker*, JINST **9** (2014), no. 01 P01002, `arXiv:1311.3893`.

[99] LHCb, M. Stahl, *Machine learning and parallelism in the reconstruction of LHCb and its upgrade*, J. Phys. Conf. Ser. **898** (2017), no. 4 042042, `arXiv:1710.0894`.

[100] LHCb collaboration, *LHCb RICH: Technical Design Report*, CERN-LHCC-2000-037.

[101] LHCb RICH Group, M. Adinolfi *et al.*, *Performance of the LHCb RICH detector at the LHC*, Eur. Phys. J. C **73** (2013) 2431, `arXiv:1211.6759`.

[102] LHCb collaboration, *LHCb calorimeters: Technical Design Report*, CERN-LHCC-2000-036.

[103] C. Abellán Beteta *et al.*, *Calibration and performance of the LHCb calorimeters in Run 1 and 2 at the LHC*, `arXiv:2008.1155`.

[104] LHCb, E. Picatoste Olloqui, *LHCb preshower(PS) and scintillating pad detector (SPD): Commissioning, calibration, and monitoring*, J. Phys. Conf. Ser. **160** (2009) 012046.

[105] LHCb collaboration, *LHCb muon system: Technical Design Report*, CERN-LHCC-2001-010.

[106] F. Archilli *et al.*, *Performance of the Muon Identification at LHCb*, JINST **8** (2013) P10020, `arXiv:1306.0249`.

[107] LHCb collaboration, *LHCb trigger system: Technical Design Report*, CERN-LHCC-2003-031.

[108] R. Matev, *Trigger plots and diagrams for conferences,*, 2018. Accessed: January 2023.

[109] LHCb collaboration, *LHCb computing: Technical Design Report*, CERN-LHCC-2005-019.

[110] G. Barrand *et al.*, *GAUDI - A software architecture and framework for building HEP data processing applications*, Comput. Phys. Commun. **140** (2001) 45.

[111] L. Starterkit, *Lhcb starterkit lessons,*, 2015. Accessed: January 2023.

[112] I. Antcheva *et al.*, *ROOT: A C++ framework for petabyte data storage, statistical analysis and visualization*, Comput. Phys. Commun. **180** (2009) 2499, `arXiv:1508.0774`.

[113] Y. Amhis *et al.*, *Averages of b-hadron, c-hadron, and τ-lepton properties as of 2021*, `arXiv:2206.0750`.

[114] BaBar, B. Aubert *et al.*, *Improved measurement of the CKM angle γ in $B^{\mp} \to D^{(*)}K^{(*\mp)}$ decays with a Dalitz plot analysis of D decays to $K^0_S\pi^+\pi^-$ and $K^0_SK^+K^-$*, Phys. Rev. D **78** (2008) 034023, `arXiv:0804.2089`.

[115] BaBar, P. del Amo Sanchez *et al.*, *Measurement of D0-antiD0 mixing parameters using $D^0 \to K^0_S\pi^+\pi-$ and $D^0 \to K^0_SK^+K^-$ decays*, Phys. Rev. Lett. **105** (2010) 081803, `arXiv:1004.5053`.

[116] BESIII, M. Ablikim *et al.*, *Analysis of the decay $D^0 \to K^0_SK^+K^-$*, `arXiv:2006.0280`.

[117] M. Clemencic *et al.*, *The LHCb simulation application, Gauss: Design, evolution and experience*, J. Phys. Conf. Ser. **331** (2011) 032023.

[118] T. Sjöstrand, S. Mrenna, and P. Skands, *PYTHIA 6.4 physics and manual*, JHEP **05** (2006) 026, `arXiv:hep-ph/0603175`.

[119] D. J. Lange, *The EvtGen particle decay simulation package*, Nucl. Instrum. Meth. **A462** (2001) 152.

[120] Geant4 collaboration, S. Agostinelli *et al.*, *Geant4: A simulation toolkit*, Nucl. Instrum. Meth. **A506** (2003) 250.

[121] Geant4 collaboration, J. Allison *et al.*, *Geant4 developments and applications*, IEEE Trans. Nucl. Sci. **53** (2006) 270.

[122] V. V. Gligorov and M. Williams, *Efficient, reliable and fast high-level triggering using a bonsai boosted decision tree*, JINST **8** (2013) P02013, `arXiv:1210.6861`.

[123] T. Likhomanenko *et al.*, *LHCb topological trigger reoptimization*, J. Phys. Conf. Ser. **664** (2015) 082025.

[124] W. D. Hulsbergen, *Decay chain fitting with a Kalman filter*, Nucl. Instrum. Meth. **A552** (2005) 566, `arXiv:physics/0503191`.

[125] P. Koppenburg, *Statistical biases in measurements with multiple candidates*, `arXiv:1703.0112`.

[126] N. Johnson, *Systems of frequency curves generated by methods of translation*, Biometrika **36** (1949) 149.

[127] A. R. et al., *hep ml - machine learning algorithms for high energy physics*, `https://arogozhnikov.github.io/hep_ml/`.

[128] M. Pivk and F. R. Le Diberder, *sPlot: A statistical tool to unfold data distributions*, Nucl. Instrum. Meth. **A555** (2005) 356, `arXiv:physics/0402083`.

[129] LHCb collaboration, R. Aaij *et al.*, *Model indepedent measurement of charm mixing parameters in $B^- \to D^0(\to K^{*0}\pi^+\pi^-)\mu^-\overline{\nu}_\mu X$ decays*, `arXiv:2208.0651` LHCb-PAPER-2022-020,CERN-EP-2022-160, `arXiv:2208.0651`, to appear in Phys. Rev. D.

[130] W. J. Metzger, *Statistical Methods in Data Analysis*, Radboud Universiteit Nijmegen, 2010.

[131] Particle Data Group, M. Tanabashi *et al.*, *Review of Particle Physics*, Phys. Rev. D **98** (2018), no. 3 030001.

[132] T. Skwarnicki, *A study of the radiative cascade transitions between the Upsilon-prime and Upsilon resonances*, PhD thesis, Institute of Nuclear Physics, Krakow, 1986, DESY-F31-86-02.

[133] R. Aaij *et al.*, *Allen: A high level trigger on GPUs for LHCb*, Comput. Softw. Big Sci. **4** (2020), no. 1 7, `arXiv:1912.0916`.

[134] LHCb collaboration, *LHCb Upgrade GPU High Level Trigger Technical Design Report*, CERN-LHCC-2020-006.